ABSTRACT

Title of dissertation: SENSING SMALL CHANGES
IN A WAVE CHAOTIC SCATTERING SYSTEM
AND ENHANCING WAVE FOCUSING
USING TIME REVERSAL MIRRORS

Biniyam Tesfaye Taddese, Doctor of Philosophy, 2012

Dissertation directed by: Professor Steven M. Anlage
Department of Electrical and Computer Engineering

Wave-based motion sensors, such as radar and sonar, are designed to detect objects within a direct line-of-sight of the sensor. The presence of multiple reflections from surrounding objects usually confounds the sensor. As a result, surveillance of a cavity with multiple internal partitions and complicated boundary conditions generally demands use of a network of sensors, in which each sensor actively monitors a section of the cavity within its direct line-of-sight.

In the first part of the dissertation, we propose and test a new paradigm of sensing that can work in a strongly scattering environment. The sensor utilizes the time reversal invariance and spatial reciprocity properties of the wave equation, and the ray chaotic nature of most real world cavities. Specifically, classical analogs of the quantum fidelity and the Loschmidt Echo are developed with the goal of detecting small perturbations in a closed wave chaotic region. In analogy with quantum fidelity, we employ scattering fidelity techniques which work by comparing response signals of the scattering region, by means of cross correlation and mutual information

of signals. The sensing techniques were compared for various perturbations induced in an acoustic resonant cavity. The acoustic signals are parametrically processed to mitigate the effect of dissipation and to vary the spatial diversity of the sensing schemes. In addition to static boundary condition perturbations at specified locations, perturbations to the medium of wave propagation are shown to be detectable, opening up various real world sensing applications in which a false negative cannot be tolerated.

As an extension of the first part of the dissertation, a sensor is developed to quantitatively measure perturbations that change the volume of a wave chaotic cavity while leaving its shape intact. The sensor was tested experimentally using a one cubic meter pseudo-integrable, microwave resonator. Volume changes that are as small as 4 parts in 10^5 were measured using electromagnetic waves with a wavelength of about $5cm$. Therefore, the sensor is sensitive to extreme sub-wavelength changes of the boundaries of a cavity. Furthermore, the sensor was tested using a frequency domain approach on a numerical model of the star graph, which is a representative wave chaotic system. These results open up interesting applications such as: monitoring the spatial uniformity of the temperature of a homogeneous cavity during heating up / cooling down procedures, verifying the uniform displacement of a fluid inside a wave chaotic cavity by another fluid, etc.

The last part of the dissertation is dedicated to improving the performance of time reversal (TR) mirrors, which suffer from dissipation in wave propagation. TR mirrors can, under ideal circumstances, precisely reconstruct a wave disturbance which happened at an earlier time, at any given later time. TR mirrors have found

applications in imaging, communication, targeted energy focusing, sensing, etc. Two techniques are proposed and tested to overcome the effects of dissipation on TR mirrors. First, a tunable iterative technique is used to improve the temporal focusing of a TR mirror. A single amplification parameter is used to tune the convergence of the iteration. The tunable iterative technique was validated by tests on the experimental electromagnetic time reversal mirror, and on the star graph numerical model. Second, the technique of exponential amplification is proposed to overcome the effect of dissipation in the case of uniform loss distributions, and, to some extent, in the case of non-uniform loss distributions. A numerical model of the star graph was employed to test the applicability of this technique on realizations of the star graph with various spatial distributions of loss. The numerical results were also verified by an experimental result from an electromagnetic TR mirror.

SENSING SMALL CHANGES IN A WAVE CHAOTIC SCATTERING SYSTEM AND ENHANCING WAVE FOCUSING USING TIME REVERSAL MIRRORS

by

Biniyam Tesfaye Taddese

Dissertation submitted to the Faculty of the Graduate School of the
University of Maryland, College Park in partial fulfillment
of the requirements for the degree of
Doctor of Philosophy
2012

Advisory Committee:
Professor Steven M. Anlage, Chair/Advisor
Professor Thomas M. Antonsen, Co-Advisor
Professor Edward Ott, Co-Advisor
Professor Christopher Davis
Professor Rajarshi Roy

Dedication

Dedicated to my parents

Ato Tesfaye Taddese Yeshaw Wolde-Giorgis

and

Woizero Fetlework Abebaw Girmaye (Balambaras-)Chedid Kindu Aqnaw.

Acknowledgments

I would like to acknowledge the indispensable guidance from my advisor Professor Anlage. He provided me with very much needed directions, comments, feedbacks, support, and mentorship during my Ph.D. studies. He introduced me to the exciting field of time reversal, and guided me to develop the experimental skills needed to succeed in my career. He made sure that I had access to state of the art equipment which enabled me to get productive in my research. I would never have achieved my research milestones, without his enthusiastic, timely, and unwavering support. Professor Anlage, thank you very much for your guidance.

I also would like to acknowledge my co-advisors Professor Antonsen and Professor Ott. They gave me very valuable feedback on a regular basis throughout my Ph.D. studies. They also provided me with valuable suggestions on theoretical and simulation tools that I have used to further validate and support my experimental results.

I would like to thank Zach Drikas, Dr. Matthew Frazier, Dr. Gabriele Gradoni, Dr. James Hart, Sun K. Hong, Michael Johnson, Dr. Hai Tran, and Jen-Hao Yeh, for collaborating with me in co-authoring various manuscripts, some of which are included in this dissertation. Specially, I would like to thank Professor Franco Moglie who collaborated with us, and provided us with very helpful simulation results. I would like to thank Professor Thomas H. Seligman, Dr. John Rodgers, and Professor Daniel Lathrop, for their helpful comments about my research. I would like to thank Professor Christopher Davis and Professor Rajarshi Roy for being on my dissertation

defense committee.

I also would like to thank the members of our research groups, Behnood, Cihan, Creeg, David, Enrique, Harita, Laura, Mark, Ming-Jer, Nightvid, Tamin, and Tristen, for their moral support through the years.

Finally, I would like to thank my family, friends, and all the wonderful people in my life, whose list would be too long to write here; I attribute my accomplishments to all of you.

Table of Contents

List of Tables

List of Figures

Chapter 1

Introduction

1.1 Motivation

Traditional wave-based motion sensors, such as radar and sonar, are designed to detect objects within a direct line-of-sight from the sensor. The presence of multiple reflections from surrounding objects usually confounds the sensor. Thus, the spatial coverage of these sensors is usually limited to objects within their direct line-of-sight. As a result, surveillance of a cavity with multiple internal partitions and complicated boundary conditions generally demands use of a network of sensors, in which each sensor actively monitors a section of the cavity.

It is interesting to explore the possibility of using a single sensor to monitor all parts of a complex cavity. Such a wave-based sensor that utilizes more than just ballistic returns would work by broadcasting a brief pulse of radiation to interrogate the cavity. The multiple reflections from different parts of the cavity are recorded to "fingerprint" a given configuration of the cavity at a given time. Using the information from all the reflections, one could imagine a sensing scheme that can detect a perturbation to the cavity under surveillance.

It may also be important to design sensors that are extremely sensitive to almost any kind of perturbation to the cavity under surveillance. This means that the sensors are very suitable to applications in which false negatives cannot be tolerated.

Examples of practical situations where such sensitive detection capabilities are beneficial include, but are not limited to, the following: strict surveillance of the interior of an unoccupied building, scrutiny of a potentially harmful re-arrangement of objects inside an enclosure being transported, supervision of a tightly sealed chamber for gas leaks, inspection of a confined fluid for hazardous turbulence, etc. In each of these circumstances, false negatives may not be tolerated and it is essential to have a sensitive detection mechanism with broad spatial coverage.

1.2 Ray Chaos and Wave Chaos

The possibility of using a single sensor to monitor all parts of a complex cavity becomes a reality in the limit of a wave chaotic cavity. Wave chaotic cavities are classically ray chaotic. Ray chaos is characterized by the fact that ray trajectories in a cavity can be sensitively dependent on their initial conditions; the chaos arises due to complicated and/or non-smooth boundary conditions of a cavity or due to ray-splitting or mode-conversion, which result in more degrees of freedom than constants of motion for the Newtonian point particles that could be imagined to be tracing out the rays in the cavity [1]. Furthermore, ray trajectories in ray chaotic cavities are spatially ergodic (i.e. a ray trajectory visits every corner of the cavity, and eventually gets arbitrarily close to its source).

Wave chaos (quantum chaos) is the study of properties of waves (quantum waves), whose wavelength is much smaller than a typical size of the cavity, propagating in classically ray chaotic cavities [1, 2]. Therefore, the cavity is wave chaotic

if it is classically ray chaotic, and the wavelength of the waves are much smaller than the size of the cavity. In this wave chaotic limit, small perturbations to the cavity can be detected using various techniques.

In the sense that is usually defined, chaos is a property associated with nonlinear dynamical systems [1], and linear wave systems cannot be chaotic [3]. However, wave systems whose classical (very short wavelength) limit is ray chaotic show interesting properties [2]. Because, in the limit where the wavelength is small compared to the characteristic size of the enclosure, wave propagation inside the enclosure can be modeled using ray trajectories. Therefore, the underlying ray chaos manifests itself on the properties of waves propagating in the ray chaotic cavities in the semi-classical limit.

The background material for most of this dissertation is the study of waves propagating inside wave chaotic cavities. Most real world cavities have ray chaotic trajectories, and can be considered wave chaotic for wavelengths that are much smaller than the enclosure dimensions. In related work, our research group has created a Random Coupling Model (RCM) to understand the frequency-domain and time-domain properties of wave chaotic systems using the impedance concept [4, 5, 6, 7, 8], and this model had been tested through experiments on a microwave resonator [9, 10, 11].

Wave chaos is frequently studied in the context of quantum mechanical waves. However, the concepts developed using quantum mechanical waves can generally be extended to classical waves. There are two mathematically equivalent quantities that quantify perturbations to a quantum mechanical system, and are widely celebrated

in the wave chaos research community: these are the quantum fidelity and the Loschmidt echo [12, 13, 14]. The classical extensions of these two concepts are the cornerstones for the sensors that are proposed and tested in this dissertation.

1.3 Extending the Concepts of Loschmidt echo and Quantum Fidelity to Classical Waves

1.3.1 Extending the Quantum Fidelity

The sensing technique based on the classical (acoustic, electromagnetic, etc) extension of quantum fidelity can be described as follows. A brief pulse is broadcast into a wave chaotic cavity, and the response signal, which we call *sona* [1], is collected. The sona essentially consists of multiple reflections of the original pulse inside the cavity. The sona can be collected before and after an alleged perturbation event; then, signal processing techniques such as cross correlation and mutual information can be used to compare the two sonas collected. It is appealing to explore if such signal comparisons allow the detection of perturbations to the cavity under surveillance. Exploration of this detection task leads to the following questions, which are answered in this dissertation. What kinds of perturbations can be detected in the cavity? Is there a possibility of distinguishing perturbations that happen at different locations within the cavity? What is the smallest perturbation that can be reliably detected?

[1] The word sona comes from the Latin word sonabilis, which means resonant. The sona refers to the entire response signal from the resonant cavity.

However, the concept of quantum fidelity, which quantifies the sensitivity of the dynamics of a quantum mechanical system to small perturbations of its Hamiltonian, is already well developed [13, 14]. Besides, the idea of quantifying perturbations to a system using a "propagation comparison" of two different final states of the system obtained from a given initial state is not new, per se. For instance, the concept of quantum fidelity has been applied to classical waves as in the study of the scattering fidelity of acoustic waves, which is, practically speaking, the correlation between sona signals as a function of time [14, 15]. The relative merits of the cross correlation and mutual information of acoustic signals in the context of underwater source detection has been studied, for example, in Ref. [16]. The work in this dissertation is new in that the scattering fidelity concept is used to detect, and in some cases quantify, practical perturbations to real world cavities.

1.3.2 Extending the Loschmidt Echo

The Loschmidt echo is mathematically equivalent to the quantum fidelity as it is shown in Sec. 2.2. However, its realization is quite different. The Loschmidt echo is an overlap between the initial and final states of a quantum mechanical system. A perturbation is applied sometime before the generation of the final state of the system. The initial state is propagated forward in time using the unperturbed Hamiltonian of the system for time t. This gives an intermediate state of the system. Then the system is perturbed and described by a new Hamiltonian. The intermediate state is propagated backward in time using the new perturbed

Hamiltonian of the system for the same time duration t. This gives the final state of the system. The overlap (correlation) between the initial and final states is called the Loschmidt echo, and it is indicative of the strength of the perturbation. The Loschmidt echo was used to quantify contrived perturbations to local boundaries of quantum mechanical systems [12]. The Loschmidt echo also makes connection to spin-echo experiments widely used in nuclear magnetic resonance [17].

The sensing technique based on the classical (acoustic, electromagnetic, etc) extension of the Loschmidt echo can be implemented as follows. A brief pulse is broadcast into the cavity, and the resulting sona signal is recorded. The digitized sona is time reversed and broadcast back into the cavity. Due to the time reversal invariance of the wave equation, the original pulse is reconstructed in a time reversed fashion at the original location of the source. This reconstruction can be achieved periodically using a single sona signal. Thus, two brief time-reversed pulses, which are reconstructed before and after a supposed perturbation, can be compared efficiently to detect the perturbation. The questions that arose in the discussion of the sensing technique based on the classical extension of the quantum fidelity are also of interest in the study of this detection technique as well. Finally, it is fascinating to compare the relative merits of the sensing techniques that are based on the extension of the quantum fidelity, and the techniques that are based on the extension of the Loschmidt echo.

Through my work, the concepts of quantum fidelity and Loschmidt echo have been successfully extended to acoustic and electromagnetic waves to realize practical sensors [18, 19, 20]. Chapter 2 and 3 of this dissertation present those results.

1.4 Time Reversal Mirrors

The concept of the Loschmidt echo has been extended to classical waves using "time-reversal mirrors" for acoustics [21, 22] and electromagnetics [23, 24, 25]. Ideally, time reversal (TR) mirrors operate by collecting and recording a propagating wave as a function of time, and at some later time they propagate it in the opposite direction in a time-reversed manner. Experimentally, it is not generally possible to mirror all waves in this manner. Experimental TR mirrors can however be realized in the special case of confined systems with highly reflective walls (so called 'billiard' systems) and classically chaotic ray dynamics such as those considered in this dissertation. Under these conditions a single-channel TR mirror can very effectively approximate the conditions required to measure the Loschmidt echo using classical waves [25, 26]. The experimental set up for the measurement of the Loschmidt echo can be further simplified by exploiting the spatial reciprocity of the wave equation [22, 18, 19].

TR mirrors face two limitations, which cause them to have less than ideal performance. These are limited spatiotemporal coverage of recording and transmitting channels, and dissipation. There have been techniques developed as extensions of the typical TR procedure in order to partially overcome the effects of dissipation. One such technique is the so called iterative TR [27]; the technique enables improved TR focusing even in the presence of loss. The technique of perfect inverse filter is claimed to achieve a better time reversed focusing than standard time reversal techniques [28, 29]; the perfect inverse filter works by multiplying the sona

signal in the frequency domain by the inverse of the transfer function of the cavity. In Chapter 4 of this dissertation, the iterative TR technique is enhanced by introducing a parameter that tunes its convergence [30]. In Chapter 5 of the dissertation, a technique of exponential amplification of the sona signal is shown to counter the effects of dissipation on TR mirrors; this is the case even in cavities with moderately inhomogenous spatial distribution of loss.

1.4.1 Applications of Time Reversal Mirrors

TR mirrors have found a wide range of practical applications in various fields. These include: non destructive imaging, development of virtual sources in geophysics, electromagnetic weapons, super-resolution wave focusing, imaging, localization, and communication.

Acoustic TR mirrors have been used to carry out non-destructive imaging of solids to detect micro-fractures [31, 32, 33]. This work relies on the fact that micro-fractures generate acoustic nonlinearities. The micro-fractures can be considered as sources of the higher harmonic waves recorded in the system. TR mirrors are then used to time reverse and broadcast these higher harmonics back into the solid. Using a scanning laser vibrometer, the harmonics can be seen focusing on the location of the micro fractures. Another application of non-destructive imaging of elastic objects uses the interaction of acoustic and electromagnetic waves [34]. Reference [34] images mechanical flaws using the modulation of electromagnetic waves scattered from an object that is acoustically illuminated, and hence mechanically

affected. TR mirrors are used to improve the sensitivity of the imaging and obtain information about the location of flaws within the target.

TR has also drawn interest in the field of geophysics. TR mirrors have been used to realize virtual sources underground; the virtual sources enable imaging geological formations beyond a seismically opaque geological stratum [35]. In [36], the localization of tremor sources is demonstrated by playing a movie of the devastating event unfold backward in time by using a computer model of the earth. Outside geophysics, Ref.[37] looks at source localization applications of electromagnetic TR.

The potential application of TR in developing electromagnetic weapons is investigated in [38]. In this work, a leaky reverberation chamber (with an aperture) is used to focus a high power electromagnetic signal with an 18dB gain over a regular directive antenna with an aperture. I have been co-authoring a manuscript with Sun K. Hong et. al. of the Naval Research Laboratory to extend this work in a new direction. Our objective is to focus an arbitrary waveform at some distance away from a leaky reverberation chamber. The manuscript is under preparation.

Regarding super-resolution time reversed focusing, there has already been some experimental success in achieving focusing beyond the diffraction limit [39]; this work relied on designing an antenna structure that accomplishes conversion between evanescent and propagating modes, which has theoretical backing [40]. The diffraction limit in time reversed focusing has also been overcome by introducing an "acoustic sink" at the port [41]. This work could have future applications in the field of microwave microscopy as detailed in Chapter 6 of the dissertation. A detailed theoretical treatment of super-resolution time-reversed acoustic focusing is provided

in [42]. A theoretical foundation for an experimental design of electromagnetic TR mirrors with a sub-wavelength focusing is provided in [43].

TR mirrors have been applied to improve the contrast and resolution of an imaging technique called Microwave-Induced Thermo-Acoustic Tomography Imaging [44]. Microwave-Induced Thermo-Acoustic Tomography Imaging is a biological tissue imaging technique that rivals conventional ultrasound and microwave imaging systems for malignant tumors. On the other hand, imaging of a target in a cluttered environment using an electromagnetic TR mirror is demonstrated in [45] assuming perfect knowledge of the Green's function of the background environment. The feasibility of building 3D images using a TR chaotic cavity is demonstrated in [46].

Improved acoustic communication in air is enabled using TR mirrors [47]. A numerical study of the possibility of improved indoor communication using electromagnetic TR is done in [48]. The promising application of electromagnetic TR in the field of communication (for instance in Multiple Input Multiple Output systems, etc) is explored in [49].

A different paradigm in the implementation of TR mirrors is introduced in [50]. In this work, TR of ultra wide band (i.e. $3 - 10GHz$ bandwidth) impulses is demonstrated in the frequency domain using affordable electronic circuit systems. This could enhance the competitiveness of TR mirrors in various applications such as communications.

TR has also found its applications in industry. Notably some of Mathias Fink's collaborators in France have started a company, (www.sensitiveobject.fr), whose

products heavily rely on TR technology. One of their products is a 2D, flat, touch-sensitive keyboard that can be customized to activate different devices in a living room. This product associates the "sona" generated when a spot on the keyboard is touched with a particular duty to be executed. Therefore, their products are relying on the reproducibility of a sona signal despite some uncontrollable changes that may happen to the touch-sensitive keyboard cavity; in this sense, they are using a different general perspective from that presented in this dissertation.

Historically, practitioners of time-reversed techniques have ignored the small changes in sona and reconstructed pulses due to perturbations. The practitioners have been mainly relying on the robustness of the time-reversed pulse to study other phenomena discussed above such as communication and localization. In this dissertation, we adopt the opposite perspective and focus on the cause of small changes to the signals due to the tiniest perturbations.

1.5 Outline of the Dissertation

As shown in Fig. 1.1, the dissertation revolves around the core concepts of Loschmidt echo and quantum fidelity applied to classical waves propagating in complex enclosures. Chapter 1 introduces the background material on ray chaos, wave chaos, and time reversal. This is the background to understand the Loschmidt echo and quantum fidelity concepts, and their classical extensions. The concepts are extended to classical waves such as acoustic and electromagnetic waves to realize a new paradigm of practical sensors. The sensors are designed to rely on informa-

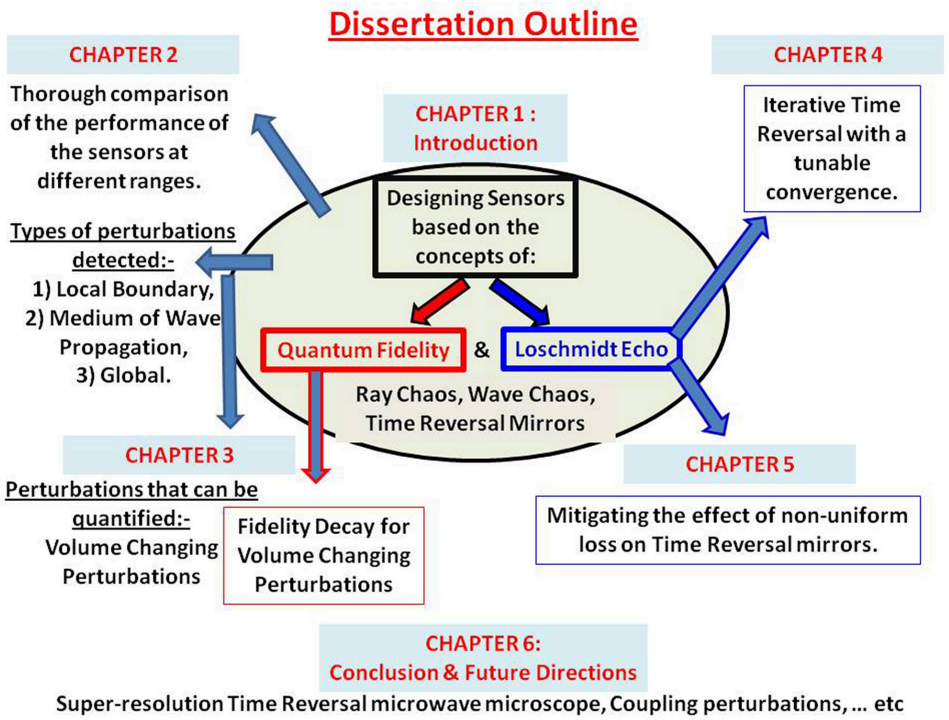

Figure 1.1: Outline of the dissertation. Chapter 1 introduces the background material on ray chaos, wave chaos, and time reversal. Chapter 1 introduces the extension of the Loschmidt echo and quantum fidelity to classical waves to realize practical sensors; this is the core of the dissertation. Chapter 2 formally defines the Loschmidt echo and quantum fidelity. Chapters 2 and 3 focus on the sensing problem. Chapters 4 and 5 propose techniques to improve the performance of time reversal mirrors which extend the Loschmidt echo to classical waves. Chapter 6 provides a conclusion, and directions for future work.

tion from multiple reflections, and can detect perturbations that are outside their line-of-sight. This capability makes the sensors reasonable alternatives to existing sensors such as radar and sonar. The downside is that the sensors may suffer from false positives even though they have minimal false negatives.

The dissertation can be divided into two main parts. The first part consists of Chapters 2 and 3. These chapters focus on the design and test of the sensors inside

real world cavities. Chapter 2 proposes four sensing techniques that are based on the extensions of the Loschmidt echo and quantum fidelity. The performance of these sensing techniques are thoroughly compared after defining a Figure of Merit of the sensing techniques. The sensing techniques are compared for various kinds of perturbations that are made inside an acoustic resonator cavity. The perturbations include the following: i) perturbations to local boundary conditions of the cavity at different ranges from the sensor, ii) perturbations to the medium of wave propagation inside the cavity, and iii) global perturbations.

Chapter 3 is conceptually an extension of the work in Chapter 2. Chapter 3 focuses on perturbations that can not only be detected but also quantified. In particular, perturbations which change the volume of a cavity while leaving its geometric shape intact are considered. These volume changing perturbations are quantified inside an electromagnetic pseudo-integrable cavity using different sensing techniques. The results are also supported by a numerical simulation inside a representative wave chaotic cavity. The nature of fidelity decay for volume changing perturbations is also discussed Chapter 3; this is relevant to the existing literature on fidelity decay regimes for different classes of perturbations [14].

The second part of the dissertation includes Chapters 4 and 5. These chapters propose and test techniques which improve the performance of TR mirrors. The performance of TR mirrors suffers from dissipation, and the techniques introduced partially counteract dissipation's adverse effects. Chapter 4 introduces tunability to the convergence of the iterative TR technique. The iterative time reversal technique improves the spatiotemporal focusing of waves using TR mirrors. The tunability of

the iterative technique is demonstrated both experimentally, and using a numerical simulation of a representative wave chaotic system. Chapter 5 introduces the exponential amplification technique to improve the performance of TR mirrors. The technique works best when the loss is distributed uniformly in the cavity. However, it is also shown that the exponential amplification technique can partially mitigate the effect of dissipation in cases with inhomogenous spatial loss distributions.

Finally, Chapter 6 provides a conclusion that ties all the results together. In addition, future directions for research in TR mirrors, and fidelity are outlined. For instance, the possibility of beating the diffraction limit using time reversal mirrors [39], opens up new opportunities in the development of super resolution microwave microscopes using time reversal mirrors.

Chapter 2

Sensing Small Changes in a Wave Chaotic Scattering System

In this chapter, classical analogs of the quantum mechanical concepts of the Loschmidt echo and quantum fidelity are developed with the goal of detecting small perturbations in a closed wave chaotic region. Sensing techniques that employ a one-recording-channel time-reversal-mirror, which in turn relies on time reversal invariance and spatial reciprocity of the classical wave equation, are introduced. In analogy with quantum fidelity, we employ scattering fidelity techniques which work by comparing response signals of the scattering region, by means of cross correlation and mutual information of signals. The performance of the sensing techniques is compared for various perturbations induced experimentally in an acoustic resonant cavity. The acoustic signals are parametrically processed to mitigate the effect of dissipation and to vary the spatial diversity of the sensing schemes. In addition to static boundary condition perturbations at specified locations, perturbations to the medium of wave propagation are shown to be detectable, opening up various real world sensing applications in which a false negative cannot be tolerated.

Detecting small changes inside enclosures with complicated boundary conditions can be of practical importance. The small changes inside such enclosures can either be perturbations of the boundary conditions or the medium of wave propagation. Examples of practical situations where such sensitive detection capabilities

are beneficial include the following: strict surveillance of the interior of an unoccupied building, scrutiny of a potentially harmful re-arrangement of objects inside an enclosure being transported, supervision of a tightly sealed chamber for gas leaks, inspection of a confined fluid for hazardous turbulence, etc. In each of these circumstances, false negatives may not be tolerated and it is essential to have a sensitive detection mechanism with broad spatial coverage.

A traditional approach of monitoring a complicated enclosure is to use a network of several wave-based sensor units each monitoring a limited region of the enclosure. Our approach is to use a single, cost effective wave based sensor unit that can monitor the complicated enclosure as a whole. Unlike traditional sensors, the sensor is not confounded by multiple reflections. Instead it actually takes advantage of, and works better using, the information of ray trajectories that ergodically explore the cavity through multiple reflections before collapsing back onto the sensor.

2.1 Introduction

In the limit where the wavelength is small compared to the characteristic size of the enclosure, wave propagation inside the enclosure can be modeled using ray trajectories. The irregularities in the boundaries of the enclosure results in sensitive dependence of the trajectories of the rays on their initial conditions. This property is known as "ray chaos". As usually defined, chaos is a property associated with nonlinear dynamical systems, and linear wave systems cannot be chaotic [3].

However, wave systems whose classical (small wavelength) limit is ray chaotic show interesting properties. The study of such wave systems is called "wave chaos" or "quantum chaos" [2]. In related work, we have created a random coupling model to understand the frequency-domain and time-domain properties of wave chaotic systems [4, 5, 6, 7], and this model has been tested through experiments on a microwave resonator [9, 10].

The underlying ray chaos in a wave chaotic system promises to be useful in detecting small changes to the system. In this chapter, two classes of sensing techniques, which take advantage of the sensitive dependence of wave trajectories on small changes to the system, are studied. The first class of sensing techniques is based on a "propagation comparison" of two distinct wave excitations of the system. The second class of sensing techniques exploits time reversal invariance and spatial reciprocity of the wave equation; it works by comparing pulses reconstructed using a time reversal of the wave excitations of the system. These sensing techniques are tested experimentally, and their performance under various circumstances is compared quantitatively.

In this chapter, the quantum mechanical concepts of fidelity and Loschmidt echo are extended to classical waves with the goal of sensing perturbations to a scattering environment. The physical theory behind these quantum mechanical concepts is briefly discussed in Sec. 2.2. Sec. 2.3 is a summary of the literature in related areas. The operation of four different acoustic sensing techniques tested in an enclosed stairwell is explained in Sec. 2.4. In this section, an indicator value of perturbation is defined for each sensing technique. The details of signal processing

done to mitigate the effect of dissipation, and to alter the spatial range sensitivity of the sensors is also included in Sec.2.4. Sec. 2.5 explains a method to standardize the indicator values of perturbation of the different sensing techniques to enable consistent comparisons. The performance of the sensing techniques for perturbations made at different locations in the stairwell is summarized in Sec. 2.6. Sec. 2.7 contains some comments on the relative merits of these different sensing techniques and discusses some of the experimental limitations. Finally, a brief conclusion is presented in Sec. 2.8.

2.2 Theory

Wave chaotic systems have wave scattering properties that are quite sensitive to small perturbations of the scattering environment. One can define two mathematically equivalent measures of this sensitivity in the context of quantum mechanics; these are the quantum fidelity and the Loschmidt echo (LE) [13, 14]. Each of these mathematically equivalent quantities measures the sensitivity of the dynamics of a quantum mechanical system to small perturbations of its Hamiltonian.

The LE can be defined as follows. A system is prepared in a given initial state $|\Psi(0)>$, propagated forward in time under an unperturbed time-reversible Hamiltonian H to some time t, $|\Psi(t)>= U(t)|\Psi(0)>$ where $U(t) = exp(-iHt/\hbar)$ is the time evolution operator. At that time the evolution is stopped and the Hamiltonian is perturbed by a small amount H', so that $H \rightarrow H + H'$. The system is then propagated backward in time under the perturbed Hamiltonian $H + H'$ to

create another state $U'(-t)U(t)|\Psi(0) >$ where $U'(-t) = exp[i(H + H')t/\hbar]$. The overlap of this forward and backward propagated state with the initial state is known as the Loschmidt echo (LE), $LE_{H'}(t) =< \Psi(0)|U'(-t)U(t)|\Psi(0) >$.

The formula above for the LE can also be interpreted as the overlap of two different final states of the system which started out from the same initial state, $\Psi(0)$, but have been propagated forward in time with different Hamiltonians, namely H and $H+H'$. Such a different interpretation of the same quantity defines the quantum fidelity. The quantum fidelity is unity in the absence of perturbations (i.e. $H' = 0$) for any H and t. However, in the presence of perturbations the quantum fidelity will decay with t at a rate depending on H and the perturbation. It is worth noting that despite their mathematical equivalence the implementation details of the computation or measurement of these quantities can be quite different, as we shall see below.

The theoretical equivalence of the Loschmidt echo and quantum fidelity motivates the exploration of their classical wave analogs with the goal of developing a practical perturbation sensor. In this paper we experimentally investigate two classes of sensing techniques which extend these two quantum mechanical concepts to classical waves. The paper devises a tunable sensor that overcomes the effects of dissipation in classical waves, and as a consequence, also creates a sensor with adjustable spatial range coverage. A statistical Figure of Merit is defined to compare the relative merits of the different sensing techniques developed. The Figure of Merit defined also helps to choose an optimum set of parameters for sensing a given perturbation.

The classical wave analog of the Loschmidt echo is implemented using a time reversal procedure which involves the following steps. Suppose that there is a cavity whose response to incident input signals can be characterized by a linear, causal, time invariant system. Let the reflected system response to an incident impulse be $s(t)$; the corresponding Fourier Transform of the impulse response (i.e. the transfer function) is denoted by $\hat{s}(\omega)$, which is a function of the Fourier frequency transform variable ω (in what follows we consider ω to be real). The first step of the time reversal procedure is to inject a narrow band, pulse modulated, incident input signal $a(t)$ into the system and to retrieve the resulting reflected output $b(t)$. The Fourier Transforms of these signals obey the relation $\hat{b}(\omega) = \hat{s}(\omega)\hat{a}(\omega)$, where, because $b(t)$ and $a(t)$ are real, $\hat{s}^*(\omega) = \hat{s}(-\omega)$. After recording $b(t)$, consider time reversing it and reinjecting it as an incident signal $b(-t)$; the Fourier Transform of $b(-t)$ is $\hat{b}(-\omega)$. The system's response to $b(-t)$ is denoted by $b'(t)$. The Fourier Transform of $b'(t)$ is given by $\hat{b}'(\omega) = \hat{s}(\omega)\hat{b}(-\omega) = \hat{s}(\omega)\hat{s}(-\omega)\hat{a}(-\omega) = |\hat{s}(\omega)|^2\hat{a}(-\omega)$. This expression is examined for different loss mechanisms in the system as follows.

For a lossless system, the scattering transfer function obeys the relation $|\hat{s}(\omega)|^2 = 1$. Thus, in the lossless case, $\hat{b}'(\omega) = \hat{a}(-\omega)$ holds, which implies that $b'(t) = a(-t)$. This means that a time reversed version of the original input, $a(t)$, is recovered after $b(-t)$ is injected into a lossless system. Thus, for the lossless case, the classical analog of the Loschmidt echo is unity, and the time reversal procedure described here is 'perfect'.

For a system that is lossy, $|\hat{s}(\omega)|^2$ generally depends on ω. As a result, the exact time reversed version of the original pulse is not expected to be reconstructed

for the lossy case. This result will be used to justify the experimental imperfection of the time reversal procedure explained in Sec. 2.4.2.2.

Next, consider a special case of a lossy system which has uniform loss. To motivate the definition of uniform loss, first consider a lossless situation in which temporally sinusoidal waves inside the scattering region are described by the wave equation $[\nabla^2 + (\omega/v)^2]\Psi = 0$, where v is the wave velocity, and the dependent variable Ψ is subject to a lossless ω-independent boundary condition on the boundaries of the scattering region. In this lossless case, the assumed solution to the scattering problem is described by a scattering coefficient $\hat{s}_0(\omega)$, where $|\hat{s}_0(\omega)|^2 = 1$; here, the subscript zero denotes the lossless case. Now assume that loss is added uniformly in space to the medium, but not to the boundary conditions. For small loss and a wide range of loss mechanisms, this modifies the wave equation within the scattering region via the replacement $\omega \rightarrow \omega + i\gamma$. Furthermore, we assume that any ω-dependence of the loss rate γ is negligible within the frequency bandwidth of the incident pulse $a(t)$. Since the only ω-dependence of the scattering problem is assumed to occur in the wave equation, the transfer function of the uniformly lossy system, $\hat{s}(\omega)$, is given by $\hat{s}(\omega) = \hat{s}_0(\omega + i\gamma)$. Therefore, for the uniform loss case, the Fourier Transform of $b'(t)$ defined above is given by $\hat{b}'(\omega) = \hat{s}_0(\omega + i\gamma)\hat{s}_0[-(\omega + i\gamma)]\hat{a}(-\omega)$. Once again, $\hat{s}_0(\omega + i\gamma)\hat{s}_0[-(\omega + i\gamma)]$ generally depends on ω, and hence the time reversal procedure is not expected to work perfectly even in the uniform loss case; in other words that $b'(t)$ is generally different from $a(-t)$.

However, we now argue that, if the uniform loss in the system is compensated by applying a proper time exponential amplification to $b(t)$, the time rever-

sal procedure will still work. The exponential amplification involves multiplying $b(t)$ by $\exp 2\gamma t$. The time reversed version of this exponentially amplified signal is $b(-t)\exp -2\gamma t$, with a corresponding Fourier Transform $\hat{b}[-(\omega + i2\gamma)]$. The Fourier Transform of the response of the system to $b(-t)\exp -2\gamma t$ is given by $\hat{b}'(\omega) = \hat{s}(\omega)\hat{b}[-(\omega + i2\gamma)]$. Here, $\hat{s}(\omega)$ can be written as $\hat{s}_0(\omega + i\gamma)$ and $\hat{b}[-(\omega + i2\gamma)]$ can be written as $\hat{s}[-(\omega + i2\gamma)]\hat{a}[-(\omega + i2\gamma)]$. After substituting these expressions and simplifying we get $\hat{b}'(\omega) = \hat{s}_0(\omega + i\gamma)\hat{s}_0[-(\omega + i\gamma)]\hat{a}[-(\omega + i2\gamma)]$. The expression $\hat{s}_0(\omega + i\gamma)\hat{s}_0[-(\omega + i\gamma)]$ is identically one for $\gamma = 0$ and all as this is the lossless case. For arbitrary γ we note that the product is an analytic function of ω. Thus, by analytic continuation it is also equal to one for any γ. Therefore, $\hat{b}'(\omega) = \hat{a}[-(\omega + i2\gamma)]$. In the time domain, $b'(t) = a(-t)\exp -2\gamma t$. If the time duration of the original input signal, $a(t)$, is short compared with $1/\gamma$, then , $b'(t) \approx a(-t)$. Therefore, if the loss in the system is uniform, then the time reversal procedure is expected to approximately work with the help of the exponential amplification. This is our motivation to use exponential amplification, described in Sec. 2.4.3, assuming that the loss in the system roughly approximates the case of a uniform loss over the bandwidth of the original input signal.

While uniform loss does not strictly apply when there are reflection losses at the boundaries (generally these depend on angle of incidence), we still might expect that the uniform loss case applies approximately. To justify this expectation, we think of $\hat{s}(\omega)$ as resulting from multiple ray paths originating from the port and then returning to it after following paths that bounce from the scatterer boundaries multiple times. Insofar as the loss over such a path is approximately proportional to

the path length (travel time), the uniform loss approximation is expected to apply. Furthermore, if these paths are long and involve many reflections, their complicated, chaotic, nature implies that the net reflection loss would involve an average of the losses over many different incidence angles of the rays on the boundary. Thus, approximately ergodic behavior of chaotic rays implies a self-averaging process over different incidence angles and approximately uniform loss for long ray paths.

2.3 Previous Related Work

The idea of quantifying perturbations to a system using either a "propagation comparison" of two different final states of the system obtained from a given initial state, or a comparison of an initial state with a final state of the system obtained by a time reversal mirror has been explored previously. The concept of quantum fidelity which quantifies the sensitivity of the dynamics of a quantum mechanical system to small perturbations of its Hamiltonian is well developed [13, 14]. The Loschmidt echo makes connection to spin-echo experiments widely used in nuclear magnetic resonance [17].

The concept of the Loschmidt echo has been extended to classical waves using "time-reversal mirrors" for acoustics [21, 22] and electromagnetics [23, 24, 25]. Ideally, time-reversal mirrors operate by collecting and recording a propagating wave as a function of time, and at some later time they propagate it in the opposite direction in a time-reversed manner. Experimentally, it is not generally possible to mirror all waves in this manner. Experimental time-reversal mirrors can however be realized

in the special case of confined systems with highly reflective walls (so called 'billiard' systems) and classically chaotic ray dynamics such as those considered here. Under these conditions a single-channel time-reversal mirror can very effectively approximate the conditions required to measure the Loschmidt echo using classical waves [25, 26]. The experimental set up for the measurement of the Loschmidt echo can be further simplified by exploiting the spatial reciprocity of the wave equation [18, 19]. Time-reversal mirrors have found a wide range of practical applications such as crack imaging in solids [31], and improved acoustic communication in air [47], among other things. Recently, it was proposed that time reversal mirrors could also be applied to quantum systems. [29]

On the other hand, the concept of quantum fidelity has been applied to classical waves as in the study of the Scattering Fidelity of acoustic waves, which is, practically speaking, the correlation between signals as a function of time [15, 51, 52, 53, 54]. The relative merits of the cross correlation and mutual information of acoustic signals in the context of underwater source detection has been studied, for example, in Ref. [16].

2.4 Experiments

The goal of our experiment is to test the sensitivity of different sensing techniques to small perturbations of a monitored acoustic cavity. A two story tall stairwell of dimensions 6m deep x 2.5m wide x 6.5m high serves as our enclosure under surveillance. [See Fig. 2.1] A Samson C01U microphone and a desktop computer

speaker that are about 1m apart are set up inside the stairwell, and are controlled by a laptop computer that is stationed outside the enclosure. This is the common experimental setup for all the sensing techniques tested. In general, the sensing techniques rely on measurements before and after a perturbation to the cavity. In Sec. 2.6, results on three different classes of perturbations are presented; these are: i) static boundary condition perturbations (i.e., insertion of an object) at six specified locations in the cavity, ii) perturbation of the medium of wave propagation in the cavity, and iii) global perturbation to the cavity. Next, the peculiarities of each sensing technique is discussed, and an indicator value of perturbation is defined for each sensing technique.

2.4.1 Sensing based on "Propagation Comparison"

The sensing techniques that rely on "propagation comparison" work as follows. The first step is to broadcast a short pulse of a carrier signal into the cavity [See Fig. 2.2(a)]. In the experiment discussed here, an acoustic pulse with a carrier frequency of 7kHz and a Gaussian envelope with time width of 1ms is broadcast into the stairwell. A typical input signal is shown in Fig. 2.3(a).The carrier wave has a wavelength that is much smaller than the typical size of the cavity so that the semiclassical limit applies. The time duration and envelope of the pulse are chosen to keep the bandwidth of the pulse narrow enough to minimize the additive background noise in the cavity, which cannot be mitigated by simple band pass filtering. A center frequency and bandwidth of the pulse which result in a relatively

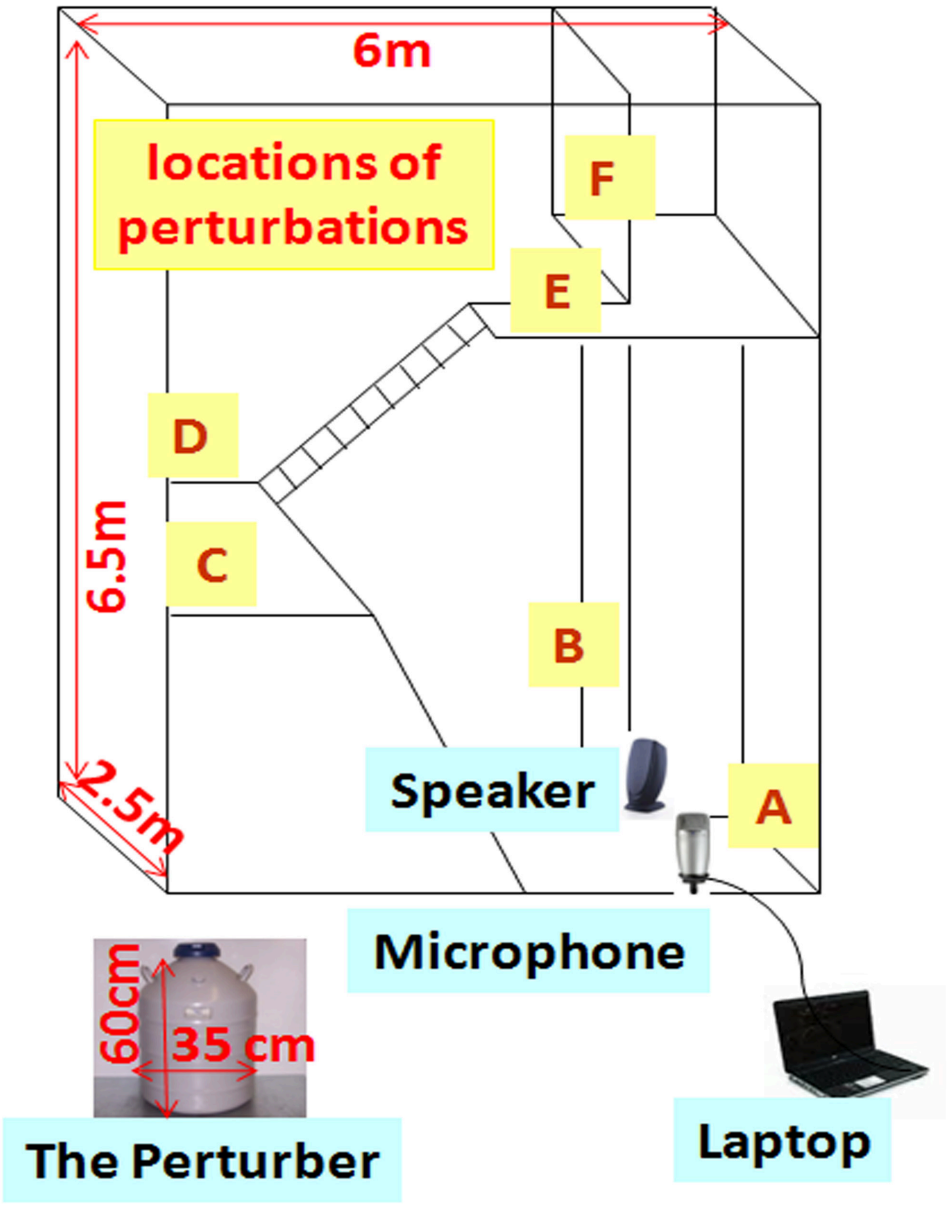

Figure 2.1: The experiment is conducted inside a stairwell with cinderblock walls and tile floors. The locations of perturbations chosen to exemplify short, medium, and long range detection attempts, both at concealed and nonconcealed locations, with respect to the sensor, are labeled with letters A to F. The inset shows the perturbing object that is introduced at the various locations AF.

strong coupling of the pulse energy into the cavity are chosen.

The second step of these sensing techniques is recording the response of the cavity to the stimulus pulse; this response is called the sona signal. Fig. 2.3(b) shows a typical sona signal from the stairwell. The sona is band pass filtered using a pass-band that matches the bandwidth of the original pulse. The sona effectively contains multiple reflections of the pulse off different parts of the stairwell and extends in time for many pulse durations. A baseline sona signal is recorded by the microphone before perturbing the cavity [See Fig. 2.2(b)]. For the case of 'boundary condition perturbation', the stairwell is perturbed by inserting a cylindrical perturbing object, which has just about 0.1% of the total volume of the stairwell. The perturber, which is shown as an inset in Fig. 2.1, is placed at one of the six perturbation locations labeled A through F in Fig. 2.1. Then, the pulse is rebroadcast into the perturbed stairwell [See Fig. 2.2(c)], and the resulting perturbed sona is recorded by the microphone [See Fig. 2.2(d)]. The baseline sona, which is collected before the perturbation, and the perturbed sona, which is collected after the perturbation, are compared in one of the following ways giving rise to two sub-classes of sensing techniques by " propagation comparison". We refer to these techniques as Sensing by Cross Correlation (SCC) and Sensing by Mutual Information (SMI).

2.4.1.1 Sensing by Cross Correlation (SCC)

One way of comparing the sonas before and after perturbation involves computing the maximum of their cross correlation. As can be seen in Eq. 2.1 and Eq. 2.2

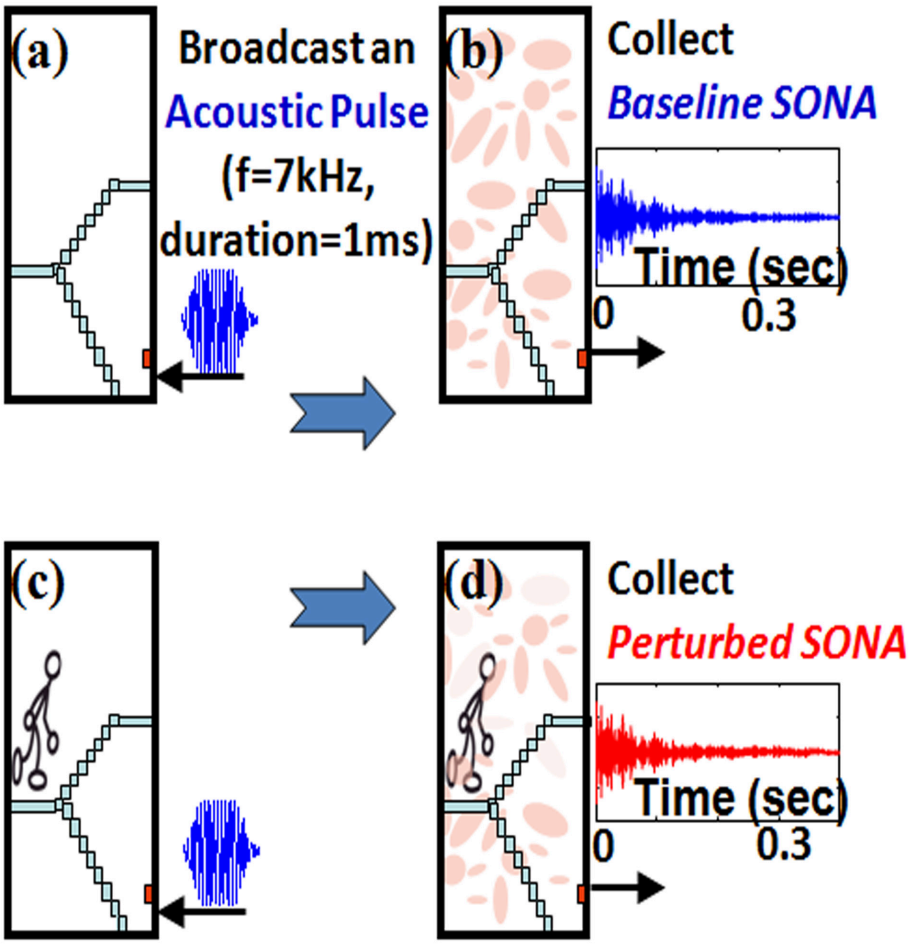

Figure 2.2: Schematic operation of a sensor based on propagation comparison. An acoustic pulse is broadcast into the stairwell in (a) and (c). The resulting sona signals are recorded in (b) and (d). In (c) and (d), the cavity is perturbed. The sensor works by comparing the baseline and perturbed sonas through either cross correlation or mutual information. The red rectangle, which is at the bottom right corner of the schematic of the stairwell, schematically shows the speaker and microphone.

below, this approach is inspired by the Scattering Fidelity [15, 51, 52, 53, 54]. Consider two time-domain sona signals that are represented as vectors, X and Y, of voltage sample values that can be indexed in time. The cross correlation, $(X * Y)[n]$ (Eq. 2.1), of these two signals is computed by finding their magnitude-normalized dot product while applying an index shift, n, between the signals; the cross correlation is a function of the index shift applied between the signals.

$$(X * Y)[n] = \frac{\sum_{m=1}^{m=l} X[m]Y[m+n]}{\|X\|\|Y\|} \tag{2.1}$$

Here, the numerator of the right hand side represents the dot product between the sona vectors X and Y, whose contents are shifted by index n with respect to each other; for a given value of n, l is the maximum index in which both $X[l]$ and $Y[l+n]$ have a well defined value. The denominator represents the product of the magnitudes of the sona vectors X and Y. The maximum of the cross correlation values (taken over all possible index shifts, n) is used as an indicator value of perturbation, I_{SCC}, for the sensing technique SCC;

$$I_{SCC} = Maximum_n\{(X * Y)[n]\} \tag{2.2}$$

If there is no perturbation in the cavity, the indicator value of perturbation for SCC (I_{SCC}) is expected to be 1; otherwise I_{SCC} is generally a number between 0 and 1.

The reason for applying an index shift between the sonas while computing their normalized dot product, and later considering the maximum of the cross correlation, is as follows. The sona signals measured before and after the perturbation are digitized using slightly different time bases. In general, this is due to variations in data acquisition triggering. Thus, it is essential to align the sona signals by

applying an appropriate relative index/time shift between them before considering the resulting correlation value; typically, a relative time shift of at most $20ms$ (i.e. an index shift of at most 880) is applied between the sonas.

2.4.1.2 Sensing by Mutual Information (SMI)

An alternative method of comparing the two sona signals is to measure their mutual information. In the context of this computation, each sona is considered as a random variable, X, taking on different voltage values as time increases. A histogram of the voltage values of a sona can be constructed using equally spaced bins. The size of these bins in Volts is determined by the inherent voltage fluctuations due to measurement noise. For this experiment, different bin sizes were tried and $1mV$ (which is also the measurement noise level) is chosen as it resulted in an optimal detection capability of the SMI technique. Thus, slightly different voltage values of the sona, which are all within an interval whose width is the typical noise level, are considered as a single voltage value for the purpose of construction of the histogram. The probability mass function, $p(x)$, of the sona is readily derived from the histogram constructed; $p(x)$ represents the probability that sona X has a voltage value of x. The entropy of the sona signal, which quantifies the information content of the sona in bits, is denoted as $H(X)$.

$$H(X) = -\sum_{x \epsilon X} p(x) \log_2 p(x) \tag{2.3}$$

All the voltage values that the sona could take on after the binning process are considered in this formula for the entropy.

The mutual information of sonas X and Y, which are considered as random variables, is denoted by $I(X;Y)$, and serves as the indicator value of perturbation, I_{SMI}, for the SMI technique.

$$I_{SMI} = I(X;Y) = \sum_{x \epsilon X} \sum_{y \epsilon Y} p(x,y) \log_2 (\frac{p(x,y)}{p(x)p(y)}) \tag{2.4}$$

The mutual information can be described as the difference between the sum of the individual entropies of the sonas and their joint entropy $I(X;Y) = H(X) + H(Y) - H(X,Y)$. The calculation is similar to that of the entropy except that now the joint probability mass function of sonas X and Y, $p(x,y)$, is involved (Eq. 2.4); the marginal probability mass functions of X and Y are denoted by $p(x)$ and $p(y)$. The joint probability mass function $p(x,y)$ assigns the probability that sona X and Y take on voltage values x and y respectively at the same time. Once again, the bins have a size on the order of the noise level in the data.

As discussed in Sec. 2.4.1.1, the sona signals X and Y, which are collected under slightly different time bases, are time aligned based on their maximum correlation value before their correlation is considered as an indicator value of perturbation. By the same token, the computation of the joint probability $p(x,y)$ of event $(X = x, Y = y)$, which is used in determining the mutual information (Eq. 2.4) of two sona signals X and Y, is done after the sonas are aligned with respect to their time index. The alignment can be achieved by finding a time index shift between the sona signals which maximizes their mutual information.

The mutual information is zero if the two signals being compared are statistically independent. In general, the mutual information takes on values ranging from

zero to a maximum value, which is the entropy value of a sona signal in the case of two identical sonas. A typical sona signal in these experiments has an entropy of about 5 bits; whereas, the mutual information between two sonas collected from two nominally identical configurations of the stairwell is typically about 2 bits.

2.4.2 Sensing based on Time Reversed Wave Propagation

The extension of the Loschmidt echo to classical waves is tested by using a one channel time reversal mirror for acoustic waves in the same stairwell. As in the experiment discussed above, an acoustic pulse with $7kHz$ center frequency and a Gaussian envelope of $1ms$ time width is broadcast into the stairwell. [See Fig. 2.4(a)] The resulting sona is measured by the microphone and digitized as shown in Fig. 2.4(b). The digitized and band-pass filtered sona is time reversed before it is broadcast back into the stairwell through the speaker. [See Fig. 2.4(c)] To carry out a full and complete time-reversed wave propagation process, the time reversed sona should be broadcast back into the stairwell from the location of the microphone, where the sona was collected. However, spatial reciprocity of the wave equation is employed which allows us to broadcast the time reversed sona from the speaker at its original location without the need to interchange the location of the two transducers. The time reversed sona propagates in the cavity and reconstructs as a time reversed pulse at the location of the microphone, where it is recorded. [See Fig. 2.4(d) and Fig. 2.3(c)] The time reversed pulse is periodically generated using the same time reversed sona signal and possibly different conditions of the cavity

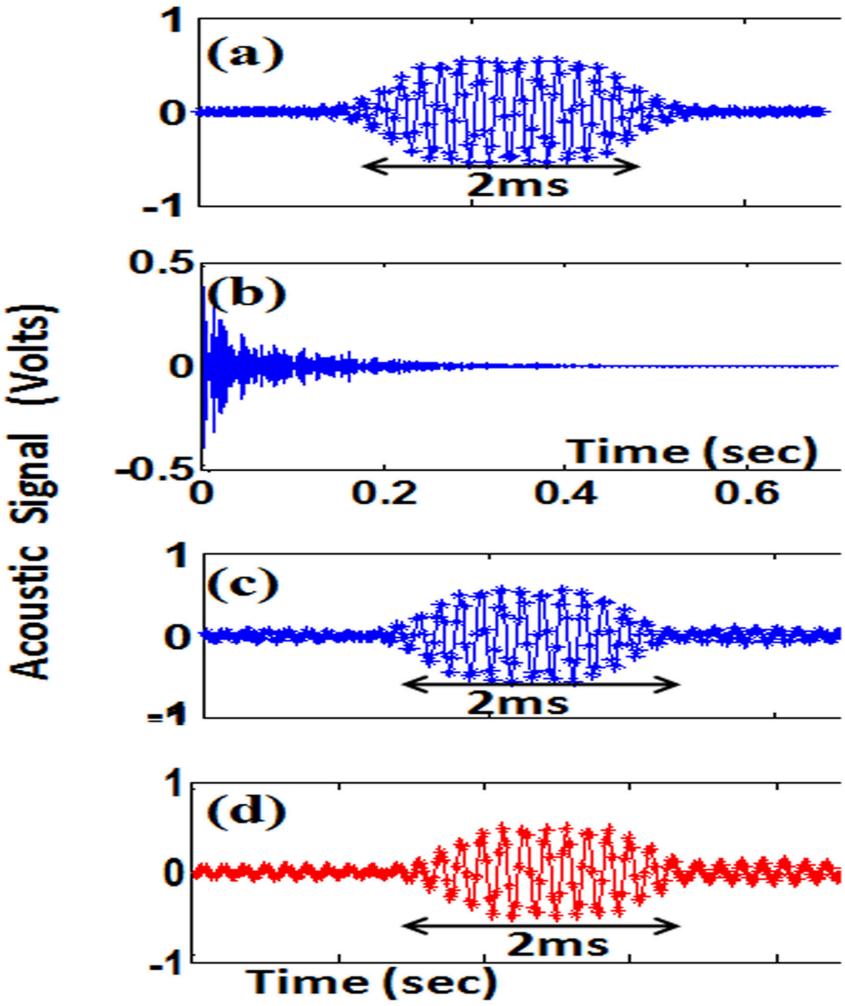

Figure 2.3: (a) The OP broadcast into the stairwell, (b) sona, (c) a baseline time reversed reconstructed pulse (BRP), (d) a perturbed time reversed reconstructed pulse (PRP). All parts show an acoustic signal (in volts) vs time.

monitored. If a perturbation occurs [See Fig. 2.4(e)], the resulting reconstructed time reversed pulse shown in Fig. 2.4(f) will be different from the reconstructed pulse shown in Fig. 2.4(d).

In general, the sensing techniques based on time reversal work by comparing two time reversed pulses reconstructed under baseline and perturbed conditions of the cavity; hence, such sensing techniques are called Chaotic Time Reversal Sensors (CTRS). The time reversed pulses reconstructed under a baseline and a perturbed condition of the cavity are referred to as a Baseline Reconstructed Pulse (BRP) and a Perturbed Reconstructed Pulse (PRP), respectively. A typical BRP and PRP are shown in Fig. 2.3(c) and Fig. 2.3(d) respectively. The comparison between BRP and PRP, which have a brief time duration, is computationally inexpensive and can be done in a number of different ways. Two representative methods of comparing these signals which give rise to two versions of the CTRS, namely CTRS1 and CTRS2, are discussed. CTRS1 is based on the comparison of the peak to peak amplitude of BRP and PRP. Alternatively, CTRS2 is based on the computation of a normalized correlation of the brief pulses PRP and BRP with a time reversed version of the original pulse, which is shown in Fig. 2.3(a).

2.4.2.1 Chaotic Time Reversal Sensor 1 (CTRS1)

Comparison of the BRP and PRP based solely on their peak to peak amplitude is computationally the simplest and most efficient. The ratio of the peak to peak amplitudes of the PRP to BRP is defined as an indicator value of perturbation for

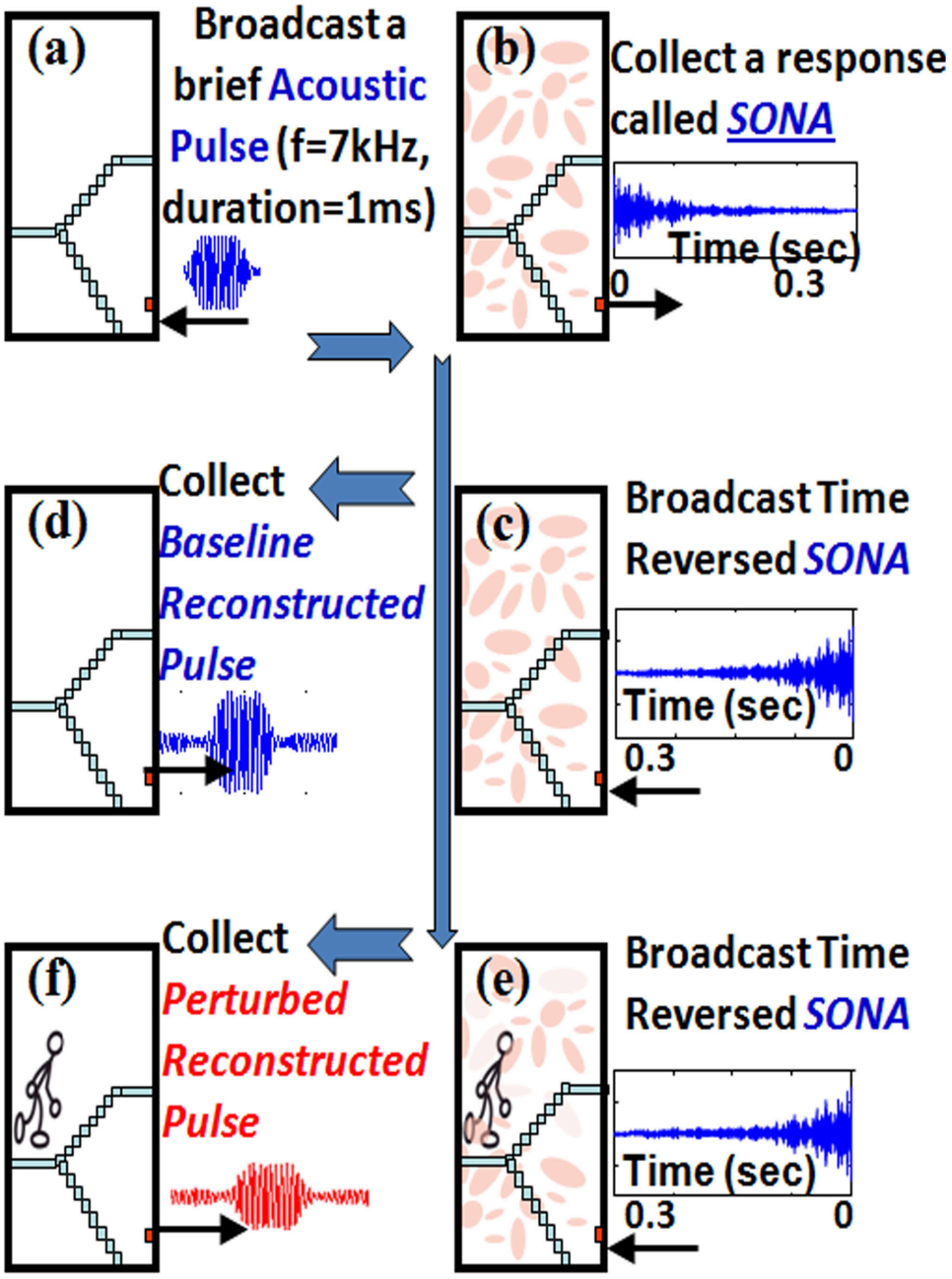

Figure 2.4: Schematic operation of the CTRS, which is based on the extension of the LE to classical waves. A sequence of steps illustrated in (a)(d) are carried out to measure the BRP. Using the sona collected in (b), the steps illustrated in (e) and (f) are carried out to measure the PRP. The CTRS works by comparing the baseline and perturbed pulses collected.

CTRS1, I_{CTRS1}.

$$I_{CTRS1} = \frac{PkPk_Amplitude_{PRP}}{PkPk_Amplitude_{BRP}} \tag{2.5}$$

This ratio is expected to be about 1 if the perturbed condition of the cavity is the same as its baseline condition. In the case of an actual perturbation, the ratio is a number smaller than 1. The contrast in the amplitude of BRP and PRP can be seen in Fig. 2.3(c) and Fig. 2.3(d).

2.4.2.2 Chaotic Time Reversal Sensor 2 (CTRS2)

An alternative method to compare BRP and PRP is based on a normalized correlation that is analogous to the definition of the Loschmidt echo. Consequently, this method involves the use of the Original Pulse (OP), which is broadcast into the cavity in order to collect the sona. The OP broadcast by the speaker is measured in a separate experiment carried out in an anechoic chamber whose walls are acoustic absorbers. Fig. 2.3(a) shows a typical measured OP. Once the OP is measured and digitized it is numerically time reversed resulting in the Reversed Original Pulse (ROP). In principle, the ROP is expected to be identical to the BRP. However, this is not the case because the one channel acoustic time reversal mirror is not perfect. The imperfections are due to the finite time recording of the sona [55], and the dissipation in the cavity [18]; the imperfection of the time reversal process due to loss is also discussed in Sec. 2.2. Additive noise from the cavity within the bandwidth of the OP also plays a role in the incongruity of the ROP and BRP.

The correlation of the ROP and the BRP is used to quantify the overall limita-

tions of the time reversal mirror. If the experiment were ideal, in the sense that the sona were recorded for an infinite amount of time in a non-dissipative and noiseless system, this correlation would be 1 for a ray chaotic system; in these experiments this correlation is roughly 80%. This correlation is used below to normalize the correlation of the ROP and the PRP. The ratio of these two correlations is the indicator value of perturbation for the CTRS2 technique, I_{CTRS2}.

$$I_{CTRS2} = \frac{\frac{<PRP,ROP>}{\|PRP\|\|ROP\|}}{\frac{<BRP,ROP>}{\|BRP\|\|ROP\|}} \tag{2.6}$$

Here, pulses PRP, ROP, and BRP are considered as vectors of voltage values that can be indexed in time. Thus, the numerator of I_{CTRS2} is the dot product of PRP and ROP divided by the product of their magnitudes. Likewise, the denominator of I_{CTRS2} is the dot product of BRP and ROP divided by the product of their magnitudes. Note that the quantity in the numerator of this I_{CTRS2} is analogous to the definition of the Loschmidt echo. The normalization in the denominator is needed to ensure that I_{CTRS2} is 1 in the absence of a perturbation. In the presence of a perturbation the I_{CTRS2} is a number between 0 and 1.

Yet another way of comparing the BRP and PRP is their correlation, $< BRP, PRP > /(\|BRP\|\|PRP\|)$. However, we have experimentally demonstrated that such an approach does not yield a reliable indication of whether a perturbation has happened or not. In other words the correlation of two time reversed pulses that are reconstructed before and after perturbation is not statistically distinguishable from the correlation of two time reversed pulses that are reconstructed under nominally identical conditions of the cavity. Hence, this third variety of the CTRS

is not discussed further.

2.4.3 Effects of Dissipation and Processing the Sona Signal

The sensing techniques discussed so far face the problem of dissipation of classical waves which effectively limits the sensitivity and spatial coverage of the sensor. The dissipation brings about an exponential decay of the signal set up by the initial broadcast of the acoustic pulse. This exponential decay is seen in the envelope of the sona signal recorded, from which the $1/e$ decay time is estimated. [Fig. 2.5(a)] A typical $1/e$ decay time of the sona signals collected from the stairwell is about 0.1 seconds. This measured $1/e$ decay time, τ, is reasonably consistent with the $60dB$ decay time of the stairwell estimated from Sabine's formula.

$$T_{60dB} = \frac{cV}{\sum_m S_m \alpha_m} \tag{2.7}$$

Here, the parameter $c = 0.161s/m$. Applying Sabine's formula involves estimating the volume of the cavity, $V \approx 93m^3$. In addition, the surface area, S, of each of the constituent materials of the interior of the cavity is estimated. The corresponding frequency dependent absorption coefficient, α, of the materials is found from the literature [56], and the summation in Eq. 2.7 is carried out over all the constituent materials, m, of the interior of the cavity. The interior of the stairwell has approximately $129m^2$ of painted concrete block and $46m^2$ of concrete floor; these constituent materials are known to have an absorption coefficient of 0.08 and 0.02 respectively for $4kHz$ sound waves. Using these rough estimates, the $60dB$ decay time for $4kHz$ sound waves in the stairwell is $1.3s$. From this, one estimates a $1/e$

decay time of 0.09 seconds for $4kHz$ sound waves in the stairwell, which is close to the measured $\tau = 0.1s$ at $7kHz$.

The exponential decay of the sona can be numerically mitigated by applying an exponential amplification $A(t, F)$ to the portion of the sona signal that has a signal to noise ratio of at least 1.

$$A(t, F) = \exp \frac{Ft}{\tau} \tag{2.8}$$

The time dependent amplifying function, $A(t, F)$, is a function of parameter F, and it uses the measured value of the $1/e$ decay time, τ, of the sona signal being amplified. The parameter F typically takes on values of either 0, 1, or 2. If $F = 0$, there is no exponential amplification of the sona. [See Fig. 2.5(a)] If $F = 1$, the resulting exponential amplification removes the effects of dissipation that happened during the time-forward propagation of the acoustic pulse up to the collection of the sona. [See Fig. 2.5(b)] If $F = 2$, the resulting exponential amplification removes the effects of dissipation that the sona has suffered up to its collection during time-forward propagation and also the dissipation that it will suffer as it goes through the stairwell again in a time reversed manner. [See Fig. 2.5(c)]

The motivation for applying exponential amplification is to make the sona signal closer to what it would be in the non-dissipative case. Working in the approximately non-dissipative case can expand the range of the sensor. In addition, the range of the sensor can be changed to some extent with choice of parameter value F. In Sec. 2.6.3, we shall see that global perturbations to the stairwell are detected best when the sonas are exponentially amplified to approximate the non-dissipative

case. The exponential amplification is also motivated by the theoretical results in Sec. 2.2.

Another possibility of tuning the sensor involves applying a rectangular time-gating window function to the sona. Such a window is a function of two parameters: start time (t_{START}) and stop time (t_{STOP}) (See Fig. 2.5(c)). The motivation for time-windowing the sona to change the sensitivity and spatial coverage of the sensor is founded on a 'ray propagation model' of the problem. Rays that bounce back from perturbation locations in the vicinity of the sensor get recorded at the beginning of the sona. In contrast, rays that bounce back from perturbation locations farther out from the sensor are recorded towards the end of the sona. This simple generalization of the complex ray trajectory dynamics in the stairwell motivates the possibility of windowing the sona to change the spatial sensitivity of the sensor. Thus, the t_{START} t_{STOP} parameters of the rectangular window are varied to explore this possibility of tuning the sensor's sensitivity to perturbation at various locations within the stairwell.

The rectangular time window has a rise and fall time that is designed to keep the bandwidth of the windowed sona invariant. Particularly, the rise and fall times are both on order of magnitude of the time width of the original acoustic pulse that generated the sona (i.e. $1ms$). Before a sona is windowed, it is exponentially amplified with a given F value. The amplitude of the windowed sona is then uniformly scaled to fit into the voltage dynamic range of linear output of the speaker, which is $-0.4V$ to $0.4V$. This range was determined by an experiment in an anechoic chamber with the microphone and speaker.

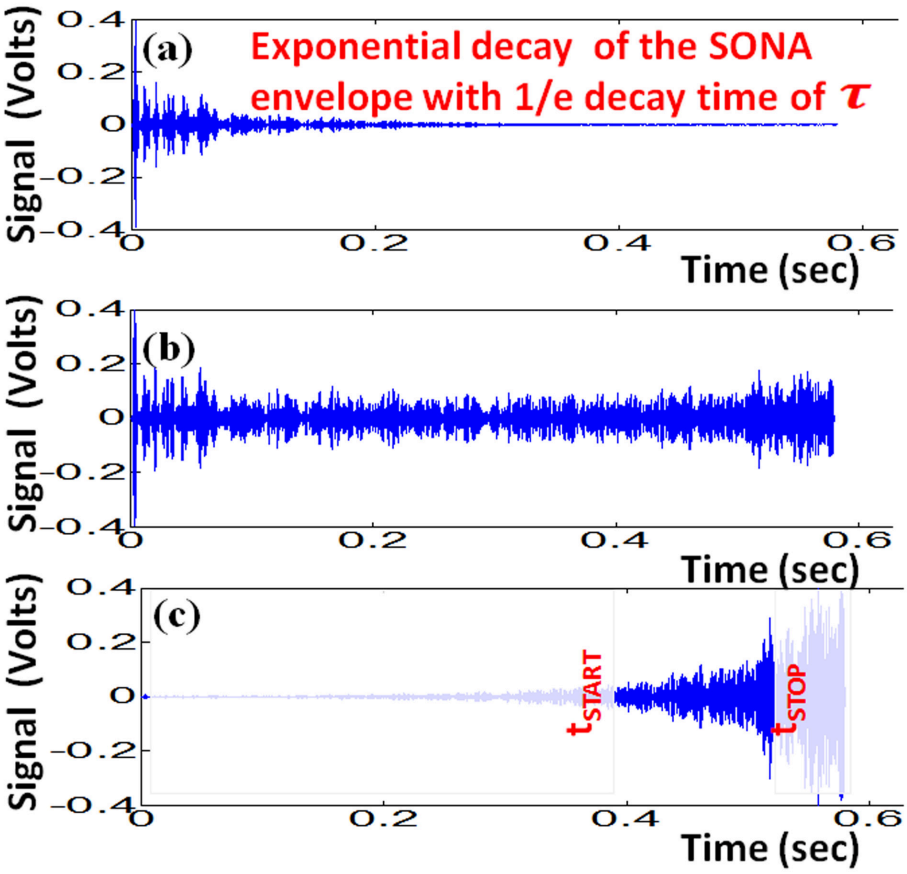

Figure 2.5: (a) A typical measured exponentially decaying sona signal, (b) exponentially amplified sona with $F = 1$, (c) exponentially amplified sona with $F = 2$ after rectangular windowing between times t_{START} and t_{STOP}.

To summarize, the sona signal is processed using the three parameters discussed above: exponent F, t_{START}, and t_{STOP}. Each of the sensing techniques discussed so far are done with various values of these parameters. For sensing techniques based on time reversal of wave propagation, the sona is processed with the appropriate parameters before it is time reversed and broadcast back into the cavity. On the other hand for the sensing techniques based on "propagation comparison", both of the sonas being compared are processed by the same exact parameter values before the computation of mutual information or cross correlation of the processed sonas are carried out.

As a caveat, the following special procedures are taken for the case of the SMI technique to improve its detection performance. The windowed sonas are not uniformly scaled to fit into the dynamic range of $-0.4V$ to $0.4V$ (mentioned above). Furthermore, the voltage values of the processed sonas are rounded off to 3 significant figures both before and after the sonas are processed (using exponential amplification and windowing); in other words, the binning of the sonas with a bin size of $1mV$ is done both before and after processing the sonas.

2.4.4 Investigation of the Tunability of the Range of the Sensor

So far, four sensing techniques have been introduced, and a mechanism to tune the range of a sensor using three parameters is established. The parameters are designed to compensate for the effects of dissipation and to alter the spatial range of the sensor, to some extent. The following experiments were done to investigate

the problem of perturbation detection at short, medium and long range.

Six different locations of perturbations, which are labeled A through F in Fig. 2.1, were chosen in the stairwell. These locations were chosen so that there are two representative locations for short (perturbation locations A and B), medium (perturbation locations C and D) and long range (perturbation locations E and F) detection attempts, respectively. Each pair of representative locations were chosen so that there is an example of a location that is concealed from the sensor (B, D, and F), and a location that is almost within the line of sight of the sensor, or at least within a couple of reflections from the sensor (A, C, and E). For each sensing technique, the baseline (unperturbed) situation involves the absence of the perturber in the stairwell, while the perturbed situation has the perturbing object located at one of the six locations A through F.

The detection experiment was systematically performed at each perturbation location using all the sensing techniques introduced above. The experiment was carefully designed to allow all the sensing techniques to be applied to a single instance of perturbation at a given location. All the sensing techniques were operated with the same set of parameter values. This experimental scheme allows for the following considerations. An optimal set of parameter values can be identified for a given sensing technique at a given perturbation location. The effectiveness of a sensing technique, which is operating at its optimal parameter values, can be gauged at different perturbation locations. The optimal detection capability of different sensing techniques can be compared at a given perturbation location. Standardization of these comparisons is discussed in the data analysis section.

2.5 Data Analysis

In the experiment section, the measurement and calculation of four different indicator values of perturbation (i.e. I_{CTRS1}, I_{CTRS2}, I_{SCC}, and I_{SMI}) corresponding to the four sensing techniques were introduced. Each of those indicator values have their own inherent uncertainty in their measurement and calculation. The range of values that the indicators take on is not uniform. Even though I_{CTRS1}, I_{CTRS2}, and I_{SCC} have the same range of values (i.e. 0 to 1), the dependence of their value on the perturbation is not necessarily the same. All these complications make the comparison of the different sensing techniques, solely using their respective indicator values of perturbation, a difficult task. This problem is solved by defining a standardized Figure of Merit (FOM) that can be calculated from the typical statistics of the indicator values of any of the techniques.

In the absence of perturbation, I_{CTRS1}, I_{CTRS2}, and I_{SCC} should ideally be 1. Whereas, I_{SMI} should have a particular value, which is closest to the typical entropy of the sona in bits, in the absence of perturbation. However, this is not always the case due to measurement uncertainties and noise that propagate through the steps of the computation of the indicators. Consider a control experiment of detection, in which we do not induce any perturbation to the cavity under surveillance. In such a control experiment, the resulting indicator values fluctuate somewhere around the ideally expected value of 1 (for $CTRS1$, $CTRS2$ and SCC), or somewhere around a value close to the entropy of the sona in bits (for SMI). The statistics of these control indicator values of perturbation are considered for each sensing technique.

Particularly, the mean, μ, and standard deviation, σ, of the control indicator values of perturbation are calculated.

If an indicator value of perturbation is much smaller than the mean of the control indicator values compared to their standard deviation, then there is a statistically significant detection. Thus, the following Figure of Merit(FOM) is defined.

$$FOM = \frac{\mu - I}{\sigma} \tag{2.9}$$

The FOM, is the ratio of the difference between the observed indicator value, I, and the mean, μ, of the control indicator values to the standard deviation, σ, of the control values. The observed indicator value of a perturbation, I, for a given instance of perturbation may itself fluctuate around some value due to noise. This results in the FOM fluctuating as well. Therefore, the FOM is averaged over 25 different realizations. Such an average FOM, $< FOM >$, also has a propagated uncertainty, $\delta_{<FOM>}$, associated with it. The difference between the average FOM and the uncertainty in the average FOM is defined as the Lower-bound of the Figure of Merit, FOM_L.

$$FOM_L =< FOM > -\delta_{<FOM>} \tag{2.10}$$

To use an abundance of caution, the FOM_L is used to ultimately decide whether or not there is a statistically reliable detection. Heuristically, if FOM_L is greater than 2, then we conclude that there is a statistically reliable detection.

The FOM_L is calculated for detection attempts using different parameter values. In what follows, the FOM_L is plotted, using a contour plot, as a function of t_{START} and t_{STOP} parameters of the rectangular time-windowing function applied

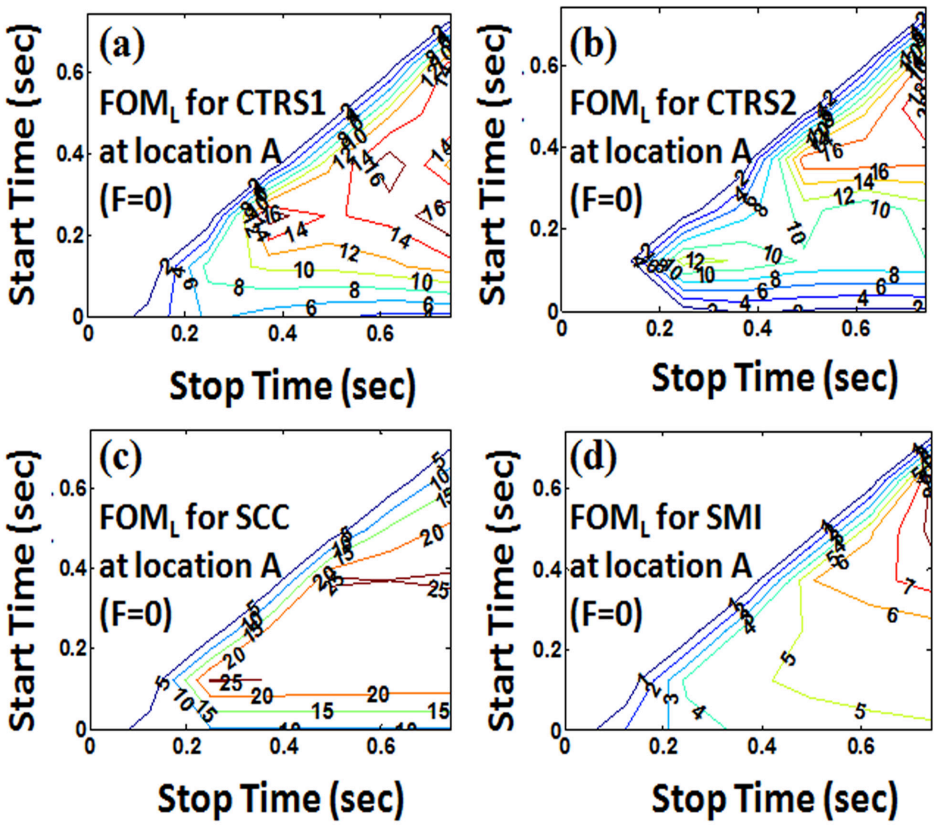

Figure 2.6: Contour plots of the lower bound on the FOM (FOM_L) as a function of start time (t_{START}) and stop time (t_{STOP}) parameters of the rectangular time windowing function applied to the sona. The plots show detection attempts at perturbation location A (indicated in Fig. 1) using $F = 0$. (a) FOM_L for CTRS1, (b) FOM_L for CTRS2, (c) FOM_L for SCC, (d) FOM_L for SMI.

to the sona. [See Fig. 2.6]These plots are done for a given value of the F parameter used to amplify the sona. Such plots are also annotated by the sensing technique that was used to generate the FOM_L and also the location of the perturbation that is being detected.

2.6 Results

2.6.1 Results on Detection of Perturbations at Specified Locations

The experiments performed can be summarized as follows. Detection attempts were made using four different sensing techniques at six different perturbation locations in the stairwell, which are labeled A through F in Fig. 2.1. The six perturbation locations are chosen to be representative of short, medium and long range detection both in a concealed and non-concealed sections of the stairwell with respect to the sensor. Each of the detection attempts using each technique were done using various parameter values. Particularly, the F parameter, which controls the exponential amplification, takes on values of 0, 1 or 2. The t_{START} and t_{STOP} of the windowing function each take on 7 equally spaced values ranging from 0 seconds to the time at which a typical sona's Signal to Noise Ratio(SNR) becomes 1, which is roughly 0.7 seconds. Therefore, there are $(7 * (7 - 1))/2 = 21$ plausible pairs of t_{START} and t_{STOP} values that constitute a rectangular sona windowing function of non-zero time width.

The FOM_L (Eq. 2.10), which is a function of t_{START} and t_{STOP}, is plotted as a contour plot for a specified F value, sensing technique and perturbation location. In

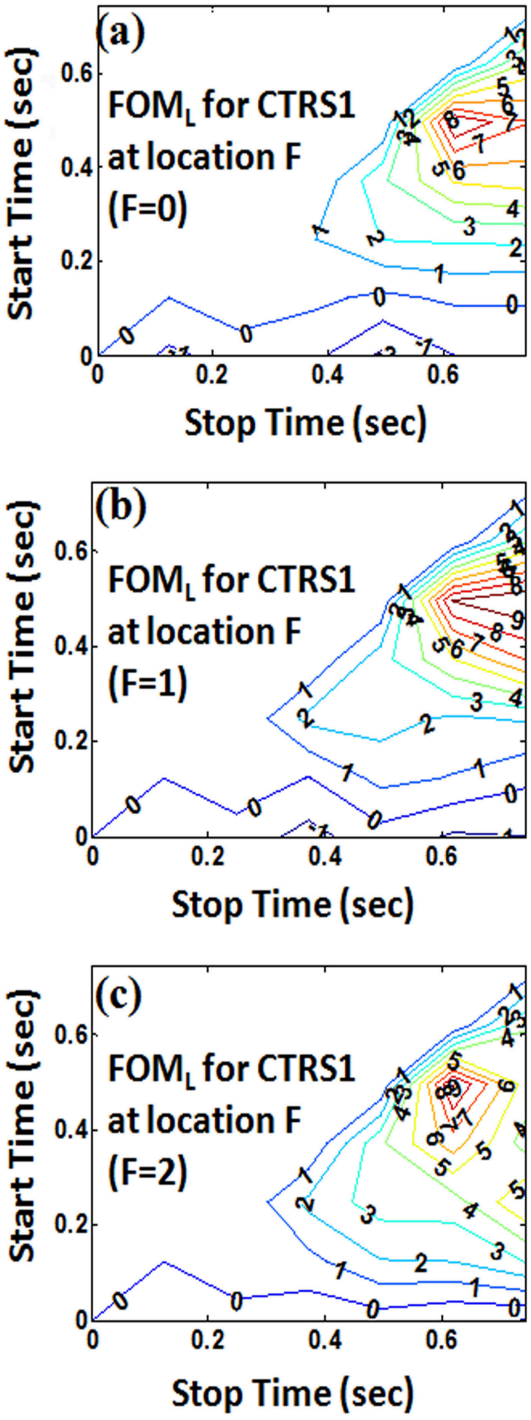

Figure 2.7: Contour plots of the lower bound on the FOM (FOM_L) as a function of start time (t_{START}) and stop time (t_{STOP}) parameters of the rectangular windowing function applied to the sona. (a) Long range detection at location F, indicated in Fig. 1, using CTRS1 with $F = 0$, (b) long range detection at location F using CTRS1 with $F = 1$, (c) long range detection at location F using CTRS1 with $F = 2$.

such contour plots, only the lower right triangle of the plane is used. Overall, since there are 6 perturbation locations, 4 sensing techniques and 3 F-values, there are 72 such contour plots for the set of experiments carried out. In this results section, a select group of these plots, which illustrate general trends, will be presented. A table that summarizes all the results is also included. [See Table 2.1] Given a perturbation location and sensing technique, the table shows the maximum FOM_L value over all parameter values tried in these experiments. The table also shows the percentage of parameter values that gave a FOM_L greater than 2, which is a conservative estimate of statistically reliable detection. The table gives an overall sense of the effectiveness of the sensing techniques, because it presents their performance in detecting perturbations at different ranges from the sensor.

In Fig. 2.6, the FOM_L is plotted for detection attempts at perturbation location A (shown in Fig. 2.1) without exponential amplification of the sona (i.e. $F = 0$). Figs. 2.6(a), (b), (c), and (d) demonstrate that the techniques of CTRS1, CTRS2, SCC, and SMI, respectively, allow for a short range and non-concealed perturbation detection over a wide range of parameter values (i.e. FOM_L is greater than 2 for a large number of rectangular windowing functions). The SMI technique has relatively smaller FOM_L values compared to the other techniques. Overall, all the sensing techniques work without the need for exponential amplification and windowing of the sona when the perturbation is in the vicinity of the sensor.

Here, Fig. 2.6(c) illustrates the connection between the calculations of the SCC technique and the traditional Scattering Fidelity [15, 51, 52, 53, 54], which has inspired the SCC technique. In Fig. 2.6(c), there is no exponential amplification

(i.e. $F = 0$). Therefore, the FOM_L values plotted near the diagonal-line of the "t_{START}, t_{STOP} contour plane" essentially come from a set of I_{SCC} values which can be plotted as Scattering Fidelity versus time of the baseline and perturbed sona signals being compared. We see that the optimal parameter region in Fig. 2.6(c) is not near the diagonal-line of the contour plane; thus, the generalized SCC technique does indeed offer greater flexibility with its three adjustable parameters (t_{START}, t_{STOP}, F), especially for perturbations that are further from the sensor, and/or hidden.

The need to process the sona comes into play when a medium or long range detection is attempted. In Fig. 2.7, the results of long range detection at concealed perturbation location F [See Fig. 2.1] are presented. The FOM_L for the CTRS1 technique is plotted with $F = 0$, $F = 1$, and $F = 2$ in Figs. 2.7(a), (b), and (c) respectively. In contrast to Fig. 2.6(a) (which shows results for short range detection by CTRS1 with $F = 0$), a smaller set of windowing parameters allow long range detection by CTRS1 with $F = 0$. Therefore, successful long range detection demands a judicious choice of windowing parameters with $F = 0$. If there is an exponential amplification with $F = 1$ or $F = 2$, there is, in this case, a slightly larger set of windowing parameters that can be used to do long range detection. However, as can be seen in Fig. 2.7, the right choice of the windowing parameters is more important in doing long range and concealed detection using CTRS1 than the value of F; this is also generally true for the CTRS2 and SCC. In general, the percentage of parameter values that allow detection decreases as the perturbation location gets farther away from the sensor, as seen in Table 2.1.

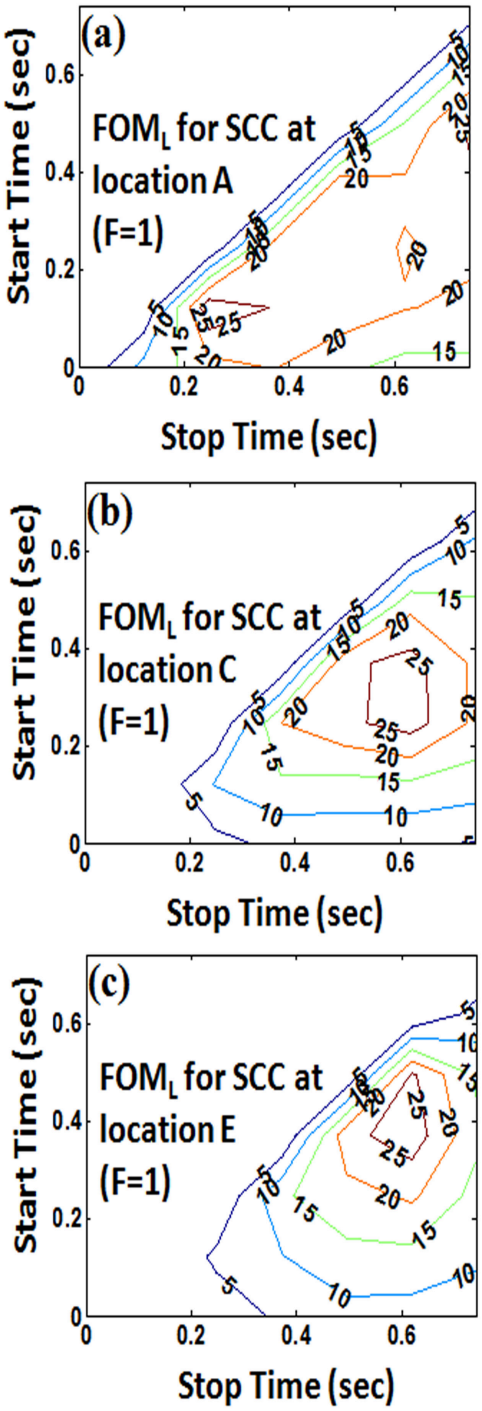

Figure 2.8: Contour plots of the lower bound on the FOM (FOM_L) as a function of t_{START} and t_{STOP} parameters of the rectangular windowing function applied to the sona. In all plots, an exponential amplification of $F = 1$ is applied to the sona. The three plots shown here show detection attempts at different locations of perturbations illustrated in Fig. 1. (a) short range detection at location A, (b) medium range detection at location C, (c) long range detection at location E.

Sensing technique		Perturbation location shown in Fig. 2.1					
		A	B	C	D	E	F
CTRS1	Maximum FOM_L value	28.9	24.6	17.8	16.0	20.1	9.9
	% of FOM_L value > 2	97%	81%	73%	71%	67%	46%
CTRS2	Maximum FOM_L value	21.7	18.0	9.9	11.5	13.1	5.8
	% of FOM_L value > 2	90%	63%	67%	32%	48%	13%
SCC	Maximum FOM_L value	32.7	33.1	33.1	22.3	30.2	7.9
	% of FOM_L value > 2	100%	95%	87%	78%	87%	24%
SMI	Maximum FOM_L value	8.3	11.2	12	8.3	15.2	3.5
	% of FOM_L value > 2	76%	71%	89%	54%	76%	6%

Table 2.1: The maximum FOM_L over all the parameter values tried is shown for each of the four sensing techniques detecting a perturbation at each of the six perturbation locations indicated in Fig. 2.1. In addition, the percentage of parameter values which gave a FOM_L that is greater than 2 is also shown.

The possibility of associating a set of optimal detection parameter values with detection of a perturbation at a particular location was investigated next. In general, as the perturbation location is farther away from the sensor, the optimal detection parameters space either shrinks and/or moves to the upper right corner of the "t_{START}, t_{STOP} plane". Fig. 2.8 illustrates this phenomena for the case of short, medium and long range detection attempts at perturbation locations A, C and E [See Fig. 2.1] respectively by the SCC. The broad swath of parameter space that is optimal for detection at short range [See Fig. 2.8(a)] shrinks as the perturbation location moves farther away from the sensor [See Figs. 2.8(b),(c)]; it also moves to the upper right corner of the plane in this case. Even though this is a consequence of the fact that the waves that bounced off the farthest perturbation location take a longer time to get back to the sensor, it is not a trivial consequence as there are multiple reflections of all the waves within the cavity.

2.6.2 Results on Detection of Perturbations of the Medium of Wave Propagation in the Cavity

So far, the results of experiments which involve detection of perturbations at six different locations in the stairwell, illustrated in Fig. 2.1, are presented. Such perturbations essentially change the boundary conditions of the cavity at a localized region. A different kind of perturbation involves perturbation of the medium of wave propagation in the cavity: For example, creating air currents will perturb acoustic wave propagation. Such perturbations naturally start out locally and may spread out throughout the medium filling the cavity in a complex manner. This motivates yet another kind of perturbation to the cavity which is global in nature. As a significant amount of time elapses, both the boundaries of the cavity and the medium within may undergo complex and spatially extensive changes due to uncontrollable thermal variations (giving rise to convection currents, for example). Next, we present the results of experiments which investigate the possibility of detecting a relatively localized perturbation to the medium of wave propagation in the cavity, and also a global perturbation to the cavity.

The medium of wave propagation in the stairwell is perturbed by remotely activating a fan which is stationed inside the stairwell about $2m$ away from the sensor. The air currents induce a phase shift, $\Delta\phi$, in the sound waves that pass through the part of the cavity in which the air is perturbed.

$$\Delta\phi \approx \frac{\Delta v}{v} k L_{path} \tag{2.11}$$

Here, v is the speed of sound, Δv is the speed of the wind, k is the wave number

of the sound wave, and L_{path} is a typical path length of travel of the sound wave through the moving air. Taking $v = 343m/s$, $\Delta v = 2m/s$, $k = \frac{2\pi}{5}cm$, $L_{path} = 1m$, gives $\Delta\phi = 0.23\pi$. Such a significant phase shift degrades the reconstruction of the time reversed pulse during the operation of the CTRS. This is because the coherent superposition of the time reversed sona is thwarted due to the phase shift that waves, which pass through the moving air, experience.

The following experiment is done to study the detectability of perturbations of the medium of wave propagation by CTRS1. A pulse is broadcast into a quiescent stairwell, and a sona is collected. The time reversed sona is then periodically broadcast into the stairwell 30 times over 9 minutes. The resulting time reversed reconstructed pulses are saved. Then, the air in the cavity is perturbed by remotely activating a mechanical fan for 15 seconds; the fan had been stationed inside the stairwell in the vicinity of the sensor. After the fan is turned off, the time reversed sona is broadcast into the stairwell 30 more times over 9 minutes. The resulting 30 additional reconstructed pulses are also saved. In this experiment, the very first time reversed reconstructed pulse is considered as a Baseline Reconstructed Pulse (BRP). All the other pulses are considered as a Perturbed Reconstructed Pulse (PRP). Then, the indicator value of perturbation for CTRS1, I_{CTRS1}, (Eq. 2.5) is constructed for each of the 59 PRP, BRP pairings. Finally, I_{CTRS1} is plotted versus time as shown in Fig. 2.9.

Fig. 2.9(a), (b), and (c) show the cases when the sona is exponentially amplified with parameter $F = 0$, $F = 1$, and $F = 2$, respectively. In all cases, the sonas are windowed with $t_{START} = 0s$ and $t_{STOP} = 0.3s$. From Fig. 2.9, it is clear when

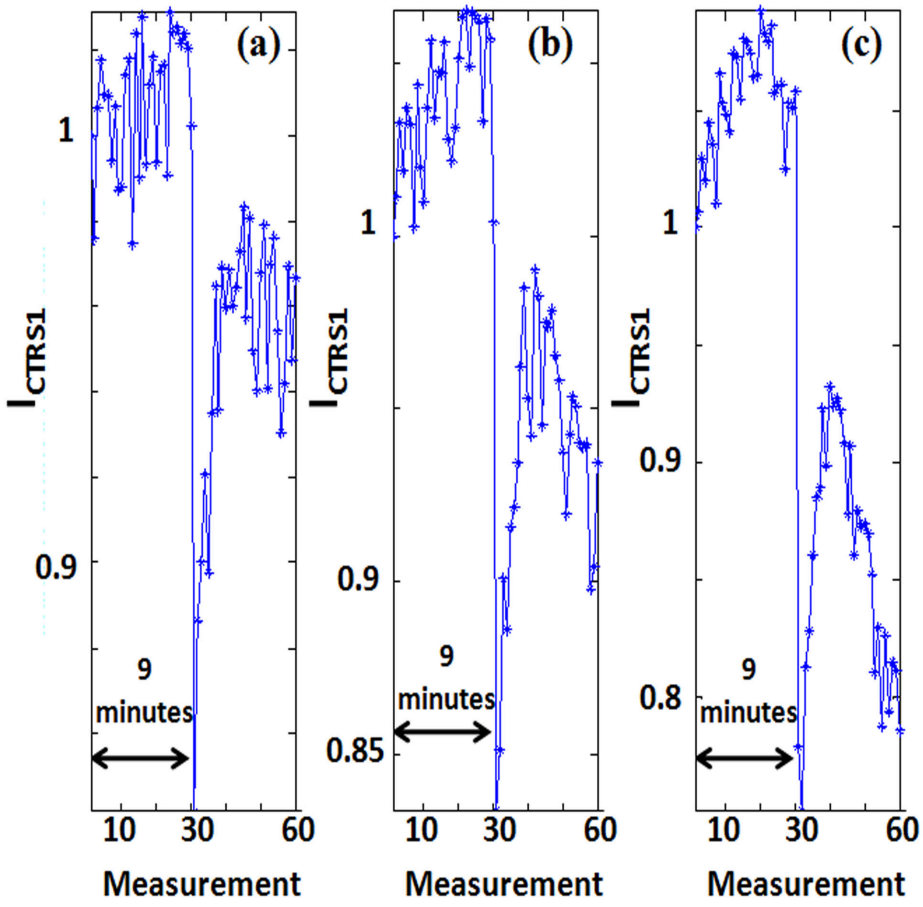

Figure 2.9: Indicator values of perturbation for CTRS1, I_{CTRS1}, vs measurement number (approximately $18s$ elapse between each measurement). Halfway in the displayed time interval, a mechanical fan is briefly activated in the stairwell perturbing the medium of wave propagation. Each of the plots correspond to cases in which the sona is exponentially amplified by different F values. In all cases, the sonas are windowed with $t_{START} = 0s$ and $t_{STOP} = 0.3s$: (a) $F = 0$, (b) $F = 1$, and (c) $F = 2$.

the medium perturbation occurred (i.e. halfway in the displayed time axis between index 30 and 31). The dynamic nature of the perturbation is exhibited in the plots because the I_{CTRS1} increases as the air currents damp out and the perturbation in the vicinity of the sensor relaxes. In Fig. 2.9(a) there is no exponential amplification, hence the dynamic perturbation is no longer sensed after about 3 minutes, which is roughly the time that it takes for the air in the vicinity of the sensor to calm down. The I_{CTRS1} indicator ends up with a smaller static value after 3 minutes in Fig. 2.9(a) in part because after the fan is activated its blades took on a different position, which by itself is a static perturbation. However, if there is exponential amplification, I_{CTRS1} changes non-monotonically as shown in Fig. 2.9(b) and (c), because the sensor is now sensitive to what happens farther out, both from the fan and the sensor. In other words, the medium of wave propagation perturbation eventually spreads out in the cavity initiating a more global perturbation. In the next sub-section, global perturbations are studied in detail.

To summarize, the general results presented in this sub-section based on the I_{CTRS1} technique are also observed in the other three techniques. It is also important to note the practical implication of these results. The medium of wave propagation can be perturbed in a variety of circumstances of interest. For instance: the dynamic nature of these perturbations means that one can verify that a cavity had been perturbed by a fast moving object even after the object has left the cavity, based solely on the air turbulence the fast moving object induced.

Sensing technique		Global perturbation		
		$F = 0$	$F = 1$	$F = 2$
CTRS1	Maximum FOM_L value	12.5	13.0	33.0
	% of FOM_L value > 2	100%	95%	90%
CTRS2	Maximum FOM_L value	15.2	12.3	23.0
	% of FOM_L value > 2	100%	95%	90%
SCC	Maximum FOM_L value	40.3	56.8	40.6
	% of FOM_L value > 2	100%	100%	100%
SMI	Maximum FOM_L value	13.8	5.1	3.1
	% of FOM_L value > 2	95%	90%	38%

Table 2.2: The maximum FOM_L over all the windowing parameter values tried is shown for each of the four sensing techniques detecting a global perturbation with a given value of the exponential amplification parameter F. In addition, the corresponding percentage of windowing parameter values which gave a FOM_L that is greater than 2 is also shown.

2.6.3 Results on Detection of Global Perturbations to the Cavity

Experimentally inducing a uniform global perturbation to a cavity is not simple. A possible global perturbation is to allow the boundaries of the stairwell and its medium to undergo thermal changes through time. If sufficient time elapses, three sides of the stairwell are exposed to the outside environment, and undergo some thermal changes that approximate global perturbations.

The procedure of the global perturbation experiment in the stairwell is very similar to the procedure of the experiments performed to detect perturbations at the six locations illustrated in Fig. 2.1. The perturbation simply involves allowing about 2 hours to elapse in between collection of baseline and perturbed sonas (time reversed pulses).

First, the same set of parameter values and techniques are used to analyze this global perturbation as in the case of the six local perturbations discussed in Sec. 2.6.1. The results are summarized in Table. 2.2. The table presents results for

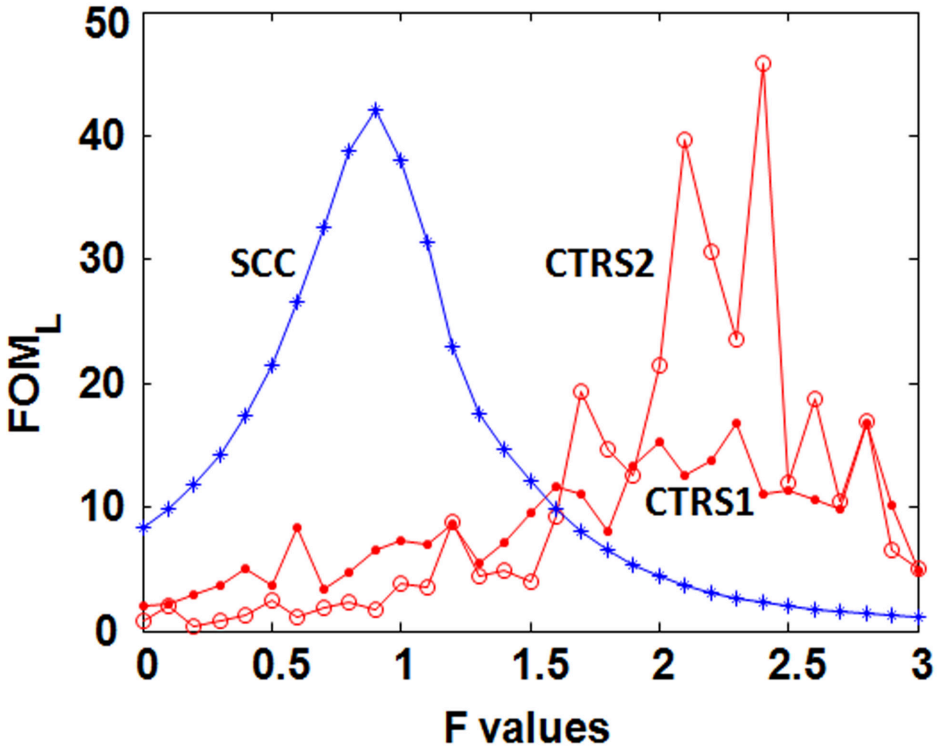

Figure 2.10: The lower bound on the FOM (FOM_L) vs the exponential amplification parameter F for detection of global perturbation using CTRS1, CTRS2, and SCC. The CTRS based techniques work best when F is close to 2, and SCC works best when F is close to 1.

each of the 3 different exponential amplification parameter F values used (0, 1, and 2) separately.

From Table. 2.2, it is seen that global perturbations can be detected by almost any of the windowing parameters tried. This supports the intuition that the effect of global perturbations leaves a signature throughout the sona signals. This raises the following question. Are global perturbations detected best when exponential amplification is applied to approximate the non-dissipative case?

If the answer is yes, then it is expected that $F = 1$ is optimum for the SCC

technique and $F = 2$ is optimum for the CTRS1 and CTRS2 techniques. This hypothesis is tested by repeating the experiment discussed above using a different set of parameter values. Here, F values ranging from 0 to 3 with increment of 0.1 are used (as opposed to using just $F = 0$, 1, and 2). On the other hand, no windowing is applied to the sona to simplify the experiment. As shown in Fig. 2.10, the FOM_L has a maximum around $F = 1$ and $F = 2$ for SCC and CTRS2 (and also CTRS1) techniques, respectively. Therefore, global perturbations are best detected by CTRS and SCC when the sona is exponentially amplified to approximate the non-dissipative case.

2.6.4 Miscellaneous Results

In this subsection, we discuss miscellaneous results that are relevant to the sensing techniques discussed so far. These results are obtained by using almost the same basic experimental set up used so far. The only difference is that the original acoustic pulse broadcast does not have a Gaussian envelope; instead, it has a rectangular envelop as can be seen in Fig. 2.13.

Particularly, the above mentioned experimental procedure to reconstruct a time reversed pulse is used to investigate the following issues [19]. The robustness of the acoustic time reversal mirror is investigated by broadcasting a time reversed sona after numerically modifying its phase information. The long term drift induced by uncontrollable environmental changes to the cavity is studied by reconstructing time reversed pulses successively over a long time period using a single sona signal

recorded at an earlier time(this is similar to the studies on the global perturbations discussed in Sec. 2.6.3). Finally, the feasibility of detecting changes to the configuration of objects inside a cavity is demonstrated as follows. A time reversed pulse is reconstructed in a stairwell with a given configuration of objects, then the same sona signal is used to reconstruct a time reversed pulse after we rotate a rectangular box to a new orientation in the stairwell. The time reversed pulses reconstructed before and after the perturbation to the cavity are compared with a goal of detecting the perturbation.

2.6.4.1 Effect of Phase Noise Added to the Sona

The robustness of the time reversal mirror to phase noise/manipulation that corrupts the sona signal is studied. We performed an experiment in which the digitized sona signal is numerically modified before it is time reversed and broadcasted back into the cavity it was collected from. Specifically, the sona is Fourier transformed to get its magnitude and phase information in the frequency domain (with a frequency step of $2Hz$ between data points). Gaussian distributed random numbers with zero mean and a given standard deviation, which is systematically varied from 0 to π, are added to the phase of the Fourier transform of the sona. The unaltered magnitude information, and the modified phase information are used to generate a modified sona signal using inverse Fourier transform. This modified sona is then time reversed and broadcasted into the cavity, and the peak to peak amplitude of the reconstructed pulse is measured.

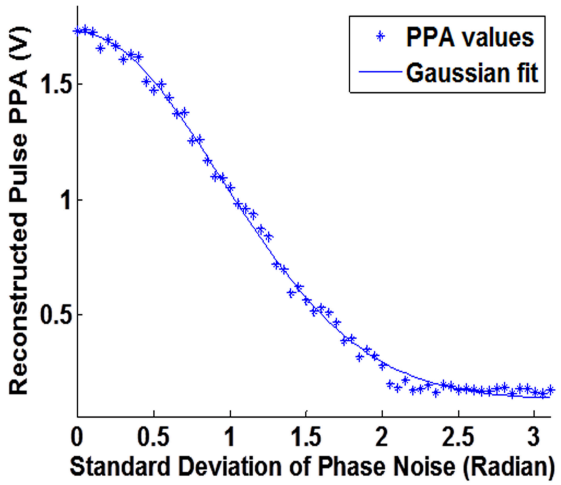

Figure 2.11: A plot of peak-to-peak amplitude (PPA) of the reconstructed pulse amplitude in volts versus the standard deviation of the Gaussian phase noise distribution in radians. Gaussian distributed random numbers with zero mean and a standard deviation, which is systematically varied between 0 and π, are added to the phase of the Fourier transform of the sona signal. This effectively scales the reconstructed pulse by a Gaussian function of the standard deviation of the underlying phase noise.

The peak to peak amplitude of the reconstructed pulse is observed to diminish as the standard deviation of the phase noise is increased (see Fig. 2.11). This result is also seen using a theoretical model that applies similar phase noise to the sona signal.

Because the system is linear, the effect of phase noise on the sona can be directly calculated. The sona can be expressed as a Fourier transform as $S(t) = \int d\omega S(\omega) \exp(i\omega t)$. With added phase noise, distributed as $P_{\Delta\theta}(\theta) = \frac{1}{\sqrt{2\pi(\Delta\theta)^2}} \exp \frac{-\theta^2}{2(\Delta\theta)^2}$, the modified sona becomes $S_{noisy}(t) = \int d\omega \tilde{S}(\omega) \int d\theta \exp i\omega t \exp i\theta P(\theta)$. Carrying out the integral over the random variable leads to $S_{noisy}(t) = \int d\omega \tilde{S}(\omega) \exp i\omega t \exp \frac{-(\Delta\theta)^2}{2}$. Clearly the sona signal is reduced in magnitude by an amount that depends on the width of the Gaussian distribution $\Delta\theta$.

The degradation of the sona signal translates into degradation of the reconstructed pulse, as shown in Fig. 2.11. The peak-to-peak amplitude of the reconstructed pulse versus width of the Gaussian phase noise distribution is fit to a Gaussian function as $V_{p-p}(\Delta\theta) = V_0 + A \exp \frac{-B(\Delta\theta)^2}{2}$, and the three parameters V_0, A, and B are allowed to vary. The result shows an excellent fit with $V0 = 0.14V$, $A = 1.58V$, and $B = 1.14$. The value of B is very close to the expected value of 1, while the offset value V_0 is the background level in the extremely noisy limit.

2.6.4.2 Long-Term Drift of the Reconstructed Pulse

As the time reversed sona signal is periodically broadcast into the cavity, the reconstructed time reversed pulse consistently reproduces itself up to some sta-

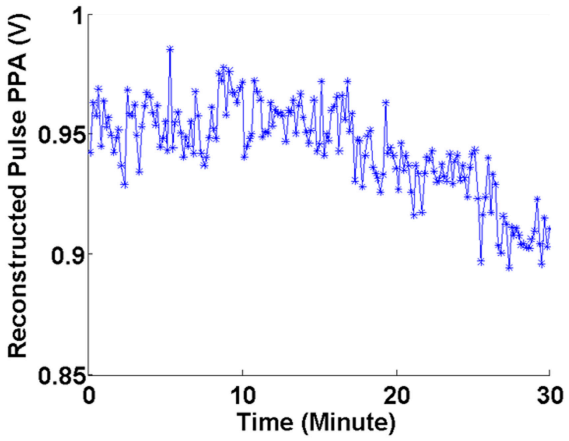

Figure 2.12: Long term drift in the PPA in volts of the reconstructed time reversed pulse in the stairwell. The PPA exhibits a drift as the reverberant cavity and air medium go through thermally-induced changes in time.

tistical measurement fluctuation. Particularly, we look at the fluctuations in the peak-to-peak amplitude of the reconstructed pulse as a single time reversed sona is periodically broadcasted into a nominally unperturbed cavity every $10s$ over a time period of $20min$ (see Fig. 2.12). For short time periods, the statistical variation of the peak-to-peak amplitude is about $\pm 2\%$. However, there are uncontrollable changes to the cavity over long time periods, such as thermal expansion or perhaps changes in temperature of the air, and these play a role in the drift of the reconstructed time reversed pulse amplitude on longer time scales ($> 10min$).

2.6.4.3 Effect of a Volume-Preserving Perturbation

Finally, we test the feasibility of the acoustic time reversal mirror to detect volume preserving perturbations to the cavity by comparing reconstructed pulses

before and after a specific perturbation of the scattering environment. The perturbation we perform involves rotating a rectangular cardboard box (with a volume of $30x60x80cm^3$), located inside the stairwell, by 90 degrees. The reconstructed time-reversed pulses before and after perturbation are compared in one of the following ways: (1) the peak-to-peak amplitude of the two pulses are compared, or (2) the normalized cross correlation between the two reconstructed pulses is calculated. The peak-to-peak amplitude of the reconstructed pulse drops from $1.11V$ to $0.92V$ upon the perturbation; this is a reduction by 17% (see Fig. 2.13), which is significant compared to the typical statistical fluctuation of about $\pm 2\%$ between nominally identical reconstructed pulses (Fig. 2.12). On the other hand, the normalized cross correlation of the pulses before and after perturbation is 93%. From this and many other measurements [18, 20] it is clear that monitoring the decrease in the peak-to-peak amplitude of the reconstructed time-reversed pulse is not only computationally simpler but it is also a statistically more reliable mechanism to detect perturbations.

2.7 Discussion

The results summarized in Table 2.1 indicate that SCC, CTRS1 and CTRS2 perform reliably in detecting perturbations at different ranges. The SMI performs detection as well, despite its relative weakness. The SCC has the highest FOM_L across the board, which is its main advantage. However, the SCC also has the broadest optimal parameter space, which may be a disadvantage if one is interested in

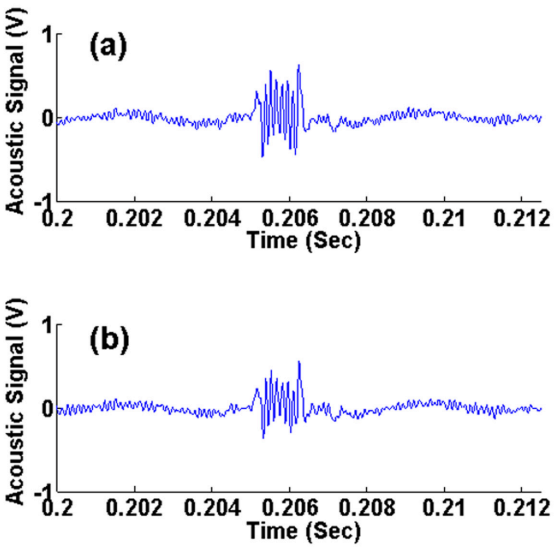

Figure 2.13: The effect of a volume preserving perturbation on the reconstructed time reversed (TR) pulse. The TR pulses (a) before ($PPA = 1.11V$) and (b) after ($PPA = 0.92V$) perturbation have a normalized correlation of 93%, but the PPA drops by 17%. The perturbation is done by rotating a rectangular box ($30cmx60cmx80cm$) by ninety degrees inside the reverberant cavity (stairwell).

associating a given perturbation location with a narrow distinct optimal parameter space; such an association can be useful to localize the perturbation.

Another shortcoming of the SCC, and also the SMI, is their higher computational cost. The lower bound on the computational resources needed to compare two sona signals using the SCC or SMI roughly scales with the length of the sona signals. [See Eq. 2.1 to Eq. 2.4] Besides, it is important to note that we have implemented the SMI by calculating the mutual information with the so called "equidistant binning estimator" technique which is the simplest method computationally [57]; if the SMI were to be implemented using other more complicated "mutual information estimators", its higher computational cost would overshadow any other benefits. This computational problem inherent in the SCC and SMI methods can be mitigated only by considering narrow windows of the sona signals. In contrast, the CTRS based sensing techniques have a small fixed computational cost in comparing the time reversed pulses regardless of the values of the parameters used to process the sona. Particularly, CTRS1 is the most computationally efficient sensing technique as it relies on a simple peak to peak amplitude measurement of the reconstructed time reversed pulses. However, the CTRS requires analogizing and broadcasting a time reversed sona signal.

It is worth emphasizing that the SCC technique is motivated by the Scattering Fidelity [15, 51, 52, 53, 54]. As mentioned in Sec. 2.4.1, the SCC technique implicitly calculates the Scattering Fidelity for the case of no exponential amplification (i.e. $F = 0$) as long as a set of t_{START} and t_{STOP} windowing parameters are used which effectively result in the sliding of a narrow rectangular-time-window

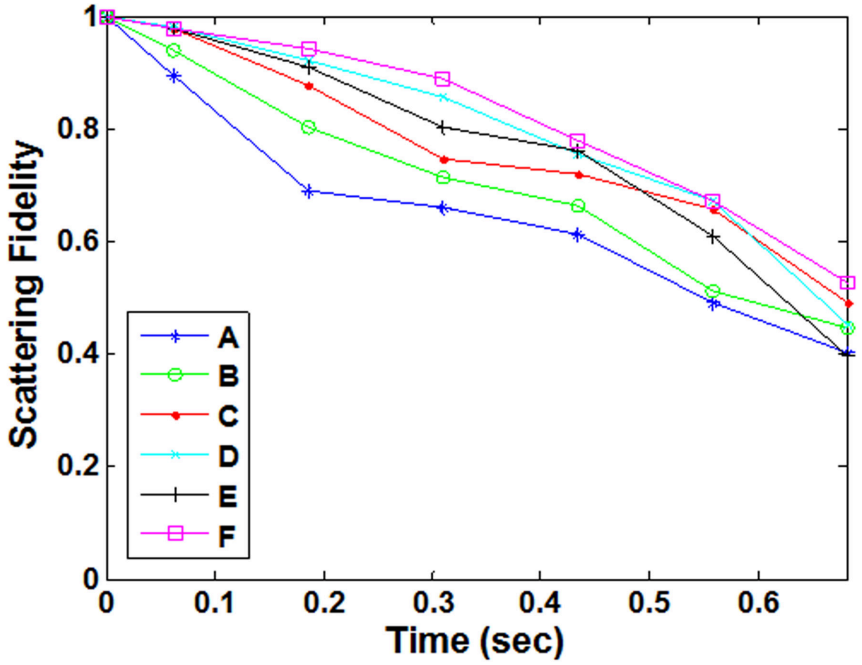

Figure 2.14: SF of sonas before and after a perturbation as a function of time. The SF plotted here is averaged over 25 realizations. The width of the time window over which the I_{SCC} and hence the SF is computed is $0.1s$. The six SF curves are labeled A through F; the labels correspond to the locations of the perturbations illustrated in Fig. 1. For example, the slowest decaying SF curve comes from sonas measured before and after perturbing the cavity at location F in Fig. 1. The rates of fidelity decay are generally indicative of the relative distance of the perturbations from the sensor.

across the baseline and perturbed sona signals being compared. Fig. 2.14 shows the 25-realization-averaged Scattering Fidelity versus time measured for the six local perturbations illustrated in Fig. 2.1. The Scattering Fidelity (SF) is simply calculated using Eq. 2.1 and Eq. 2.2 as follows: $SF(t*) = I_{SCC}(t*)$, where $t*$ is the middle of the time-window formed by the parameters t_{START} and t_{STOP}, and where $F = 0$.

It is clear that the Scattering Fidelity decays the fastest for short-range perturbations (i.e. perturbation locations A and B in Fig. 2.1), whereas the slowest Scattering Fidelity decay is for the long-range and concealed perturbation (i.e. perturbation location F). When the Scattering Fidelity decay of concealed and non-concealed perturbations that are at about the same distance from the sensor is compared, it turns out that non-concealed perturbations (i.e. A, C, and E) result in a faster Scattering Fidelity decay. These results agree with our earlier observations regarding the dependence of the optimum parameter space (in the "t_{START}, t_{STOP} contour plane" of the FOM_L) on the perturbation location; (i.e. long range and concealed perturbations are detected better if we look at the end of the sona.)

The exact mathematical equivalence between the quantum mechanical quantities Loschmidt echo and quantum fidelity is not quite replicated in their classical analogs developed here, namely the I_{CTRS2} and I_{SCC}. It is important to note that the overlap between the classical wave systems is done only at a single point in space where the microphone is located; in addition, there is dissipation in the classical system.

2.8 Conclusion

The direct analogy of the quantum mechanical concepts of Loschmidt echo and quantum fidelity give rise to the sensing techniques CTRS2 and SCC presented here. In addition, the CTRS1 and the SMI techniques are developed in parallel. The CTRS based techniques, which rely on a time reversal mirror, offer a computationally cheap alternative to the SCC and SMI techniques that are based on a more traditional "propagation comparison" concept.

A systematic set of experiments are done to detect perturbations at six different locations in an enclosed stairwell using these sensing techniques. The processing of the sona signals by exponential amplification and time windowing allowed long range detection at concealed locations in the cavity; such detection endeavors would not have been possible without such processing of the sona, especially the time windowing. The optimal parameter space of the sensing techniques is also seen to be related to the perturbation location. Even though there may not be a one to one correspondence between an optimal parameter space and a perturbation location (which would enable exact localization of the perturbation), the current results indicate that one can at least rule out candidate locations for a detected perturbation by looking at the optimal parameter space found.

In addition to detection of static boundary perturbations at given locations, perturbations to the medium of wave propagation are also shown to be detectable. Detection of such perturbations opens up a wide range of applications. It is also shown that by using exponential amplification of the sona, one can see how the

initially localized medium perturbation spreads out into other parts of the cavity. The extreme case of global perturbations, which can be experimentally realized by allowing the cavity to undergo thermally induced changes, is also investigated. It is shown that the global perturbations are detected best when the sona is exponentially amplified to approximate the lossless case.

Chapter 3

Quantifying Volume Changing and Shape Preserving Perturbations

In this Chapter, the sensors introduced in Chapter 2 are used to quantitatively measure perturbations that change the volume of a wave chaotic cavity while leaving its shape intact. The sensors work in the time domain by using either scattering fidelity of the transmitted signals or the Loschmidt echo. The sensors were tested experimentally by inducing volume changing perturbations to a one cubic meter pseudo-integrable, real-world cavity. Perturbations which caused a volume change that is as small as 4 parts in 10^5 were quantitatively measured. These results were obtained by using electromagnetic waves with a wavelength of about $5cm$, therefore, the sensor is sensitive to extreme sub-wavelength changes of the boundaries of a cavity. The experimental results were compared with Finite Difference Time Domain (FDTD) simulation results, and good agreement was found [1]. Furthermore, the sensor was tested using a frequency domain approach on a numerical model of the star graph, which is a representative wave chaotic system. These results open up interesting applications such as: monitoring the spatial uniformity of the temperature of a homogeneous cavity during heating up / cooling down procedures, verifying the uniform displacement of a fluid inside a wave chaotic cavity by another fluid, etc.

[1]The simulation in Sec. 3.3.2 was carried out by Professor Franco Moglie at the "Dipartimento di Ingegneria dell'Informazione" in the "Universita Politecnica delle Marche" in Ancona, Italy

3.1 Introduction

Most sensors such as SONAR rely on direct line of sight information. In that case, monitoring a cavity which has an irregular geometric shape, including hidden regions, may require installing multiple sensors throughout the cavity for a comprehensive coverage. However, most real world cavities have irregular shapes. This irregularity has the benefit of facilitating the creation of ray chaotic trajectories. The study of waves propagating inside these ray chaotic cavities, in the semi-classical limit, is called wave chaos [2]. Wave chaos is essentially the manifestation of the underlying ray chaos on the properties of the waves whose wavelength is much smaller than the typical dimensions of the cavity. Ray chaos is characterized by sensitive dependence of ray trajectories to initial conditions. The effect of perturbations on waves propagating in such cavities was studied using the concept of the scattering fidelity for some specific experimental set ups [15, 53]. Scattering fidelity is a normalized correlation between two cavity response signals as a function of time; the response signals are typically collected before and after a perturbation to the cavity. However, the practical sensing application of the scattering fidelity concept had not been explored. In Chapter 2, wave chaotic sensing techniques that allow a comprehensive spatial coverage using a single sensor were introduced [18, 20, 19]. These techniques rely on the wave chaotic nature of most real world cavities. When a pulse is broadcast into a cavity to probe it, the response signal consists of reflections that bounced from almost all parts of the cavity; this is due to the underlying spatial ergodicity of ray trajectories in ray chaotic cavities. Therefore, the response signal

essentially "fingerprints" the cavity, and it enables the detection of changes to the cavity.

The wave chaotic sensing techniques in Chapter 2 were not used to quantify any kind of perturbation [18, 20, 19]. Local and global perturbations to the boundaries of the cavity, and perturbations to the medium of wave propagation within the cavity, were all shown to be detectable [20]. However, the quantification of a perturbation was not accomplished. On the other hand, a remarkably sensitive quantification of a perturbation which involved translation of a sub-wavelength object over sub-wavelength distances was successfully demonstrated [58]. However, the quantification was based on an empirical law that is specific to the system and perturbation at hand. This is because the effect of the perturbation on the dynamics of the waves propagating inside the wave chaotic cavity is not straightforward [58]. In this Chapter, we focus on a single class of perturbation whose effect can be theoretically predicted, and propose two time domain techniques to measure that particular kind of perturbation in any cavity.

In this chapter, we focus on quantifying volume changing perturbations (VCP) to a wave chaotic scattering system. A VCP changes the volume of a cavity, but it may slightly change its shape as well. A special kind of VCP is a volume changing and shape preserving perturbation (VCSPP). In Sec. 3.2, the theoretical prediction of the effect of VCSPPs is discussed. Sec. 3.2 proposes two time domain techniques to quantify VCPs. As Chapter 2, these techniques are based on the scattering fidelity and the Loschmidt echo. Sec. 3.3 presents the experimental test of these two VCSPP sensing techniques, along with a head-to-head numerical validation.

The experimental test is carried out inside a pseudo-integrable, real world cavity using electromagnetic waves. Sec. 3.4.2 provides a test of the sensing techniques in a numerical model of the star graph, which is a quasi-1D wave chaotic system. Sec. 3.4.2 also shows the relative merits of approaching the problem in the frequency domain. Sec. 3.5 discusses practical applications of the VCSPP sensor, and Sec. 3.6 provides a conclusion.

3.2 Theory and Approach

Consider a generic wave chaotic cavity with volume V_1, which is considered as a baseline system (see Fig. 3.1(a)). The schematics in Fig. 3.1(a)&(b) illustrate the cavity as a stadium billiard, but the cavity is considered generic throughout Sec. 3.2. Suppose that the baseline cavity is perturbed such that each of its three length dimensions increase by a factor of P. This amounts to a VCSPP, by a factor of P^3; the perturbed cavity has a volume of $V_2 = P^3 V_1$ (see Fig. 3.1(b)). Fig. 3.1(a)&(b) show a brief pulse being broadcast into the cavity. The response signal to the pulse is called the sona. The sona from the baseline cavity (which is referred to as baseline sona) and the sona from the perturbed cavity (which is referred to as perturbed sona) are expected to be related, under certain conditions which are discussed later in this section. For instance, if $P > 1$, a signal feature in the perturbed sona is expected to be delayed by a factor of P compared to its appearance in the baseline sona. The sensor is designed to enable the measurement of the value of P, which effectively quantifies the VCSPP, by using the theoretically

predicted effects of the VCSPP on the dynamics of the waves. Another practically useful capability of the sensor is to check if the perturbation is indeed a VCSPP, and not just merely a VCP.

As opposed to the resource intensive frequency domain sensing, it is practically preferable to use a time domain interrogation of the baseline and the perturbed cavity by measuring the sonas. However, it is useful to look at the problem in the frequency domain to understand the limitations of the time domain approach. Consider the scattering parameters of the cavities as a function of frequency. The $|S_{12}|^2$ as a function of frequency of the baseline and the perturbed 2-port cavity are schematically shown in Figs. 3.1(c)&(d). We expect a precise mathematical relationship between the scattering parameters of the baseline and perturbed cavities as a function of frequency. Particularly, if $P > 1$, the baseline spectrum can be obtained by stretching out the perturbed spectrum by a factor of P along its frequency axis. This is precisely the prediction about the effect of VCSPPs on the dynamics of the waves.

Now, we can describe the time domain approach further, and point out its limitations. When a cavity is monitored for a VCSPP, a pulse is periodically broadcast into it, and a sona is collected. It is generally preferred to use the same probing pulse (i.e. the same center frequency, bandwidth, amplitude, and shape) so that only the changes in the system show up when looking at the sonas. When a VCSPP (with $P > 1$) occurs, the transmission spectrum $|S_{12}|^2$ of the system shrinks along the frequency axis by a factor of P as shown in Figs. 3.1(c)&(d). The probing pulse frequency coverage is schematically shown in the frequency domain in

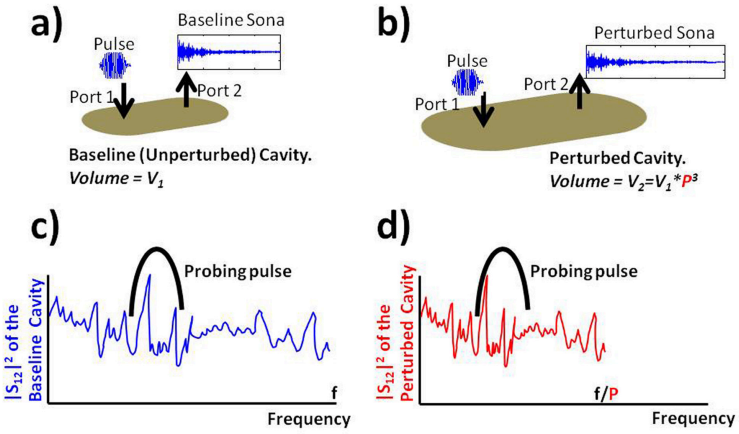

Figure 3.1: Schematic illustrating Volume Changing & Shape Preserving (VCSP) perturbations. (a) Sona is collected from a baseline cavity of volume V_1. (b) Sona is collected from a perturbed cavity of volume V_2. (c) Pulse exciting the resonances of the baseline system. (d) The same pulse exciting the perturbed resonances of the perturbed system.

Figs. 3.1(c)&(d). The baseline and the perturbed sonas are a result of the probing pulse exciting resonances of the cavity. The resonances excited by the probing pulse in the baseline and perturbed cavity are not all the same. Suppose that there is a significant overlap between the resonances excited by the probing pulse in the baseline and perturbed cavity. Under this condition, we expect that the baseline sona can be numerically stretched out by a factor of P along its time axis to approximate the perturbed sona.

As in Chapter 2 [20], there are two classes of time domain sensing techniques that can be used to quantify VCSPPs. The first technique relies on the scattering fidelity [14]. Consider two sonas X and Y, which are real voltage versus time signals.

The scattering fidelity (SF) of X and Y is simply their normalized correlation as a function of time, t [14];

$$SF(t) = \frac{\sum_{m=t}^{m=t+\Delta t} X[m]Y[m]}{\sqrt{\sum_{m=t}^{m=t+\Delta t} X[m]^2 \sum_{m=t}^{m=t+\Delta t} Y[m]^2}} \tag{3.1}$$

where Δt in Eq. 3.1 is typically chosen to be the time scale it takes the waves to traverse the cavity, at the very least, once (i.e. in order of magnitude of the ballistic flight time). The $SF(t)$ of two sonas can take real values ranging from 1 (i.e. perfect correlation at time t) to -1 (i.e. perfect anti-correlation at time t). If $SF(t)$ is 0, then the sonas are not correlated at time t. The SF of the baseline and the perturbed sonas is not expected to stay close to 1 throughout time. However, the SF of the perturbed sona and the baseline sona whose time axis is scaled using the optimum stretching/squeezing factor is expected to stay close to 1 throughout time. The optimum stretching/squeezing factor is expected to approximate P, which is also related to the magnitude of the perturbation.

The second technique to quantify VCSPPs utilizes the Loschmidt echo through classical time reversal mirrors [21]. To see the operation of a time reversal mirror, consider a two port cavity. Suppose that a pulse is broadcast into the baseline cavity through port 1, and a baseline sona is recorded through port 2. If the baseline sona is time reversed and broadcast back into the cavity through port 2, a time-reversed version of the original pulse reconstructs at port 1. The reconstructed pulse approximates the time reversed version of the original pulse broadcast into the cavity. However, if the time reversed baseline sona is broadcast into a perturbed cavity, then the reconstructed pulse will more poorly approximate the time reversed version of

the original pulse. The time axis of the baseline sona needs to be scaled using the optimum factor before it is time reversed and broadcast into the perturbed cavity; this is assuming that the perturbation is VCSPP. The optimum stretching/squeezing factor is expected to result in a reconstructed pulse that best approximates the original pulse. Once again, the optimum stretching/squeezing factor is expected to be P.

3.3 Testing the Quantitative Sensor in the Time Domain

3.3.1 Experimental Setup

The cavity that is used to test the sensing techniques is an approximately $1m^3$ (i.e. dimensions of $1.27m$ x $1.27m$ x $0.65m$) aluminum box that has scatterers and interior surface irregularities which facilitate the creation of ray chaotic trajectories. The cavity is pseudo-integrable because it has parallel walls which may support integrable modes in addition to the chaotic modes. Overall, the cavity represents a real world case in which the sensor would operate. There are two ports that connect the cavity to a microwave source and an oscilloscope. Each port consists of a monopole antenna of length $\approx 1cm$, and diameter $\approx 1mm$. The monopole antennas are mounted on the wall of the cavity. An electromagnetic pulse with a center frequency of $7GHz$, and a Gaussian envelope of standard deviation $1ns$ is typically broadcast into the cavity through port 1. The resulting sona signal is collected at port 2 by the oscilloscope, and it is digitally filtered to minimize noise.

Experimentally inducing a VCSPP can be more challenging than inducing

a VCP, which may slightly change the shape of the enclosure. VCSPPs can be realized by changing the speed of wave propagation within the cavity (i.e. changing the electrical volume). The speed of light (for the electromagnetic experiment at $7GHz$) within the cavity can be changed by filling up the cavity with different gasses which have similar dissipation and dispersion properties. For example, the relative dielectric constant (ϵ_r) of air (at $\approx 50\%$ relative humidity), nitrogen gas, and helium gas are $\epsilon_{r,air} = 1.000576$, $\epsilon_{r,N_2} = 1.000547$, $\epsilon_{r,He} = 1.00017$, respectively, at a temperature of 20^0C. As discussed later in Sec. 3.3.2, it was shown that the slightly different dissipation values of these gasses does not change the sona signal in any perceivable way. However, the slightly different speed of light values of these gasses was seen to significantly change the sonas collected.

The experimental procedure for filling up the cavity with different gasses is as follows (see Fig. 3.2). There is a gas inlet on the top wall of the cavity. The gas inlet was connected to a gas tank via a plastic tube and a long copper tube coil. The long copper tube coil allowed the gas to reach room temperature before it gets into the cavity. There was a pressure regulator in between the gas tank and the copper tube to control the rate of flow of the gas. There were three gas outlets near the top wall of the cavity, and three gas outlets near the bottom wall of the cavity. The diameter of the gas inlet and outlets was just about a fifth of the wavelength, so that no significant microwave leakage occurred. Depending on the density of the gas which was being pumped into the cavity, half of the outlets (near the top or bottom wall) were closed off with tape. This procedure helped to displace the existing gas and retain the gas being pumped into the cavity.

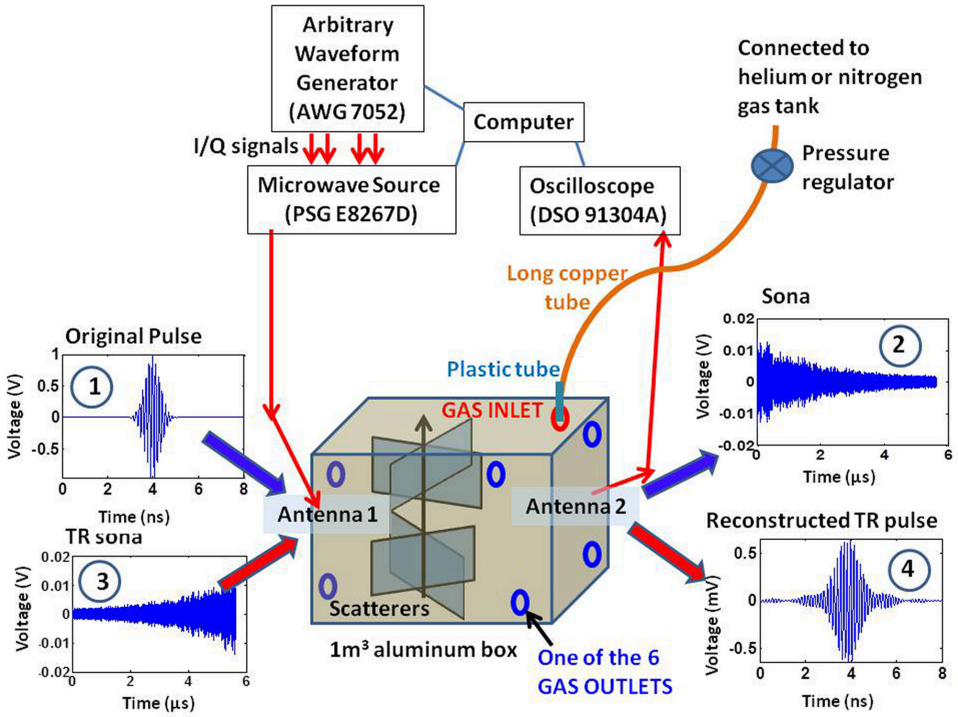

Figure 3.2: Schematic of the experimental set up to induce VCSPPs in an electromagnetic cavity, and the equipment needed to implement an electromagnetic time reversal mirror. The VCSPP is induced by filling the cavity with helium or nitrogen gas. The gas transfer is carried out using a long copper tube that helps to warm the gases up to room temperature. There is a gas inlet, and six gas outlets on the walls of the cavity. The cavity has two antennas that are connected to a microwave source and an oscilloscope. The electromagnetic time reversal is carried out as follows. First, the original pulse is broadcast through antenna 1 (1), and the resulting sona is collected at antenna 2 (2). Next, the time reversed sona is injected into the system at antenna 1 (3) to retrieve the reconstructed time reversed pulse at antenna 2 using spatial reciprocity (4). Experimental data are shown for each step.

As detailed in Sec. 3.3.4, sona signals were collected from the cavity both during and after the gas transfer process. The sona signals that were collected during the gas transfer indicate when the cavity is fully filled with the new gas. The sona signals that were collected after the gas transfer were used to measure the VCSPP that was induced.

3.3.2 Finite Difference Time Domain (FDTD) Simulations

The experiment described in Sec. 3.3.1 was modeled by a Finite Difference Time Domain (FDTD) code [2]. The FDTD code solves Maxwell's Equations inside a 3D numerical model of the $1m^3$ cavity. The code for this simulation was optimized for parallel computers and for the simulation of reverberation chambers [59, 60]. The FDTD simulation of the cavity enabled a direct comparison of experimental and simulation results.

The FDTD simulation formed a 3D model of the experimental cavity by using spatial cubic cells with an edge length of $\Delta x \approx 3.49mm$, and the cavity consisted of $364*364*188$ cells. The smallest time step taken to propagate solutions of Maxwell's Equations through the cells was $\Delta t = 6ps$. Therefore, the Courant's number for computational stability was $\frac{c\Delta t\sqrt{3}}{\sqrt{\epsilon_r}\Delta x} \approx 0.89 < 1$ for all the media (ϵ_r) considered, where c is the speed of light in vacuum [61]. The model of the cavity also had two ports, with antennas that have similar characteristics to the ones used in the experiment. The electromagnetic pulse broadcast into the model was also similar

[2]The simulation in Sec. 3.3.2 was carried out by Professor Franco Moglie at the "Dipartimento di Ingegneria dell'Informazione" in the "Universita Politecnica delle Marche" in Ancona, Italy

to the one broadcast experimentally (i.e. center frequency of $7GHz$, and width of $1ns$). The maximum and minimum of the ratio of the wavelength to the cubic cell dimension were 14 and 11 respectively.

In the experiment, the main source of dissipation is ohmic loss from the aluminum walls of the cavity. In the simulation, the walls were assumed to be lossless for simplicity. Instead, an equivalent loss was introduced within the medium of wave propagation to achieve the same quality factor as the experimental cavity [59]. To accomplish this, a uniform conductivity of $10^{-5}S$ was introduced throughout the interior of the cavity model.

As mentioned in Sec. 3.3.1, the experiment relies on changing the electrical volume (at $7GHz$) within the cavity by changing the gasses filling the cavity. The gasses used were air, nitrogen gas, and helium gas. For typical laboratory atmospheric conditions, the electromagnetic loss in air at $7GHz$ can be mainly attributed to oxygen molecules [62, 59]. The specific attenuation of oxygen is $0.007dB/km$ whereas the specific attenuation of water vapor is just $0.003dB/km$ at $7GHz$. The conductivity of air is estimated to be $4.3 * 10^{-9}S$ [59]. Therefore, the dissipation inside the cavity filled by helium gas or nitrogen gas was roughly modeled by introducing an equivalent loss of $10^{-5}S - 4.3 * 10^{-9}S = 9.9957 * 10^{-6}S$ uniformly throughout the cavity (once again, the walls were assumed to be lossless in the model). It was shown that sonas that are collected from the cavity model with $10^{-5}S$ conductivity, and sonas that are collected from the cavity model with $9.9957 * 10^{-6}S$ are almost exactly identical. This simulation result proved that the difference in loss among air (at $\approx 50\%$ relative humidity), nitrogen gas, and helium gas is not significant.

3.3.3 Sensitivity of the Quantitative Sensor

It was shown that the minute conductivity differences (i.e. 0.05%) among air, nitrogen gas, and helium gas do not affect the nature of the sonas collected from the cavity filled by any of these gasses. However, it was also shown that the minute differences in ϵ_r (at $7GHz$) of these gasses (which is also 0.05%) do affect the sonas. This will be shown by first deriving an expression for the minimum volume changing perturbation that can be measured. Then, it will be shown that the VCSPP which is induced when either of these three gasses is displaced by another one, can be measured using our experimental set up.

Consider using the sensing technique based on scattering fidelity, which was introduced in Section 3.2. The technique relies on comparing the baseline and perturbed sonas as a function of time. In Sec. 3.3.3, it is assumed that the perturbation increases the volume by a factor of P^3, where $P > 1$. At time $t = 0$, the sonas are expected to be similar for small enough Δt (see Eq. 3.1), hence $SF(t = 0) \approx 1$. At any other time t, there may be a perceptible difference between the sonas. Any particular signal feature in the baseline sona at time t is expected to be seen in the perturbed sona at time $t + t_{gap}(t)$, where $t_{gap}(t) = P * t - t$; here, $t_{gap}(t)$ is defined as the time gap that develops between two identical features in the baseline and perturbed sona at time t, where t is measured within the baseline sona. This is because the baseline sona stretched out along its time axis by a factor of P should approximate the perturbed sona, as discussed in Sec. 3.2.

The minimum volume changing perturbation that can be quantified is the

minimum of $P^3 = (\frac{t+t_{gap}(t)}{t})^3$. On the other hand, when the SF of the baseline and perturbed sona is computed at any time t (see Eq. 3.1), there are two necessary conditions that should be satisfied in order to be able to measure the perturbation. First, the signal-to-noise-ratio (SNR) of the baseline sona at time t should be well above 1. This is because the SF of the baseline and perturbed sonas (when the SNR is close to 1) would simply be the correlation of two noisy signals. Second, $t_{gap}(t)$ should be, conservatively, greater than half of the period of the oscillations in the sona signals. Otherwise, if $t_{gap}(t)$ is much smaller than half a period of the sona oscillations, the $SF(t)$ will not be convincingly lower than its maximum value at $t = 0$ (which is ≈ 1 for the appropriate Δt value in Eq. 3.1), hindering reliable measurement of the perturbation. These two conditions guarantee that the $SF(t)$ of the baseline and perturbed sona can be used to measure the perturbation. The minimum of $P^3 = (\frac{t+t_{gap}(t)}{t})^3$ subject to these two conditions is $(1 + \frac{T/2}{T_{NoiseLevel}})^3$, where T is the period of sona oscillations and $T_{NoiseLevel}$ is the time at which the SNR of the sona approaches 1.

Therefore, the minimum perturbation that can be quantified by the sensor (i.e. $(1+\frac{T/2}{T_{NoiseLevel}})^3$) depends on the wavelength of the waves used to probe the cavity, the dissipation in the cavity and the SNR of the system. The SNR in turn depends on the noise in the system, and the dynamic range of the wave generation and detection equipment. The equipments used in this experiment are shown in Fig. 3.2. For the electromagnetic experimental set up that is probing the $1m^3$ cavity discussed in this work, using a $5cm$ wavelength waves, a VCSPP that is as small as 4 parts in 10^5 can be measured.

Getting back to the experimental set up shown in Fig. 3.2, the VCSPP was induced by changing the gas filling the cavity from air to nitrogen gas or to helium gas. This results in $\approx 0.05\%$ change in the ϵ_r of the gasses, which is equivalent to a VCSPP of 5 parts in 10^5. Therefore, the experimental system is expected to detect the change in electrical volume induced when one of these gasses displaces the other inside the cavity.

3.3.4 Results from the Experiment and the FDTD Simulation

3.3.4.1 Sensing Using Scattering Fidelity

The air in the cavity at $\approx 20^0C$ and $\approx 50\%$ relative humidity, was systematically displaced with nitrogen gas at room temperature. The nitrogen gas was pumped into the cavity at $30psi$ gauge pressure as the air flowed out through the gas outlets of the cavity. Every two minutes, the flow was stopped, and 10 nominally identical sonas (which are actually almost identical) were measured from the cavity, and these were averaged together. The averaging is done after aligning the sonas to eliminate the adverse effects of trigger jitter in the data acquisition system. In this manner, five averaged sonas were collected from the cavity as the cavity was filled with more and more pure nitrogen gas. Each of these five sonas were compared with a sona that was collected from the original cavity filled with air. The comparison was done by computing the scattering fidelity (see Eq. 3.1) of the sona from airy cavity and a sona from a partially air-filled cavity. Fig. 3.3 shows these scattering fidelities. The concentration of nitrogen increases with the number of minutes

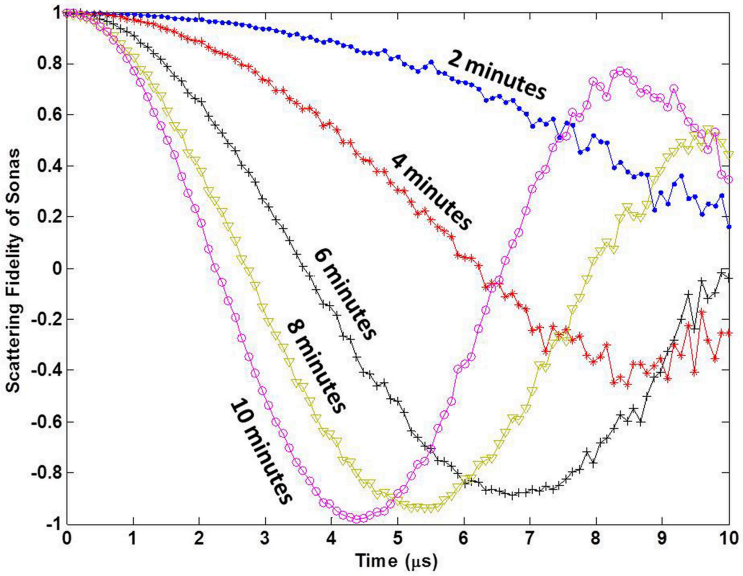

Figure 3.3: Scattering fidelity of sona signal from a cavity that is filled with air (baseline), and sona from a perturbed cavity that had 2, 4, 6, 8, and 10 minutes of nitrogen gas inflow. The perturbation gets stronger as the concentration of nitrogen gas increases in the perturbed cavity.

of nitrogen inflow into the cavity. Therefore, Fig. 3.3 shows scattering fidelities of VCSPPs which get progressively stronger.

The scattering fidelity of a VCSPP shows oscillation whose period is inversely related to the strength of the perturbation (see Fig. 3.3). The oscillation in the scattering fidelity can be explained by specifically examining the scattering fidelity of sona from the air filled cavity, and sona from the nitrogen gas filled cavity (see Fig. 3.4(a)). Here, both of the sonas were obtained by averaging over 100 nominally identical sona samples. For times relatively close to $t = 0$, the difference in the speed of light between air and nitrogen does not show up when signals that traveled through these two gasses are compared (see Fig. 3.4(b)). However, at $t \approx 4\mu s$, a phase shift of half a period (i.e. $0.07ns$ for the probing pulse centered at $7GHz$)

develops between the two signals (see Fig. 3.4(c)). Thus, the scattering fidelity between the two sonas becomes ≈ -1. The relative phase shift between the two sonas increases to one full period at about $8\mu s$, and hence the scattering fidelity recovers to almost 1 (see Fig. 3.4(d)). However, as can be seen in Fig. 3.4(d), in addition to the phase shift that develops between the individual oscillations of the two sonas, a relative phase shift starts to develop between the envelopes of the sona signals. Thus, the scattering fidelity of VCSPPs is not expected to oscillate between 1 and -1 indefinitely. Rather, it is expected to decay while oscillating. However, we do not anticipate to see this fidelity decay with our measurement system for this particular perturbation because the SNR of the sonas approaches unity after about $10\mu s$.

The speed of light at $7GHz$ in pure nitrogen gas was faster than it was in the laboratory air (which had about 50% relative humidity). Therefore, as discussed in Sec. 3.2, the VCSPP can be quantified by finding the optimum stretching factor to be applied on the sona that is collected from the cavity filled with nitrogen. The goal is to recover the scattering fidelity of the stretched "nitrogen-sona" and the "air-sona" to 1 (Note that "air-sona" refers to the sona that is collected from the cavity which is filled with air, and likewise for the other gasses). This was achieved by using a stretching factor given by $(4\mu s + 0.07ns)/4\mu s$; because, $t_{gap} = 0.07ns$ ($\approx$ half a period of oscillation of the sona) at $t = 4\mu s$ ($SF \approx -1$) based on the discussion in Sec. 3.3.3. The resulting scattering fidelity is plotted in red (see Fig. 3.5) with the scattering fidelity of the unmodified sonas which is shown in blue. The stretching

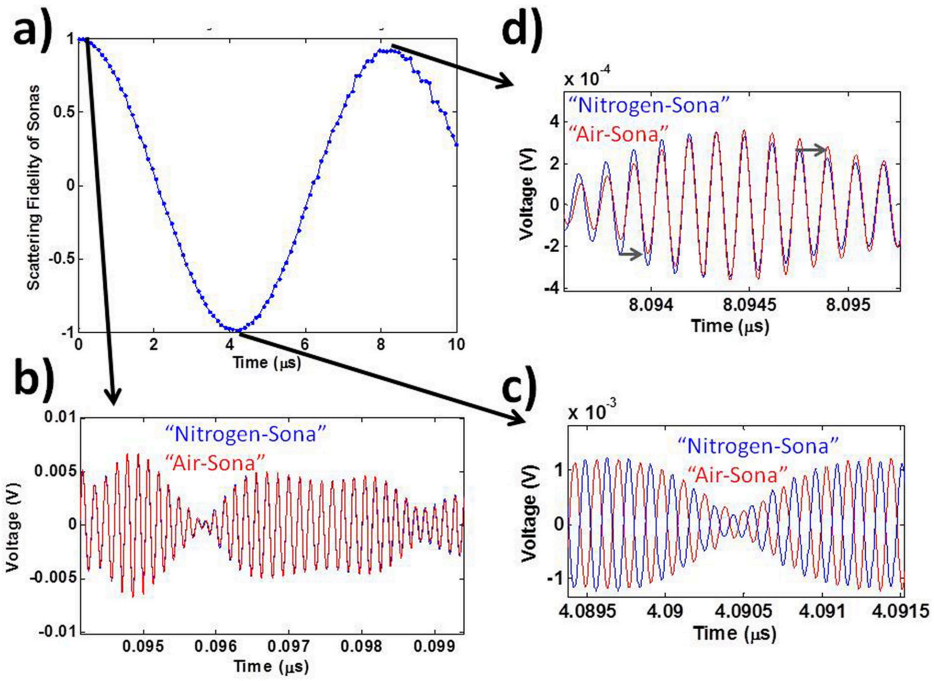

Figure 3.4: (a) Examining the scattering fidelity oscillation for VCSPPs using sona from air filled cavity and sona from nitrogen filled cavity. Each of the sonas are averaged over 100 sona samples. (b) The sonas near $t = 0$ have fidelity of 1. (c) The sonas are out of phase by half a period around $t = 4\mu s$. (d) The sonas are out of phase by a period around $t = 8\mu s$. Besides, the phase shift between the envelopes of the sonas becomes significant.

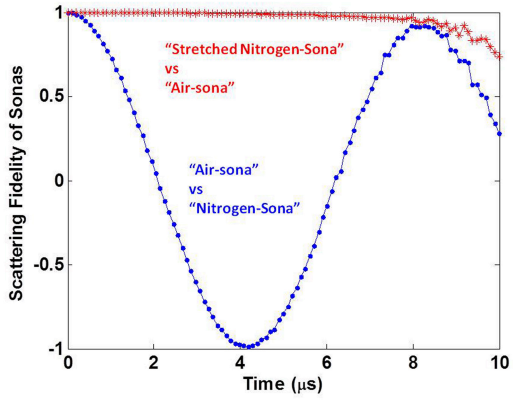

Figure 3.5: Undoing the effect of a VCSPP. The sona that was collected from the cavity filled with nitrogen was stretched out optimally to recover the scattering fidelity to 1 throughout the times when the SNR is robust. The optimum stretching factor quantified the VCSP. The fact that the scattering fidelity was recovered proved that the perturbation was VCSP.

factor $(4\mu s + 0.07ns)/4\mu s \approx 1.000017$ closely approximates $\sqrt{\frac{\epsilon_{r,Air}}{\epsilon_{r,N_2}}} \approx 1.000014$, the expected value of P. This is evidence of the successful measurement of the electrical volume change induced by the VCSPP. The fact that the shape of the cavity was preserved (during the displacement of the air by nitrogen gas) can also be seen from Fig. 3.5. If the shape of the cavity were not preserved, it would not be possible to recover the scattering fidelity of the two sonas through simple numerical stretching of one of the sonas, along the time axis. Hence, displacing air with nitrogen gas is not just a VCP, but is also a VCSPP. Later, a VCP induced by displacement of air with helium, which is not VCSPP, will be discussed.

The fidelity decay, which is expected to be superimposed on the fidelity oscillations, of VCSPPs can be seen for a stronger VCSPP. The VCSP should be strong

enough to bring about a significant phase shift between the envelopes of the sonas before their SNR deteriorates. For our experimental set up, such a strong VCSPP can be achieved by displacing the air in the cavity by helium gas. The scattering fidelity of sona from a cavity that is filled with air and sona from a cavity that is filled with helium is plotted in Fig. 3.6 in blue. Based on the definition in Sec. 3.3.3, $t_{gap} = 0.07ns$ (which is half the period of sona oscillation) at time $t = 0.35\mu s$. Thus, the optimum stretching factor was chosen to be $(0.35\mu s + 0.07ns)/0.35\mu s = 1.0002$. The optimum value was chosen to maximize the average value of the resulting scattering fidelity. Since the speed of light at $7GHz$ is higher in helium than in air, it was the "helium sona" that was stretched out along its time axis. The scattering fidelity of the stretched "helium sona" and the "air sona" is also shown in Fig. 3.6 in red. Once again, the stretching factor $(0.35\mu s + 0.07ns)/0.35\mu s = 1.0002$ closely approximates $\sqrt{\frac{\epsilon_{r,Air}}{\epsilon_{r,He}}} \approx 1.0002$. This shows that the change in electrical volume which was induced by replacing the air in the cavity with helium was quantified successfully. However, unlike the case in Fig. 3.5, the effect of the VCP could not be undone perfectly. The scattering fidelity of the stretched "helium sona" and the "air sona" was not close to 1 throughout time; instead it shows a fidelity decay. The scattering fidelity of "helium sona" and "air sona" is expected to oscillate between 1 and -1 (as the phase shift between the fast oscillations of the sonas increases in a similar fashion to the illustration in Fig. 3.4(b-d)) and decay to 0 (as the phase shift between the complicated envelopes of the sonas increases). This decay is seen experimentally in Fig. 3.6. However, there must be another fidelity decay superimposed on the fidelity decay that can be attributed to a VCP; because the fidelity

decay could not be undone by numerically stretching out one of the sonas.

A FDTD simulation of the experiment was performed to better understand the form of the scattering fidelity when comparing "helium sona" and "air sona". As discussed in Sec. 3.3.2, differences in the dissipation of helium gas and air are so minute that they do not need to be considered. The scattering fidelity of "helium sona" and "air sona", which were obtained from the FDTD model by broadcasting the $7GHz$ pulse used experimentally, are shown in Fig.3.7. The simulation results show that the effect of the VCSPP can be undone by applying the optimum stretching factor (i.e. $(0.35\mu s + 0.07ns)/0.35\mu s = 1.0002$) to the "helium sona". The scattering fidelity of the "air sona" and the stretched "helium sona" is shown in red in Fig.3.7; it is close to 1 which shows that the effect of the perturbation can be undone by simple numerical stretching.

The difference in the results in Fig. 3.6 and Fig. 3.7, shows that experimentally displacing air with helium induces another kind of perturbation other than a volume changing perturbation. Such additional perturbation was not seen when nitrogen was pumped into the cavity at the same pressure setting (i.e. $30psig$) as was used for pumping helium into the cavity. This discrepancy can be explained by the fact that helium gas has a significant buoyancy force which slightly flexes the walls of the cavity (about $1m^2$ area, and $3mm$ thick aluminum sheets); because, from previous work on this cavity, it was shown that a flexing of one of the walls of the cavity can cause a significant shape changing perturbation [25]. The result shown in Fig. 3.6 demonstrates that it is possible to verify if the shape of the cavity remained intact while its electrical volume changed. This verification can be simply done by checking

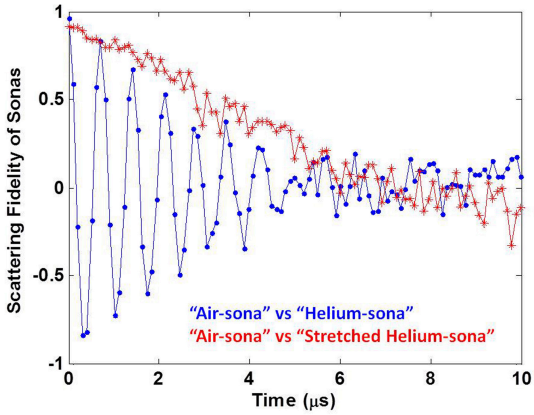

Figure 3.6: Scattering fidelity of sona from a cavity filled with air and sona from a cavity filled with helium. The fidelity oscillations and decay can be seen. The effect of the VCP could not be completely undone by stretching the "helium sona", so, the perturbation is not VCSP. The buoyant force of helium gas can slightly change the shape by flexing the walls of the cavity.

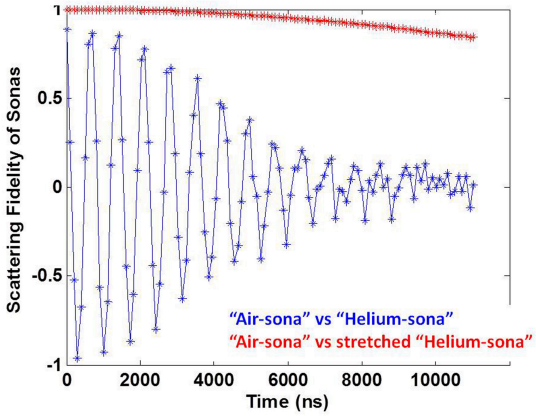

Figure 3.7: Scattering fidelity of sona from a cavity filled with air and sona from a cavity filled with helium. The sonas are generated from the FDTD model of the cavity.

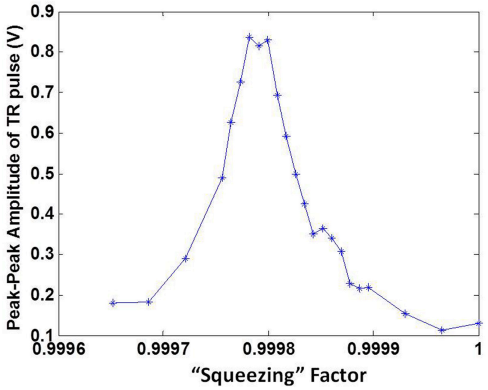

Figure 3.8: Plot of peak-to-peak amplitude of time-reversed pulse in a cavity filled with Helium vs "squeezing" factor used to scale the time axis of the sona which is collected from a cavity filled with Nitrogen.

if the scattering fidelity can be recovered to 1 throughout time. The capability to detect changes to the shape of the cavity during a volume changing perturbation (which could be induced by a spatially uniform heating or cooling of a homogenous cavity) can have several applications as was pointed out in Sec. 3.1.

3.3.4.2 Sensing Using Time Reversal

So far, only one of the sensing techniques introduced in Sec. 3.2 is demonstrated to quantify volume changing perturbations. In addition to the scattering fidelity technique, time reversal mirrors can be used to quantify volume changing perturbations. When a sona signal that is collected from the cavity filled with nitrogen is time reversed and broadcast into the cavity filled with helium, the reconstructed time reversed pulse is not expected to be ideal. This is because the time reversed sona would be traversing an effectively smaller cavity. Note that in this

particular case, the baseline cavity is electrically larger than the perturbed cavity. Based on the discussions in Sec. 3.2, the baseline sona should be squeezed along its time axis using an optimum factor to recover the maximum amplitude time reversed pulse. When the optimally squeezed "nitrogen sona" is time reversed and broadcast into the cavity filled with helium, the reconstructed time reversed pulse is expected to better approximate the original pulse.

As detailed in Chapter 2, the improvement in the quality of the time reversed reconstructed pulse can be measured in various ways [20]. Here, the simplest measure (the peak-to-peak-amplitude (PPA) of the reconstructed pulse) of the quality of the time reversed pulse is used. Fig. 3.8 shows the PPA of the time reversed reconstructed pulse obtained when the "nitrogen sona" is numerically squeezed along its time axis by varying amounts. The optimum squeezing factor of 0.9998 closely approximates $\sqrt{\frac{\epsilon_{r,He}}{\epsilon_{r,N_2}}} \approx 0.9998$. This shows that the time reversal technique can also be used to quantify volume changing perturbations. Time reversal mirrors can also be used to detect when a volume changing perturbation slightly changes the shape of the cavity. In this case, when the "nitrogen sona" is time reversed and broadcast into the cavity filled with nitrogen, the PPA of the reconstructed time reversed pulse was about $1.13V$. However, when an optimally squeezed "nitrogen sona" is broadcast into the cavity filled with helium gas, the optimal value of the PPA is only about $0.85V$. This indicates that the perturbation, which is induced when the nitrogen gas inside the cavity is displaced with helium gas, is not just a volume changing perturbation but also a shape changing perturbation. Once again, this is due to the relatively strong buoyant force of helium gas which can flex the

walls of the cavity.

To summarize, either of the two time domain sensing techniques introduced in Sec. 3.2 can be used to identify and quantify a VCSPP. However, the sensing technique based on time reversal can have an advantage because it is computationally cheaper [20]. This advantage is more readily capitalized when an acoustic time reversal mirror is used. Because, the equipment for the electromagnetic time reversal mirror (which includes an Arbitrary Waveform Generator) is more expensive than the equipment needed for the sensing technique based on scattering fidelity.

3.3.5 Limitation of the Time Domain Approaches to Measure VCSPP

Based on the discussion in Sec. 3.2, there should be an overlap between the resonances excited in the baseline and perturbed system, for the time domain sensing techniques to work. Thus, both of the time domain sensing techniques (based on scattering fidelity and time reversal mirrors) face a limitation regarding the maximum VCSPP that can be measured. This limitation can be improved by increasing the bandwidth of the pulse that is used to probe the cavity. Doing so would effectively make the time domain technique closer to the frequency domain interrogation of the system, which does not face a limit on the maximum VCSPP that can be measured. In a similar spirit, using a pulse with a flat bandwidth (such as a chirp) may also be helpful.

The regime of VCSPP strengths that cannot be measured using the time

domain techniques is estimated as follows. Suppose that the probing pulse excites resonances with frequencies ranging from f_{min} to f_{max}, with the center frequency at $f = \frac{f_{min}+f_{max}}{2}$. The probing pulse is considered to excite frequencies from f_{min} to f_{max} with at least the conventionally defined minimum power level, which is chosen based on the given noise power (which is $-30dBm$ for the system described in Sec. 3.3.1). The VCSPP changes the volume of the cavity by a factor of P^3, where $P > 1$ for simplicity. Once again, the VCSPP has the effect of scaling the $|S_{12}|^2(f)$ of the cavity along the frequency axis by a factor of P. If $\frac{f_{max}}{P} < f_{min}$, then the VCSPP certainly cannot be measured by using this probing pulse in the time domain because there would be no overlap between the resonances excited in the baseline and perturbed cavities.

Next, the conditions for the maximum VCSPP that can be measured are formulated. Assume that the pulse has a constant magnitude (for example, with only about $10dB$ allowance for power fluctuations) around an f_ϵ neighborhood of f in the frequency domain (i.e. $f - f_\epsilon$ to $f + f_\epsilon$). For reasons to be explained later, f_ϵ should be a frequency value which satisfies $f_\epsilon < f - f_{min}$, and $f_\epsilon \gg \Delta f$, where Δf is the mean spacing between the resonant frequencies of the baseline cavity. If $\frac{f+f_\epsilon}{P} > f$, the following conditions hold. The resonances excited in the baseline cavity between f and $f + f_\epsilon$ are also excited (with the same magnitude) in the perturbed cavity between $\frac{f}{P}$ (which can be shown to be greater than $f - f_\epsilon$ for $P > 1$) and $\frac{f+f_\epsilon}{P}$. This means that there is common information content (i.e. resonances excited) inside the baseline and perturbed sonas. In other words, the baseline and perturbed sonas contain information that is equivalent to a frequency

domain interrogation of the system over a narrow bandwidth. To retrieve this common information, the baseline and perturbed sonas can be band-pass filtered with a pass-band from f to $f + f_\epsilon$ and with a pass-band from $\frac{f}{P}$ to $\frac{f+f_\epsilon}{P}$ respectively. The value of f_ϵ is predetermined from the shape of the pulse. The sonas can be band pass filtered with an educated guess for P, and the resulting filtered sonas can be compared after stretching out the baseline sona along the time axis with the same educated guess for P. This iterative process can be repeated until the optimum value of P which quantifies the VCSPP is determined: here, the objective optimal result is the maximization of the average value of the resulting scattering fidelity of the two sonas.

Therefore, the maximum VCSPP that can be measured is P^3 where $P \approx \frac{f+f_\epsilon}{f}$, for f_ϵ that satisfies the above mentioned requirements.

In the experiments discussed in Sec. 3.3.1, the strongest VCP that was induced in the laboratory had $P \approx 1.0002$. This was for comparison of cavities filled with air (at $\approx 50\%$ relative humidity) and helium gas at 20^0C. The bandwidth and center frequency of the probing pulse were $1GHz$ and $7GHz$ respectively. The mean spacing between the resonant frequencies of the baseline cavity is given by $\Delta f = \frac{\lambda^3}{V}\frac{f}{8\pi} \approx 22kHz$; where V is the volume of the baseline cavity, $f = 7GHz$ is the center frequency of the pulse, and λ is the wavelength. The pulse had a Gaussian envelope, hence a conservative estimate for f_ϵ is $10MHz$ (i.e. 1% of the bandwidth, and about 500 resonances between f and $f + f_\epsilon$). Therefore, the maximum VCSPP that can be measured in the cavity introduced in Sec. 3.3.1 is $P \approx \frac{7GHz+10MHz}{7GHz} \approx 1.001$ (using the $7GHz$ pulse). Clearly, the VCSPP that was

achieved in the laboratory (i.e. $P \approx 1.00002$ for nitrogen gas vs the air) is much smaller than the conservative estimate for the maximum VCSPP that could have been measured (i.e. $P \approx 1.001$).

The case of a strong VCSPP perturbation, which cannot be measured using the time domain techniques, is best considered using a simulation tool that can be easily interrogated in the frequency domain as well. Sec. 3.4 discusses such strong perturbations, and shows how they can be quantified using a frequency domain approach.

3.4 Sensing Using Frequency Domain Information

In Sec. 3.2, it was mentioned that VCSPPs can be quantified using information obtained in the time domain or frequency domain. The time domain approach is generally more practical in applications. However, the frequency domain approach does not have limitations on the maximum perturbation value that can be quantified. This frequency domain approach is used to measure VCSPPs on a quasi-1D system called the star graph. We use the star graph because it is a type of quantum graph that has generic properties of wave chaotic systems [63], but is relatively simple to understand and simulate. Besides, the star graph can be directly implemented in the frequency domain as discussed in Sec. 3.4.1.

3.4.1 The Star Graph Model

The star graph is numerically modeled as a set of interconnected transmission lines as shown, schematically, in Fig. 3.9 [30]. The system is a one port system, hence, the input signal is injected into the driving transmission line and the output signal is also retrieved from the same line. The driving transmission line has zero length. The driving transmission line is connected with a number of transmission lines which are all connected in parallel with each other. The transmission line properties (for a line labeled by i) are length (L_i), characteristic admittance (Y_{ci}), frequency dependent complex propagation constant ($\gamma_i(\omega)$), and complex reflection coefficient (Γ_i) (for reflection from the terminations of the lines that are not connected to the driving line). The driving line has zero length, thus its only adjustable property is its characteristic admittance (Y_{cd}).

This one port system is modeled by using the analytically derived expression for its scattering parameter as a function of frequency, $S_{11}(\omega)$. The scattering parameter, $S_{11}(\omega)$, can be expressed in terms of the characteristic admittance of the driving line (Y_{cd}) and the input admittance (Y_i) of each of the other transmission lines while looking towards them,

$$S_{11}(\omega) = \frac{Y_{cd} - \sum_{i=1}^{i=N} Y_i(\omega)}{Y_{cd} + \sum_i Y_i(\omega)}, \tag{3.2}$$

where N is the number of transmission lines connected in parallel. The input admittance of each transmission line (labeled by i), $Y_i(\omega)$, can be expressed in terms of the above mentioned properties of the line,

$$Y_i(\omega) = Y_{ci}\left(\frac{1 - \Gamma_i e^{2\gamma_i(\omega)L_i}}{1 + \Gamma_i e^{2\gamma_i(\omega)L_i}}\right). \tag{3.3}$$

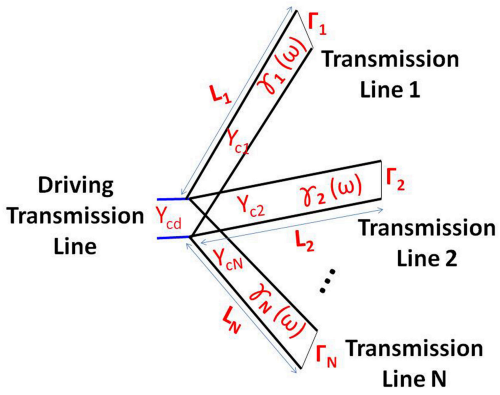

Figure 3.9: Schematic of the star graph model. There are N transmission lines that are connected in parallel, and a driving transmission line of zero length. Each of the N lines (labeled by i) can have unique length (L_i), characteristic admittance (Y_{ci}), frequency dependent propagation constant ($\gamma_i(\omega)$), and reflection coefficient (Γ_i). The driving line has a characteristic admittance of Y_{cd}.

Once the scattering parameter of the system is computed over a broad frequency range, the response to any time domain input signal can be calculated. This is done by Fourier transforming the input signal to the frequency domain, multiplying it by the scattering parameter ($S_{11}(\omega)$) and inverse Fourier transforming the product back to the time domain. This establishes the star graph model as a time domain simulation of this quasi-1D system. However, in this section we are mainly interested in the frequency domain representation of the star graph using its scattering parameter. The frequency domain approach will be shown to be effective in quantifying strong perturbations that could not have been measured otherwise.

3.4.2 Quantifying Strong Perturbations to the Star Graph

As discussed in Sec. 3.2, the scattering parameter of a cavity can be used to quantify a VCSPP. The star graph is a quasi-1D system. A perturbation that changes the length of all of the lines of the star graph by the same proportion (i.e. with constant P) effectively changes its volume while leaving its shape intact (i.e. it is a VCSPP). The effective volume of a star graph with N lines is given by $2\sum_{i=1}^{i=N} L_i$ [64]. Therefore, for a VCSPP perturbation that scales the length by a factor of P, the effective volume of the star graph also changes by a factor of P. This is different from the case of the 3D cavity discussed in Sec. 3.3 (i.e. the volume of the 3D cavity changes by P^3).

The baseline star graph was set up using the following parameter values. There were 10 lines whose length is given by $L_i = 0.3\lceil 10\sqrt{i}\rceil$ m (for i ranging from 1 to 10). Each of these lines had a characteristic admittance, Y_{ci}, of $1S$. The characteristic admittance of the driving line was chosen such that $Y_{cd} = \sum_{i=1}^{i=10} Y_{ci} = 10S$ in order to eliminate prompt reflection of signals injected through the driving line. The propagation constant of the lines is a function of the frequency, ω, and was given by $\gamma_i(\omega) = \imath\frac{\omega}{c}$ with $i = 1, ..., N$, where c is the speed of light in vacuum; thus, the lines themselves were considered to be lossless (i.e. $\gamma_i(\omega)$ does not have a real part). However, energy was dissipated during reflections from the terminations of the lines. The reflection coefficient from the termination of the lines was given by $\Gamma_i = e^{\frac{-0.3\lceil 10\sqrt{i}\rceil 2}{c\tau}}$ with $i = 1, ..., N$, where $\tau = 1.5\mu s$. The amount of dissipation was designed to be independent of the size of the star graph, which is changed by a

VCSPP. However, the dissipation introduced through non-unit values of Γ_i can be interpreted as an equivalent loss that could be introduced through $\gamma_i(\omega)$ (i.e. by introducing $\frac{1}{c\tau}$ as the real part of $\gamma_i(\omega) = \imath\frac{\omega}{c} + \frac{1}{c\tau}$). Thus, if the dissipation were modeled using $\gamma_i(\omega)$, $\tau = 1.5\mu s$ would be interpreted as the time it takes the signals to decay by $1/e$ as they propagate along the lines. As a result, the typical $1/e$ decay time of the sona from the star graph was $\approx 1.5\mu s$, a value typical of our 3D experiment.

The perturbed star graph was set up using identical values of parameters as the baseline star graph, except for the length, L_i. The lengthes of the perturbed star graph were chosen to be PL_i, where P is the perturbation strength. The driving line has zero length in both the baseline and perturbed star graphs.

3.4.2.1 Using the Time Domain Approaches

A Gaussian pulse of width $1ns$ and center frequency $7GHz$ was used to generate a baseline and perturbed sona from the baseline and perturbed star graphs. The time domain sensing technique which is based on scattering fidelity was applied to quantify a perturbation of strength $P = 1.0002$. Fig. 3.10 shows the scattering fidelity of the baseline and perturbed sonas before (blue) and after (red) optimally stretching the baseline sona. This demonstrates that the scattering fidelity sensing technique can be used to quantify a VCSPP in the quasi-1D chaotic system. The result gives the clearest evidence to the discussion of fidelity decay induced by VCSPPs in Sec. 3.3.4.1 (i.e. the results shown in Figs. 3.5 and 3.6). VCSPPs induce a

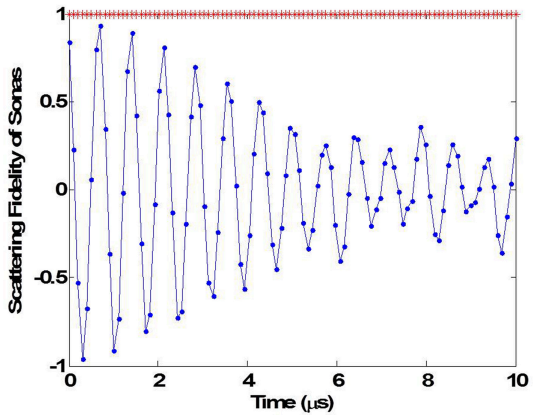

Figure 3.10: Scattering fidelity of baseline and perturbed sonas from the star graph before (blue) and after (red) optimally scaling the baseline sona along its time axis. The perturbation is a VCSPP with $P = 1.0002$.

scattering fidelity oscillation that is superimposed on a fidelity decay (see Fig. 3.10).

The application of the time domain sensing technique which is based on time reversal is presented in Fig. 3.11. Fig. 3.11 shows the PPA of the time reversed pulse reconstructed using the baseline sona scaled with different factors along its time axis. The optimal PPA was obtained when the sona was scaled by a factor exactly equal to the stretching of the transmission line lengths (i.e. 1.0002).

The perturbation strength of $P = 1.0002$ was shown to be detectable using time domain techniques in the star graph set up described. However, as the perturbation got stronger, the shortcoming of the time domain techniques was revealed. For perturbation strength values, P, ranging from 1.0002 to 1.14, the $SF(t)$ of the perturbed sona and the optimally scaled (along the time axis) baseline sona was

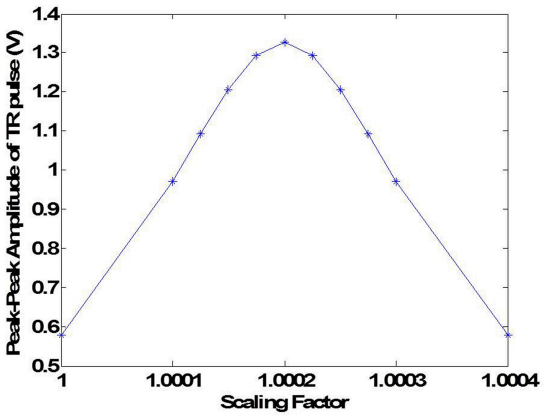

Figure 3.11: Peak-to-peak amplitude (PPA) of time reversed pulse reconstructed inside the perturbed star graph using the baseline sona which is scaled along its time axis by different scaling factors.

examined. For each P, the $SF(t)$ was averaged over time, t (from $0s$ to $10\mu s$, which is the duration of the sonas). The closeness of the average $SF(t)$ to 1 indicates the success of the time domain technique to undo the effect of the VCSPP, and to measure it. Fig. 3.12 shows the average value of $SF(t)$ (for optimally scaled baseline sona) versus $\log_{10}(P)$; the standard deviations of $SF(t)$ taken over t are also shown as an error bar in Fig. 3.12. As P increased beyond about $10^{.025} \approx 1.06$, the effectiveness of the time domain sensing technique starts to deteriorate.

Based on the discussion in Sec. 3.3.5, the maximum VCSPP that can be measured using time domain techniques in this realization of the star graph is $P \approx \frac{f+f_\epsilon}{f} \approx \frac{7GHz+200MHz}{7GHz} \approx 1.03$. The value of f_ϵ defined in Sec. 3.3.5 was chosen to be $200MHz$ to satisfy the requirement that $f_\epsilon >> \Delta f$. The mean spacing between resonant frequencies of the baseline star graph is $\Delta f = \frac{c}{2\sum_{i=1}^{i=N} L_i} \approx 2MHz$, where N is the number of lines in the star graph [64]. Thus, about 100 resonances exist in the

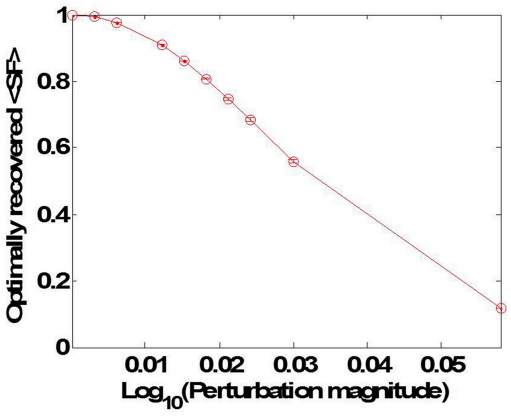

Figure 3.12: The average $SF(t)$ of the baseline sona and perturbed sonas, which are optimally scaled by P (perturbation magnitude) along their time axis. The sonas were collected from the baseline star graph, and a perturbed star graph (VCSPP with P). The average $SF(t)$ was taken from time $t = 0s$ to $t = 10\mu s$ of the sonas; error bars show the associated standard deviation.

baseline star graph between $f = 7GHz$ and $f - f_\epsilon = 6.8GHz$, and $f_{min} \approx 6GHz$ for the Gaussian pulse with $1GHz$ bandwidth (and noiseless simulation). The conservative estimate for the maximum VCSPP that can be measured (i.e. $P \approx 1.03$ or $\log_{10}(P) \approx 0.012$) is consistent with the result illustrated in Fig. 3.12, which suggests that a VCSPP of $P \approx 10^{.025} \approx 1.06$ might be quantifiable.

3.4.2.2 Using the Frequency Domain Approach

The limitation of the time domain approach was discussed in Sec. 3.3.5, and demonstrated using the star graph in Sec. 3.4.2.1. As shown in Fig. 3.12, for a strong perturbation such as $P = 1.14$, the time domain sensing techniques fail to undo the effect of the VCSPP, and hence to measure it. Here, a frequency domain

approach is used to illustrate how the VCSPP with $P = 1.14$ can be measured.

Fig. 3.13(a) shows the $|S_{11}|^2(\omega)$ of the baseline (blue) and perturbed (red) star graphs. The $|S_{11}|^2(\omega)$ of the perturbed star graph (larger in size by a factor of $P = 1.14$) is compressed along the frequency axis compared to the baseline's case. This effect was predicted in Sec. 3.2, and schematically illustrated in Fig. 3.1. The frequency domain approach to measure VCSPP involves optimally scaling the frequency axis of the scattering parameter of the perturbed system (star graph in this case) to align it with the scattering parameter of the baseline system. Fig. 3.13(b) shows the $|S_{11}|^2(\omega)$ of the baseline star graph (blue) and the optimally stretched $|S_{11}|^2(\omega)$ of the perturbed star graph (black). The optimal frequency scaling factor was $P = 1.14$, which also successfully measures the VCSPP induced on the baseline star graph. To conclude, given the scattering parameters of a baseline and a perturbed system, one can check if a VCSPP happened, and quantify it.

3.5 Discussion

The development of this quantitative sensor opens up possibilities for several potentially useful applications. For example, when a cavity that has a homogenous material make up is cooled down (or warmed up), it is interesting to check if the temperature stays uniform throughout all parts of the cavity. The sensor developed in this paper would allow one to check if the volume of the cavity is decreasing (or increasing) while the shape is intact; the sensor would also allow one to measure by how much the volume (and hence the temperature) of the cavity is changing. This

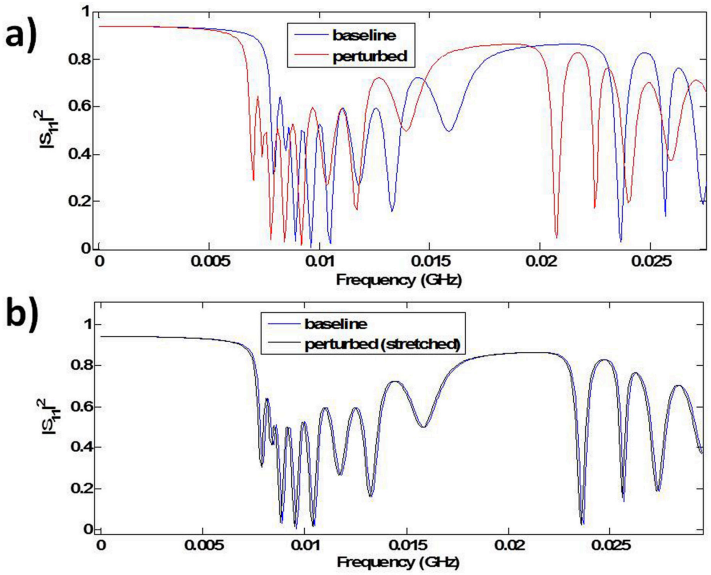

Figure 3.13: Quantifying a volume changing perturbation in the frequency domain. (a) The $|S_{11}|^2(\omega)$ of the baseline (blue) and a perturbed (red) star graph for perturbation strength $P = 1.14$. (b) The $|S_{11}|^2(\omega)$ of the baseline star graph (blue), and the $|S_{11}|^2(\omega)$ of the perturbed star graph (black) after optimal frequency scaling which measures the VCSPP.

is one possible application of VCSPP sensor which can practically compete with the traditional option of installing thermometers throughout the cavity. Another possible application of the VCSPP sensor is monitoring to check if a fluid has displaced another fluid uniformly throughout a cavity. Since the speed of the waves inside different fluids can be different, the displacement of the fluid can change the volume of the cavity, as seen by the waves. This assumes that other wave properties (such as dissipation and dispersion) of the two fluids are similar.

3.6 Conclusion

Quantifying a generic perturbation to a wave chaotic enclosure is a challenge because the effect of a perturbation on the dynamics of waves is not generally very well understood. However, the effect of a perturbation that changes the volume but keeps the shape intact can be theoretically predicted. The theoretical prediction is most clear in the frequency domain. Thus, quantifying volume changing perturbations is best done in the frequency domain. Nonetheless, time domain approaches can be preferred for practical purposes. The time domain approach is limited by a maximum perturbation that can be measured. This limitation was demonstrated using a simulation of a star graph, which is a representative wave chaotic system. The time domain approach can work using either scattering fidelity techniques or the Loschmidt echo. Quantification of a volume changing perturbation was experimentally demonstrated using these techniques. The volume changing perturbation was induced experimentally by changing the electrical volume of the cavity. The

results of the experiment were compared with FDTD simulation results of the cavity and good agreement was found.

Chapter 4

Iterative Time Reversal with Tunable Convergence

Time reversal mirrors were introduced and used for sensing applications in Chapters 2 and 3. In this chapter, we propose and test a tunable iterative technique for improving the temporal focusing of a time reversal mirror [30]. A single amplification parameter is used to tune the convergence of the iteration. The tunable iterative technique is validated by tests on the experimental electromagnetic time reversal mirror. The technique is also tested on the star graph numerical model, which was first introduced in Chapter 3.

The iterative technique can potentially be used in many applications which already utilize time reversal. Some examples of these applications are: the improvement of communication systems [48, 49], and the sharpening of targeted energy focusing [38]. These applications would benefit from enhanced spatiotemporal focusing.

4.1 Introduction

Spatiotemporal focusing of waves has applications in fields such as imaging and communication. Time reversal (TR) mirrors have been used to focus waves in both space and time [21]. An ideal TR mirror consists of a wave source located inside a lossless medium that is completely enclosed by a surface of transceivers.

The transceivers record and absorb the signal initially broadcast by the source. Later, the transceivers rebroadcast a time reversed version of the recorded waves in a coordinated fashion. Because of the TR invariance of the lossless wave equation, the waves undo all phase shifts acquired while propagating forward in time and focus on the location of the source and reconstruct a time reversed version of the original signal. In practice, TR mirrors have several limitations that result in loss of information about the waves broadcast by the source. These limitations include i) limited coverage by the transceivers, and ii) dissipation during the wave propagation (which breaks TR invariance) [26, 18].

The first limitation of TR mirrors can be overcome by the use of a reflecting wave chaotic cavity with partial spatial coverage of the transceivers, along with a long recording time [26]. However, the limitation due to dissipation persists, and leads to increasing loss of information as the recording time increases.

The loss of information during the reconstruction results in temporal and spatial sidelobes of the reconstructed pulse. In Chapter 2, we used the exponential amplification technique to partially undo the adverse effects of dissipation. The objective in Chapter 2 was to enhance the range of the TR based sensors, which suffered from dissipation [18, 20]. However, this technique does not directly improve the temporal focusing of the reconstructed pulse. In fact, as will be described in Chapter 5, it worsens the temporal focusing of the reconstructed pulse upon recording. However, Chapter 5 will also show that the temporal focusing can be restored (and actually enhanced) if exponential de-amplification is carried out on the digitized reconstructed pulse. In any event, the exponential amplification technique

is not applicable if the temporal focusing of the reconstructed pulse is demanded in real time (and not after manipulations of the digitized reconstructed pulse). This may be a requirement for applications such as electromagnetic weapons [38], where energy needs to be focused at a target in real time. On the other hand, Ref.[27] has introduced an iterative TR technique which has been shown to be effective in eliminating the spatiotemporal sidelobes of the reconstructed pulse. The iterative TR enables spatiotemporal focusing in real time.

In this chapter, we introduce a single parameter into the iterative TR technique, [27]. The parameter is designed to compensate for loss. By tuning this parameter, we can substantially improve the accuracy and convergence of the iterative focusing technique. This is demonstrated both experimentally and numerically. Sec. 4.2 outlines the algorithm of the tunable iterative TR mirror. Sec. 4.3 and Sec. 4.4 describe the experimental set up of the electromagnetic TR mirror, and simulation set up of the star graph, which are used to test the tunable iterative technique, respectively. Sec. 4.5 presents the experimental and numerical results. Sec. 4.6 discusses modifications to the iterative algorithm to overcome experimental challenges. Sec. 4.6 further discusses potential applications of the tunable iterative technique. Sec. 4.7 is the conclusion.

4.2 The Iterative Time Reversal Algorithm with a Convergence Parameter

The iterative TR algorithm was first introduced using acoustic waves [27]. Here, an improvement to the algorithm is introduced. From now on, a signal, X, is assumed to be frequency dependent by default. The inverse Fourier transform of X is denoted as $\mathcal{F}^{-1}[X]$, which is a time domain signal.

Consider a regular TR mirror operation that involves broadcasting an original pulse, $\mathcal{F}^{-1}[O]$, into a cavity with a single port. Denote the scattering parameter of the system by H. We call the response signal received at the port the sona, $\mathcal{F}^{-1}[S]$. Thus, $S_1 = HO + b_0$, where the subscript on S indexes the iteration, and b_0 is additive white Gaussian noise (AWGN). For a regular TR (which is the first step of the iteration), the sona, $\mathcal{F}^{-1}[S_1]$, is time reversed (phase conjugated, as S_1^*, in the frequency domain) and broadcast back into the cavity to retrieve the reconstructed pulse at the first iteration, $\mathcal{F}^{-1}[R_1] = \mathcal{F}^{-1}[HS_1^* + a_1] = \mathcal{F}^{-1}[HH^*O^* + Hb_0^* + a_1]$. Here, a_1 is AWGN that is picked up during the recording of $\mathcal{F}^{-1}[R_1]$. Note that in the ideal case $b_0 = a_1 = 0$ (no noise) and $|H|^2 = 1$ (no cavity losses), and $\mathcal{F}^{-1}[R_1]$ is thus equal to $\mathcal{F}^{-1}[O^*]$ (i.e., a time reversed original signal). However, if losses are present $|H|^2$ is frequency dependent and less than unity. The iterative algorithm calculates a new sona signal, $\mathcal{F}^{-1}[S_{n+1}]$, by subtracting a correction signal, $\mathcal{F}^{-1}[C_n]$, from the previous sona, $\mathcal{F}^{-1}[S_n]$, (i.e. $\mathcal{F}^{-1}[S_{n+1}] = \mathcal{F}^{-1}[S_n] - \mathcal{F}^{-1}[C_n]$); and, the algorithm uses the newly calculated sona, $\mathcal{F}^{-1}[S_{n+1}]$, to generate a new reconstructed pulse, $\mathcal{F}^{-1}[R_{n+1}]$, iteratively (i.e. $\mathcal{F}^{-1}[R_{n+1}] = \mathcal{F}^{-1}[HS_{n+1}^* + a_{n+1}]$). The correction signal

can be interpreted as the part of the sona that resulted in the sidelobes during the reconstruction. The correction signal is obtained by first computing the sidelobes in $\mathcal{F}^{-1}[R_n]$ which are given by $\mathcal{F}^{-1}[R_n - O^*]$. Then, the sidelobes during the n^{th} reconstruction, $\mathcal{F}^{-1}[R_n - O^*]$, are time reversed and broadcast into the system to determine the correction signal, $\mathcal{F}^{-1}[C_n] = \mathcal{F}^{-1}[H(R_n - O^*)^*k + b_n]$. Once again, b_n is AWGN that is picked up while $\mathcal{F}^{-1}[C_n]$ is recorded, and k is a new real scalar parameter discussed below. k is independent of frequency.

The advantage of introducing the parameter k is revealed by the expression for the n^{th} iterated reconstructed pulse R_n that is derived from the previous equations:

$$R_n = [1 - (1 - HH^*k)^{n-1}]O^* + HH^*(1 - HH^*k)^{n-1}O^* + \sum_{j=0}^{n-1}(1 - HH^*k)^j Hb^*_{n-1-j} - \sum_{j=0}^{n-2}(1 - HH^*k)^j HH^*ka_{n-1-j} + a_n \qquad (4.1)$$

Note that for $k = 1$, Eq. 4.1 reduces to the result in Ref.[27]. The goal of the algorithm is to make R_n converge to O^* (i.e. the phase conjugated version of the original pulse) as n increases. The first two terms in Eq. 4.1 show that the convergence of the iteration can be hastened if k is chosen to make HH^*k as close to 1 as possible over the bandwidth of the pulse. In addition, the first two terms dictate the following condition for the convergence of the iteration: HH^*k should be smaller than 2 for all frequencies within the bandwidth of the pulse. On the other hand, the third and fourth terms in Eq. 4.1 show that the iteration may diverge if $HH^*k > 2$ over the bandwidth of the AWGN (i.e. a_n and b_n). Therefore, heuristically, the optimum k value for the fastest convergence of the iteration is chosen as $\frac{2}{\max(HH^*)}$, where $\max(HH^*)$ is the maximum of HH^* taken over the bandwidth of both the

pulse and the AWGN after filtering. Using $k \ll \frac{2}{\max(HH^*)}$) is a conservative approach which guarantees that the R_n will continue to approach O^* regardless of the value of n. Choosing $k \approx \frac{2}{\max(HH^*)}$ generally speeds up the convergence; however, there is a risk of divergence at higher n values if the measured value of $\max(HH^*)$ was underestimated. $\max(HH^*)$ is determined from an initial reference experiment which measures H of the system in the frequency domain. The tunable iterative TR algorithm can be carried out with the optimum k value after the H of the system is measured.

One may argue that the need for the initial reference experiment renders the iterative technique useless because once H is measured in the frequency domain, the inverse filter technique [28, 27] could be used instead. The inverse filter technique computes $\mathcal{F}^{-1}[(H^{-1}O)^*]$ and broadcasts it into the cavity to achieve spatiotemporal focusing of $\mathcal{F}^{-1}[H(H^{-1}O)^*] = \mathcal{F}^{-1}[O^*]$. Unlike the inverse filter technique, the initial reference experiment is done to approximately determine solely $\max(HH^*)$. Therefore, the iterative technique is still preferable because it does not require an extremely accurate determination of H over a large dynamic range. Besides, in the case of a multi-port experiment where H is a large matrix, the inverse filter technique suffers from the computational cost and instability of matrix inversion [27]. From Eq. 4.1, it can be shown that as $n \to \infty$, the expression for R_n approaches $HH^{-1}O^* = O^*$, which is equivalent to the result of the inverse filter technique [27].

4.3 The Electromagnetic TR Mirror Experimental Setup

The tunable iterative TR method was tested on a $1m^3$ aluminum box resonant cavity with interior scatterers, which was first introduced in Sec. 3.3.1. The box had two electrical ports that were connected to an oscilloscope, and a microwave source (see Fig. 4.1). Spatial reciprocity between the two ports simplifies the experiment because the connections to the oscilloscope and the source need not be exchanged. Fig. 4.1 illustrates how the two steps of the regular TR (i.e. the 1^{st} step of the iterative algorithm) were carried out [25]. Although our derivation above assumed a 1-port situation, it is expected that the results will also apply on this 2-port configuration [27]. For a 1-port system, the S_{11} scattering parameter is considered as H in Eq. 4.1. Whereas, for a 2-port system, the S_{12} scattering parameter is considered as H in Eq. 4.1.

4.4 The Star Graph Model

The tunable iterative TR technique was also tested using simulation of the star graph. The star graph was first introduced in Sec. 3.4.1. It is a linear system consisting of a driving transmission line that is connected to a number of transmission lines. The lines are all connected in parallel. A sketch of the star graph is shown in Fig. 3.9.

The following parameters of the star graph were chosen to create an under-coupled cavity [11]. For an under-coupled cavity, energy loss due to dissipation dominates energy loss due to poor coupling. We chose to set up the star graph

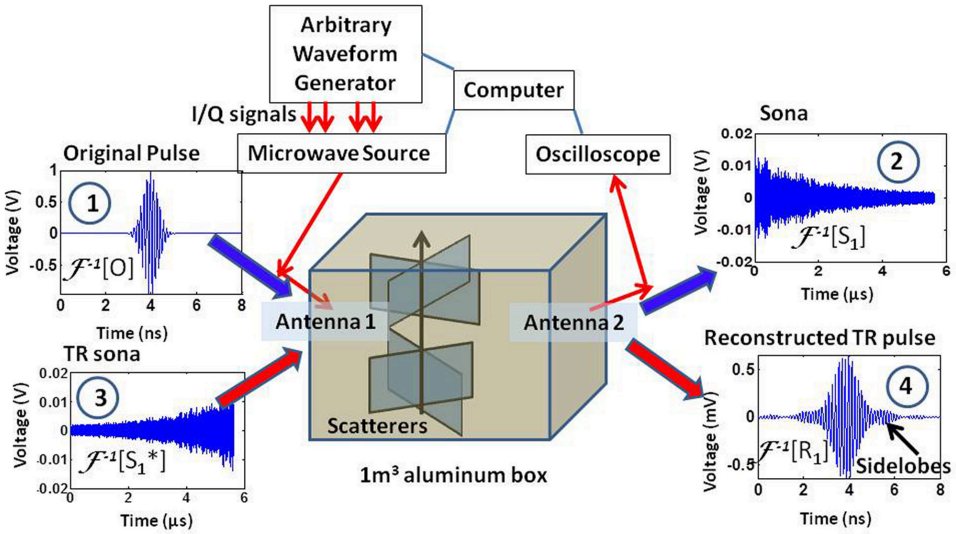

Figure 4.1: Schematic of the electromagnetic time reversal (TR) mirror experiment. The 1^{st} step of the tunable iterative TR mirror operation involved the following. First, the original pulse ($\mathcal{F}^{-1}[O]$) was broadcast through antenna 1 (1), and the resulting sona ($\mathcal{F}^{-1}[S_1]$) was collected at antenna 2 (2). Next, the time reversed sona ($\mathcal{F}^{-1}[S_1^*]$) was injected into the system at antenna 1 (3) to retrieve the reconstructed time reversed pulse ($\mathcal{F}^{-1}[R_1]$) at antenna 2 using spatial reciprocity (4). Experimental data are shown for each step.

as an under-coupled cavity because, we are trying to clearly illustrate how the iterative technique mitigates the adverse effects of dissipation. The experimental cavity considered in Sec. 4.3 is also an under-coupled cavity.

There were 50 transmission lines in the star graph set up, excluding the driving line. The lines had length $L_i = \sqrt{i}\ m$ where i labels each line ranging from 1 to 50. The driving line had zero length. All of the lines had a characteristic admittance $Y_{ci} = 1S$, except the driving line which had a characteristic admittance of $Y_{cd} = \sum_{i=1}^{i=50} L_i = 50S$. The choice of the characteristic admittances eliminated prompt reflections when signals were injected through the driving line. Each of the 50 transmission lines had a reflection coefficient of $\Gamma_i = 1$ at their terminations. The frequency dependent propagation constants of the lines were given by $\gamma_i(\omega) = \imath\frac{\omega}{c} + \alpha_i$ where c is the speed of light, and α_i is the loss constant on line i. The loss constant on each of the 50 lines was $\alpha_i = \frac{1}{c\tau}$ where $\tau = 0.5\mu s$. τ signifies the equivalent $1/e$ voltage decay time of the waves on the lines.

The pulse is injected through the driving line. After the pulse reverberates through the lines connected in parallel, it comes back out through the driving line to form the model sona. This simple quasi-1D system captures the essence of multiple pulse trajectories inside complicated 3D scattering systems [63].

The scattering parameter, S_{11}, of this 1-port system (with the port at the driving line) can be analytically determined from the characteristic admittance, the propagation constant, and the terminal reflection coefficient of the lines (see Eq.3.2 and the discussion in Sec.3.4.1). Thus, the response to any time domain input signal can be determined by Fourier transforming the input signal, multiplying it

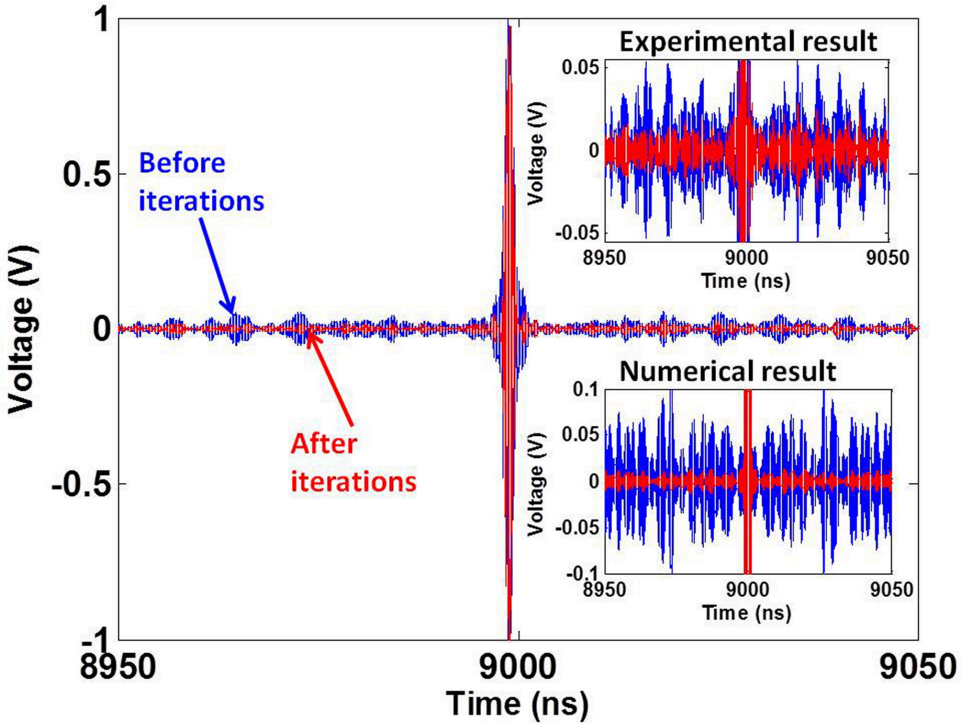

Figure 4.2: The experimental time reversed pulse reconstructed after 25 iterations (i.e. $\mathcal{F}^{-1}[R_{25}]$) using $k = 110$ (red) is overlaid on the pulse reconstructed without the iterative technique (i.e. $\mathcal{F}^{-1}[R_1]$) (blue); the inset on the top right corner shows a close up view of how the sidelobes are suppressed by the iterative technique experimentally. The inset on the bottom right corner shows a close up view of the suppression of the sidelobes after 25 iterations in the noiseless numerical model using $k = 2.5$.

by S_{11}, and inverse Fourier transforming to get the time domain representation of the output signal. Here, the S_{11} is considered as the transfer function H shown in Eq. 4.1.

4.5 Results

4.5.1 Experimental Result

The tunable iterative algorithm was applied to the electromagnetic TR mirror illustrated in Fig. 4.1. A pulse, $\mathcal{F}^{-1}[O]$, with a center frequency of $7GHz$ and a Gaussian envelope of $1ns$ standard deviation was used. In Fig. 4.2, the reconstructed pulse with 1 iteration (i.e. $\mathcal{F}^{-1}[R_1]$ in blue), and after 25 iterations (i.e. $\mathcal{F}^{-1}[R_{25}]$ in red) are compared; the iteration was performed using $k = 110$. The inset at the top right corner of Fig. 4.2 shows a close up view of the resulting sidelobe suppression.

Other iterations were also performed using different values of k. However, only the iterations performed with $k \leq 110$ were expected to converge (i.e. achieve $R_n \to O^*$ as n increases). This is because the H of the 2-port cavity shown in Fig. 4.1 was directly measured, and $\frac{2}{\max(HH^*)} \approx 110$ within the bandwidth of the pulse and the AWGN. All the iterations performed with $k \geq 115$ resulted in a divergence of the iteration. A divergence of the iteration is characterized by the domination of R_n by a single frequency component for large values of n; typically, R_n is dominated by a frequency where HH^* achieved its maximum. In the time domain, the divergence of the iteration corresponds to an increase in the temporal sidelobes of $\mathcal{F}^{-1}[R_n]$ for large values of n.

4.5.2 Comparison with Numerical Result

The simulation was also carried out using a $1ns$ long, $7GHz$ input pulse. The inset at the bottom right corner of Fig. 4.2 shows the corresponding close up view for the result from the star graph model after 25 iterations with $k = 2.5$. This particular simulation did not have AWGN. The scattering parameter, $S_{11} = H$, of the 1-port star graph is accessible from its definition (see Eq.3.2 and the discussion in Sec.3.4.1). For the star graph set up described, $\frac{2}{\max(HH^*)} \approx 2.5$.

Both for the experimental and simulation results, $\mathcal{F}^{-1}[R_n]$ consisted of an approximation of the $1ns$ long pulse and the unwanted $\simeq 10\mu s$ long temporal sidelobes. For each $\mathcal{F}^{-1}[R_n]$, a quantity called the energy ratio, ER_n, was calculated. ER_n is the ratio of the energy of the $1ns$ long pulse within $\mathcal{F}^{-1}[R_n]$ to the temporal sidelobe energy of $\mathcal{F}^{-1}[R_n]$. The temporal sidelobe energy was integrated over the $\simeq 10\mu s$ long sidelobes of $\mathcal{F}^{-1}[R_n]$. ER_n is a figure of merit and quantifies the temporal focusing of the reconstructed time reversed pulse at the n^{th} iteration. The average of this ratio, $< ER_n >_{n=1:100}$, was taken for values of n ranging from $n = 1$ to $n = 100$, for different values of k. This was done on the experimental and simulation data. The test of the iterative TR on the star graph was also run for different noise levels. The noise levels were specified by the standard deviation (σ) of the AWGN (i.e. a_n and b_n noises at each iteration n had the same σ).

A normalized k is defined as $\hat{k} = \max(HH^*)k$. Based on the discussion in Sec. 4.2, $< ER_n >_{n=1:100}$ is expected to be higher for values of $\hat{k} < 2$ than for values of $\hat{k} > 2$. For values of $\hat{k} > 2$, the R_n becomes dominated by a single frequency

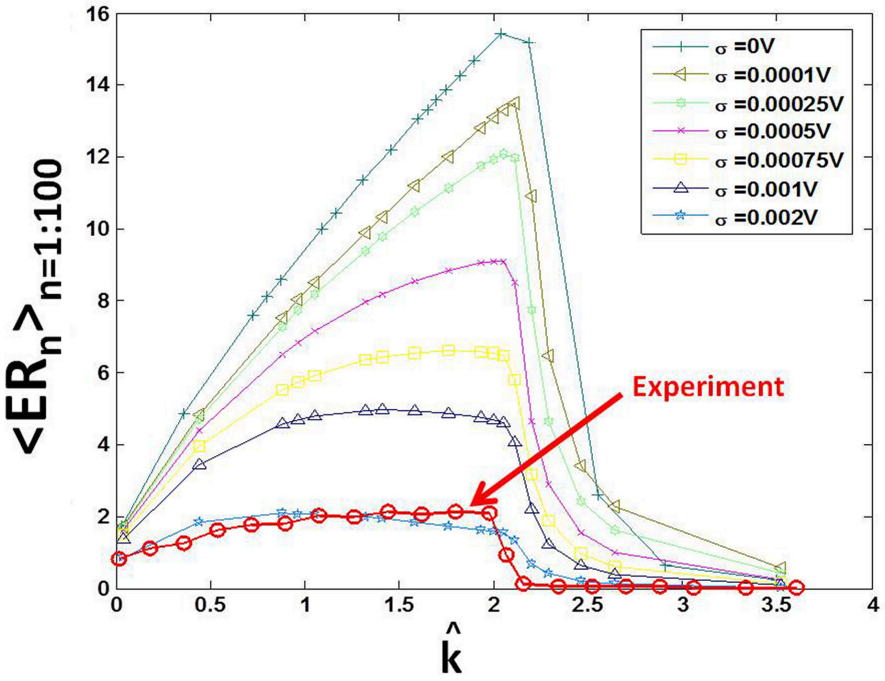

Figure 4.3: The average ratio of the main pulse energy to sidelobe energy (i.e. $< ER_n >_{n=1:100}$) is plotted against normalized k (i.e. $\hat{k}$) for different noise levels that are labeled by the standard deviation (σ) of the AWGN introduced in the numerical model. The average value (i.e. $< ER_n >_{n=1:100}$) was taken over the ratios computed for the first 100 iterations. In addition, similar data from the experiment (shown in Fig. 4.1) is plotted as red circles. The k value is normalized by multiplying it by the maximum of HH^* (magnitude square of the transfer function) of the system over the bandwidth of the pulse and the noise after filtering.

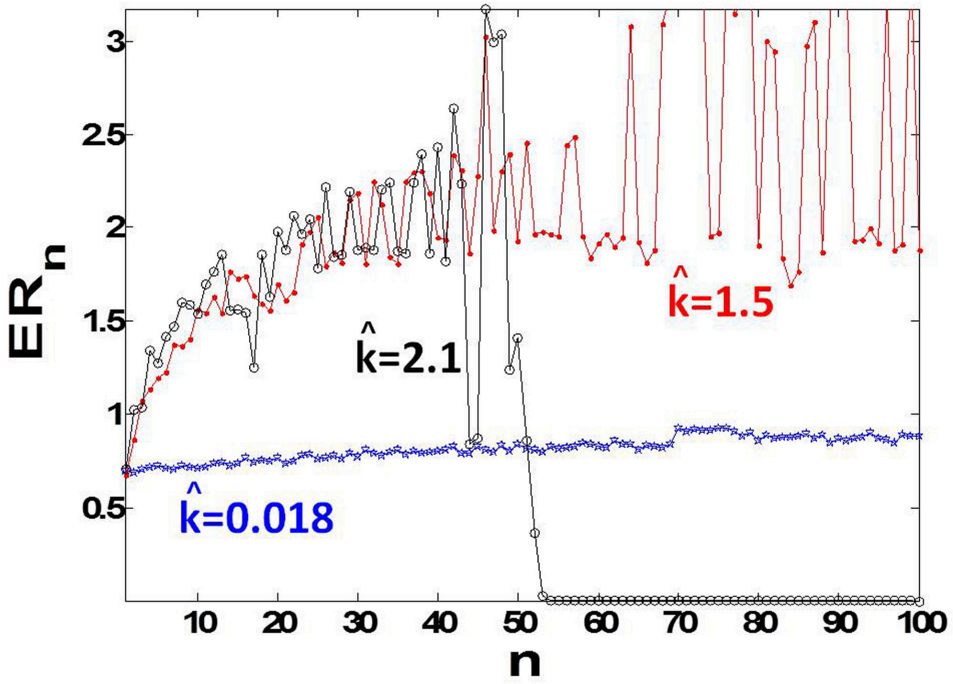

Figure 4.4: The improvement of ER_n is shown as a function of n for exemplar $\hat{k}$ values used in the experiment. For values of $\hat{k} > 2$, the iteration is expected to diverge eventually. The convergence of the iteration can be tuned using $\hat{k}$ (equivalently. k).

component for large n values; therefore, the $< ER_n >_{n=1:100}$ is expected to be lower for values of $\hat{k} > 2$.

Fig. 4.3 shows the $< ER_n >_{n=1:100}$ versus $\hat{k}$ for simulations run with different noise levels, and for the experiment. The experimental result shows very clear similarity to the simulation results. Fig. 4.4 shows ER_n versus n for the experimental data at selected values of $\hat{k}$. For example, at $\hat{k} = 2.1$, the ER_n steadily improves until about $n = 45$, and it crashes as R_n starts to get dominated by a single frequency component. Fig. 4.4 illustrates that the convergence of the iterative TR can be tuned using k.

Fig. 4.3 also demonstrates that the optimum k is roughly $\frac{2}{\max(HH^*)}$. The tunable iterative TR performed best for $\hat{k} \approx 2$, both for the simulation with different noise levels, and the experiment. This is in agreement with the convergence condition for Eq. 4.1 as discussed in Sec. 4.2.

4.6 Discussion

4.6.1 Overcoming Dynamic Range Limitations

Despite the elegance of the discussion leading to Eq. 4.1, there were some experimental challenges in realizing the tunable iterative TR algorithm. In this section, the technique that is used to overcome the experimental challenge is discussed.

As shown in Fig. 4.1, an arbitrary waveform generator (AWG) was used in conjunction with a microwave source to realize the TR mirror operation. There was a limited dynamic range (i.e. 8 bits) offered by the AWG to represent signals. This made generating $\mathcal{F}^{-1}[(R_n - O^*)^*]$ using the AWG and recording the appropriate $\mathcal{F}^{-1}[C_n]$ using the oscilloscope a challenge because, in a very lossy or poorly coupled systems, $HH^* \ll 1$ for most frequency values. The cavity shown in Fig. 4.1 was an example of a poorly coupled system due to the radiation characteristics of the monopole antennas used. Therefore, $|R_n|^2 \ll |OO|^2$ for most frequency values in these systems. Consequently, $\mathcal{F}^{-1}[(R_n - O^*)^*]$ is approximately equal to $\mathcal{F}^{-1}[-O]$ in these systems. When we attempt to generate $\mathcal{F}^{-1}[(R_n - O^*)^*] \approx \mathcal{F}^{-1}[-O]$ using the AWG, it essentially generates just $\mathcal{F}^{-1}[-O]$ due to the limited dynamic range of the equipment.

Based on the derivation in Sec. 4.2, if $(R_n - O^*)^*$ is reduced to $-O$ due to the limited dynamic range of the instrumentation, then C_n (which is defined as $C_n = H(R_n - O^*)^* k + b_n$) reduces to $-HOk + b_n = -S_1 k + b_n$. Consequently, the sona update equation, which is $S_{n+1} = S_n - C_n$, reduces to $S_{n+1} = S_n + S_1 k - b_n$. This makes the iterative TR algorithm ineffective because, the sona does not change as the iteration progresses, other than picking up AWGN.

This experimental problem was overcome by introducing a single amplitude scaling factor, Ω_n, which is dynamically determined at each iteration n. Ω_n is determined from the ratio of the maximum amplitudes of $\mathcal{F}^{-1}[R_n]$ and $\mathcal{F}^{-1}[O^*]$. Then instead of $\mathcal{F}^{-1}[(R_n - O^*)^*]$, the AWG is programmed to generate $\mathcal{F}^{-1}[(R_n - \Omega_n O^*)^*]$, which has a smaller dynamic range.

Ω_n is a real number smaller than 1. Hence, the generated $\mathcal{F}^{-1}[(R_n - \Omega_n O^*)^*]$ is lacking some information about O^* (specifically $(1 - \Omega_n)O^*$). Consequently, C_n (which is $H(R_n - \Omega_n O^*)^* k + b_n$) is lacking $(1 - \Omega_n)HO$. So, the sona update equation ($S_{n+1} = S_n - C_n$) needs to be amended before the iteration continues. Otherwise, S_{n+1} losses some information about $(1 - \Omega_n)HO$ as well. The amended sona update equation is $S_{n+1} = S_n - C_n + (1 - \Omega_n)HO = S_n - C_n + (1 - \Omega_n)S_1$.

To summarize, the limited dynamic range of the AWG was overcome by introducing a dynamically determined scaling constant Ω_n at each iteration. This resulted in the generation of the low dynamic range signal, $\mathcal{F}^{-1}[(R_n - \Omega_n O^*)^*]$, by the AWG instead of $\mathcal{F}^{-1}[(R_n - O^*)^*]$, which has a high dynamic range. To compensate for the adverse effects of this modification to the algorithm, the sona update equation is amended to be $S_{n+1} = S_n - C_n + (1 - \Omega_n)S_1$. Despite these internal

changes to the algorithm, there is no change on the structure of Eq. 4.1. The experimental results were obtained using this technique to overcome the limited dynamic range of the AWG.

4.6.2 Potential Applications

The main goal of the iterative TR is to improve the spatiotemporal focusing of the reconstructed pulse. The iterative technique can be useful in applications where TR mirrors have already been employed, but could benefit from an enhanced focusing. The tunable iterative technique introduced in this chapter is advantageous because it can speed up the convergence of the iteration.

Here is a description of a scenario where the tunable iterative TR can be applied. Suppose that there are two points in space labeled A and B. There is a capability to transmit and record waves at point A, and there is only access to record waves at point B. The regular TR mirror broadcasts a pulse from point A and records the sona at point B. Then, it broadcasts the time reversed sona from point A, and it records the reconstructed time reversed pulse at point B (taking advantage of spatial reciprocity). Finally, the spatiotemporal focusing of the reconstructed pulse can be improved using the iterative TR.

The scenario becomes even more interesting if the access to record waves at point B expires. For example the recording device that was covertly placed at point B could run out of battery-supplied energy. In this special scenario, the tunability of the iterative TR is an advantage. Because, the optimum sona that can

achieve sharp spatiotemporal focusing at point B can be synthesized using as few iterations as possible. There is even a possibility of remotely scanning the recording device to neighboring points of B, and quickly synthesizing optimum sonas that can achieve focusing at any selected nearby point. Clearly, the capability to speed up the convergence of the regular iterative TR is a practical advantage.

An example of a real world application that is based on the scenario described above is the realization of virtual sources in geophysics [35, 36]. Continuing with the discussion above, the reconstructed pulse at point B diverges out after it spatiotemporally focuses on B. This effectively makes point B a virtual source of waves. In geophysics, TR mirrors have been used to realize virtual sources which image geological formations beyond a seismically opaque geological stratum [35]. If the tunable iterative TR technique is applied, the virtual sources may be better localized in space. Finally, the tunable iterative TR can also be useful to enhance spatially focused, peak field generation inside reverberation chambers [65].

4.7 Conclusion

The iterative time reversal technique was demonstrated experimentally using electromagnetic waves in a microwave wave chaotic cavity, and by using a simulation of a star graph. A new amplification parameter is introduced into the iterative algorithm to control the rate of convergence of the iteration. The optimum value of this parameter is dictated by the scattering properties of the system over the bandwidth of the pulse and the noise.

Chapter 5

Mitigating the Effect of Non-Uniform Loss on Time Reversal Mirrors Using Exponential Amplification

In Chapter 4, the tunable iterative technique was introduced. The technique overcomes the adverse effect of dissipation on the real-time spatiotemporal wave focusing of time reversal mirrors. The focusing was quantified in Sec. 4.5.1 using the ratio of pulse to temporal sidelobe energy. In this Chapter, we are less interested in achieving a real-time spatiotemporal wave focusing using time reversal mirrors. Instead, we are mainly interested in the capability to easily identify the reconstructed time reversed pulse after it is digitized. The ability to precisely identify the reconstructed pulse after digitization may be important in applications such as communication.

Here, the performance of time-reversal mirrors is quantitatively defined as the correlation between the original pulse and the time reversed version of the reconstructed pulse. The adverse effect of dissipation on this performance of time-reversal mirrors is investigated. The technique of exponential amplification is proposed to overcome the effect of dissipation in the case of uniform loss distributions, and, to some extent, in the case of non-uniform loss distributions. A numerical model of a star graph was employed to test the applicability of this technique on realizations of the star graph with various spatial distributions of loss. The numerical results are

also verified by an experimental result from an electromagnetic time-reversal mirror.

5.1 Introduction

Time reversal (TR) mirrors can, under ideal circumstances, precisely reconstruct a wave disturbance which happened at an earlier time, at any given later time. TR mirrors have found numerous applications since the earliest experimental demonstrations of TR using acoustic waves [21]. More recently, TR mirrors have been realized using electromagnetic waves [23, 25] expanding their applicability. TR mirrors have applications in communications [48, 49], imaging [45, 44], source localization [36], non-destructive evaluation [32, 33], and sensing [18, 20, 25]. In applications such as communications, it may be vital that the reconstruction of the wave disturbance (before or after numerically processing) is of high quality. In this chapter, we will see how this can be achieved despite the presence of inhomogeneous loss in the system.

TR mirrors are used to focus waves both in space and time. An ideal TR mirror consists of a wave source located inside a lossless medium that is completely enclosed by a surface of transceivers. A TR mirror operates in two steps. In step one, the transceivers record and absorb the signal broadcast by the source. In step two, the transceivers rebroadcast time reversed versions of the recorded waves. The waves broadcast in step two eventually focus on the location of the source and reconstruct a time reversed version of the original signal, which was broadcast in step one: this is possible because of the TR invariance property of the lossless wave

equation. This ideal TR mirror uses the so called closed TR cavity [66]. However, it is not generally practical, for example, to build a closed TR cavity, whose interior is completely covered with transceivers. Therefore, practical TR mirrors have several limitations, which result in an imperfect reconstruction of the original signal. These limitations include i) limited spatial coverage by the transceivers, and ii) dissipation during the wave propagation (which breaks TR invariance of the wave equation) [26, 18].

The first limitation of TR mirrors can be overcome by the use of a reflecting wave chaotic cavity with partial spatial coverage and transceivers that have a long recording time [26, 18]. However, the limitation due to dissipation persists, and leads to increasing loss of information as the recording time increases.

As described in Chapter 4, the technique of iterative TR was proposed to improve the performance of TR mirrors, which suffer from the limitations of dissipation and incomplete spatial coverage of transceivers [27]. However, the iterative technique may not converge fast enough, despite a recent result showing the tunability of its convergence [30]. The faster alternative to the iterative technique is the inverse filter technique [28, 27], which was introduced in Sec. 4.2. But, the inverse filter technique is computationally costly and potentially unstable [27].

In Chapter 2, the technique of exponential amplification was initially used to overcome an adverse effect of dissipation. Specifically, the spatial range of the TR sensing techniques was limited due to dissipation. The exponential amplification technique was used to extend the spatial range of the sensing techniques [18, 20].

In this Chapter, yet another application of the exponential amplification tech-

nique is proposed. The application involves improving the performance of TR mirrors, which suffer from dissipation. The performance of TR mirrors is defined as the normalized correlation between the original pulse and the time reversed version of the reconstructed pulse. The technique of exponential amplification can compete with the iterative TR technique in improving this performance of TR mirrors, to some extent. The relative advantage of the exponential amplification technique is that it is faster to implement, as it does not rely on iterative steps. It is also cheaper computationally.

In Sec. 5.2, the theory supporting the exponential amplification technique, which is first discussed in Sec. 2.2, is summarized. The performance of TR mirrors is also defined in Sec. 5.2. In Sec. 5.3, the exponential amplification technique was used to improve the performance of an electromagnetic TR mirror. Particularly, it is shown that the technique can improve the performance of a TR mirror for the case of uniform spatial loss distribution. Above and beyond the uniform loss case, Sec. 5.4 investigates the limits of applicability of the exponential amplification in systems with inhomogeneous loss distributions. The investigation was carried out using a numerical model of the star graph, which is introduced in Sec. 3.4.1. Sec. 5.5 provides a conclusion.

5.2 Theory

Sec. 2.2 first introduced the theory supporting the exponential amplification technique. To summarize, a cavity with transfer function $\hat{s}(\omega)$ was considered.

When a brief pulse, $a(t)$, is broadcast into the cavity, the response is $b(t)$. In the frequency domain, these signals obey $\hat{b}(\omega) = \hat{s}(\omega)\hat{a}(\omega)$. A time reversed version of $b(t)$ is denoted as $c(t)$ in this section. When $c(t)$ is broadcast back into the cavity, a reconstructed pulse is obtained which is denoted as $d(t)$. Sec. 2.2 provides a derivation supporting the following results. If the cavity is lossless, $a(t)$ is the same as a time reversed version of $d(t)$ which is denoted here as $e(t)$. Thus, the TR mirror works perfectly in a lossless cavity.

Even if the cavity is lossy, it is shown that the TR mirror can be perfected assuming uniform loss. Suppose that the uniform loss is represented by a $1/e$ voltage decay time (i.e. τ). In this case, the signal $b(t)$ is exponentially amplified by $e^{2t/\tau}$, time reversed, and broadcast back into the cavity. $\tilde{c}(t)$ denotes the signal obtained after exponentially amplifying $b(t)$, and time reversing it. Similarly, $\tilde{d}(t)$ denotes the reconstructed pulse obtained when $\tilde{c}(t)$ is broadcast back into the cavity. The time reversed version of $\tilde{d}(t)$ is denoted by $\tilde{e}(t)$. Sec. 2.2 analytically predicts $\tilde{e}(t)e^{-2t/\tau}$ which is equal to $a(t)$ for a uniform loss that is characterized by τ.

Here, we define a new signal ($\hat{e}(t)$) that can be synthesized from $\tilde{e}(t)$. $\hat{e}(t)$ is called the corrected reconstructed pulse. $\hat{e}(t)$ is obtained by multiplying $\tilde{e}(t)$ by $e^{-2t/\tau}$. In this Chapter, the performance (η) of the TR mirror is defined based on the normalized correlation between the corrected reconstructed pulse ($\hat{e}(t)$), and the original pulse ($a(t)$).

$$\eta = \frac{\sum_{t=0}^{t=T} a(t)\hat{e}(t)}{\sqrt{\sum_{t=0}^{t=T} a(t)^2 \sum_{t=0}^{t=T} \hat{e}(t)^2}} \tag{5.1}$$

Each of the signals $a(t)$ and $\hat{e}(t)$ have a duration of T. The two signals are assumed

to be perfectly aligned to maximize η. Based on the result from Sec. 2.2, $a(t) = \hat{e}(t)$ if the system is uniformly lossy with a $1/e$ voltage decay time, τ. Therefore, the performance of the TR mirror is expected to be perfect (i.e. $\eta = 1$) based on this analysis of the application of the exponential amplification technique. However, the analysis does not model the effect of noise and limited dynamic range on the exponential amplification technique.

If the exponential amplification is not applied to $b(t)$, the performance, η, can still be calculated using the signals $a(t)$ and $e(t)$, instead of using $a(t)$ and $\hat{e}(t)$. But, if the system is lossy, and exponential amplification is not applied, then it is not expected that $\eta = 1$.

In Sec. 5.3, this theory, which assumes uniform loss distribution, is successfully tested in an experimental system that approximates the case of uniform loss distribution. However, it is also expected that the theory applies for the case of moderately non-uniform loss distribution. The applicability of the exponential amplification technique to mitigate the effect of non-uniform loss is studied in Sec. 5.4.

5.3 Overcoming the Effect of Spatially Uniform Loss: Experimental Test

The electromagnetic TR mirror involves a one cubic meter aluminum box that has scatterers inside it, and two ports. The experimental TR mirror operates as shown in Fig. 5.1. The original pulse was broadcast into the cavity using port 1, and the response signal, which we call "sona", was collected using port 2. The

original pulse had a carrier frequency of $7GHz$ and a Gaussian envelope with a standard deviation of $1ns$. The sona was recorded for about $6.5\mu s$ with a signal to noise ratio (SNR) greater than 1. During the second step of the TR mirror operation, the sona signal was time reversed and broadcast back into the cavity using port 1; this made use of the spatial reciprocity property of the wave equation [18]. Finally, a reconstructed pulse, which approximates a time reversed version of the original pulse was collected at port 2. The reconstructed pulse (and its temporal sidelobes) was collected over a $10\mu s$ duration. The first $6.5\mu s$ included a direct recording of the time reversed sona being injected into the cavity. The last $3.5\mu s$ was a recording of the reconstructed pulse diverging out from port 2, and reverberating throughout the cavity.

Based on Eq. 5.1, η can be calculated as the normalized correlation between the following two aligned signals: i) the time reversed version of the reconstructed pulse with its temporal sidelobes (which was a $10\mu s$ long recording), and ii) the original pulse broadcast (by considering the $1ns$ long Gaussian envelope to be located at $t = 3.5\mu s$ of a $10\mu s$ long signal of nearly zero voltage values). Note that these two signals are equivalent to the aligned $a(t)$ and $e(t)$ signals introduced in Sec. 5.2. If the TR mirror were perfect, η would be 1. However, as can be seen in part 4 of Fig. 5.1, the reconstructed pulse has temporal sidelobes which result in $\eta < 1$. The sidelobes arise due to the limitations of practical TR mirrors discussed in Sec. 5.1, which include limited spatial coverage of transceivers and dissipation.

Generally, the sona signal shows an exponential decay which is caused by dissipation and coupling. The experimental system discussed here is strongly under-

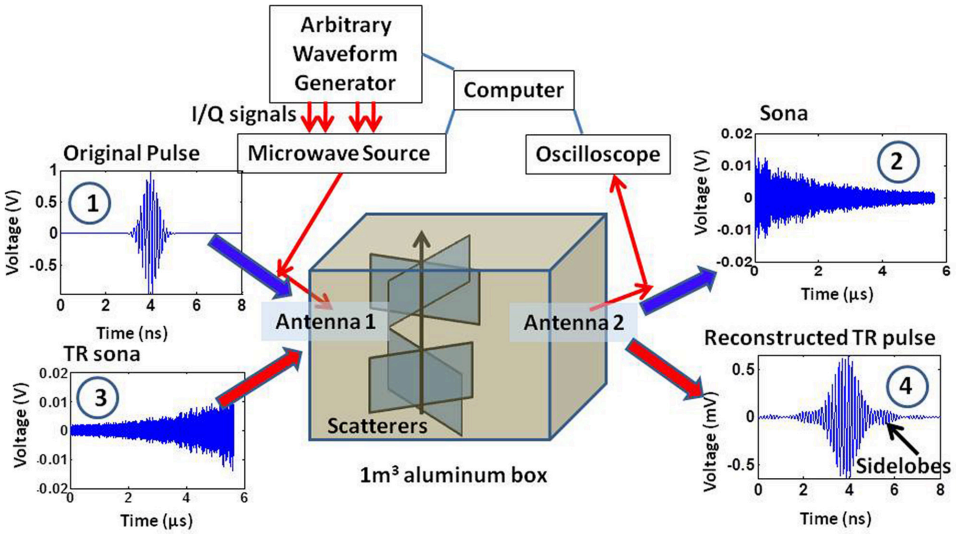

Figure 5.1: Schematic of the electromagnetic time reversal (TR) mirror experiment, without exponential amplification. During step 1 of the TR mirror, the original pulse is broadcast through antenna 1 (as shown in part 1), and the resulting sona is collected at antenna 2 (as shown in part 2). During step 2 of the TR mirror, the time reversed sona is injected into the system at antenna 1 (as shown in part 3) to retrieve the reconstructed time reversed pulse at antenna 2 using spatial reciprocity (as shown in part 4). Experimental data are shown for each step.

coupled [11], which means that the effect of dissipation dominates the effect of coupling. Therefore, the $1/e$ voltage decay constant (τ) which is related to the unloaded quality factor can be readily determined by a line fit to the *log* of the sona energy as a function of time. The exponential amplification can then be applied to the sona signal before it is time reversed and broadcast into the cavity. The exponential amplification is carried out by multiplying the sona signal by the time dependent amplifying function

$$A(t, F) = exp(\frac{Ft}{\tau}) \tag{5.2}$$

where t is time in seconds, and F is a fudge factor. Assuming a precise determination of τ, using $F = 1$ compensates only for the effect of dissipation on the sona during step 1 of the TR mirror operation; whereas, using $F = 2$ compensates for the effect of dissipation on the sona during both step 1 and step 2 of the TR mirror operation [20]. The theoretical discussion in Sec. 5.2 predicts that $F = 2$ to maximize η. The exponential amplification is applied to the part of the sona whose signal to noise ratio is, at the very least, greater than 1 (i.e. the $6.5\mu s$ long sona in this experiment). Besides, the function $A(t, F)$ is typically terminated by a smooth ramp down function whose time span is at least as wide as the time duration of the original pulse, which is $1ns$; this prevents additional frequency components from entering into the sona.

Suppose that the sona is exponentially amplified using $A(t, F)$, before it is time reversed and broadcast into the electromagnetic cavity. The reconstructed pulse obtained with $F > 0$ sona amplification will have more sidelobes than the re-

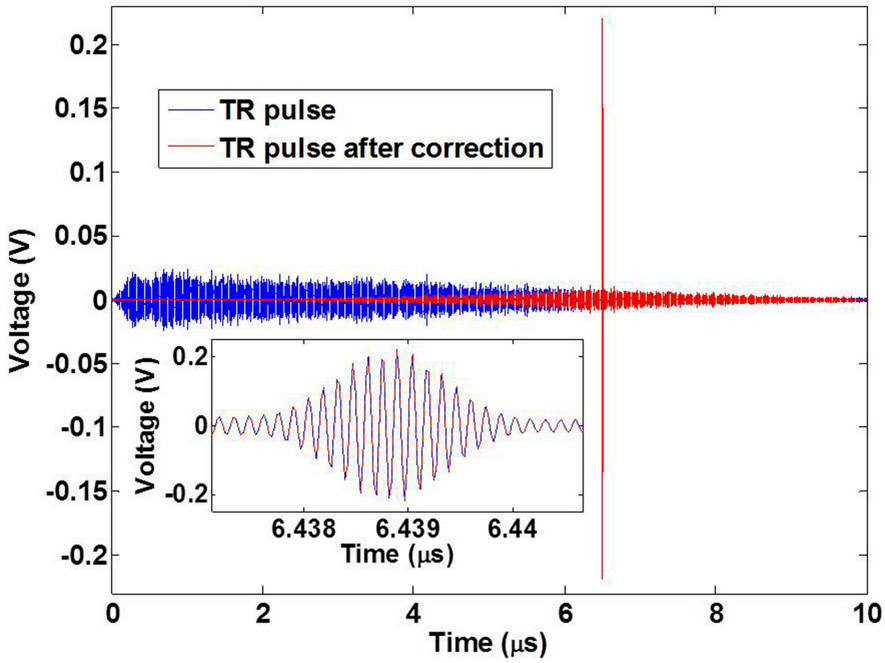

Figure 5.2: The reconstructed TR pulse obtained from a sona that was exponentially amplified with $F = 2$ (blue) had significant sidelobes. The corrected reconstructed pulse (red) was obtained by multiplying the time reversed version of the reconstructed TR pulse by $A(t - 3.5\mu s, F = -2)$. The corrected reconstructed pulse is displayed here after time reversing it. $A(t, F) = 1$ if $t < 0$. The inset shows a close up of the reconstructed pulses, which are the same before and after the correction.

constructed pulse obtained with $F = 0$ sona amplification. However, these sidelobes can be numerically suppressed by manipulating the reconstructed waveform, which is digitized, as follows. For example, Fig. 5.2 shows the reconstructed waveform obtained using sona that is amplified with $A(t, F = 2)$ (in blue); the reconstructed waveform has unwanted temporal sidelobes which are a result of the exponential amplification applied to the sona. These sidelobes were corrected as follows. The $10\mu s$ long reconstructed waveform was time reversed so that the $1ns$ long Gaussian pulse is located at about $t = 3.5\mu s$; this waveform was then multiplied by $A(t - 3.5\mu s, F = -2)$ to get the corrected reconstructed waveform (i.e. $\hat{e}(t)$) introduced in Sec. 5.2. $A(t, F) = 1$ for $t < 0$ by convention. In Fig. 5.2, the corrected reconstructed waveform is time reversed and plotted (in red) to highlight its relationship with the reconstructed waveform. The corrected reconstructed waveform is expected to have a better normalized correlation with the original pulse because of the exponential amplification with $F = 2$, as predicted in Sec. 5.2.

Several values of F were used to carry out the operation of the TR mirror assisted by exponential amplification. For each F value, the performance of the electromagnetic TR mirror, η, is shown in Fig. 5.3. It is shown that the performance of the TR mirror is enhanced by using exponential amplification with $F \approx 2$ for a good determination of τ of the sona; particularly, η increases from $\approx 63\%$ at $F = 0$ to $\approx 73\%$ at $F = 2$. This result agrees with the theoretical prediction in Sec. 5.2. The fact that the $\eta < 1$ even for $F \approx 2$ can be explained by the fact that the TR mirror only has one recording channel, whereas the theory assumes that all the waves are captured. Thus, the exponential amplification technique only overcomes

the limitation of TR mirror emanating from dissipation, and not the problem of insufficient spatial coverage of recorders. The noise, which is not considered in the theory, also affects the performance of TR mirrors as it was seen in Sec. 4.5.2.

As shown in Fig. 5.3, the exponential amplification achieves η that is as high as 73% for the experimental set up described. This compares with $\eta \approx 78\%$ which is achieved by the tunable iterative technique of Chapter 4 on the same experimental set up described in Sec. 4.3. Therefore, the iterative technique performs better than the exponential amplification technique when both of them use their respective optimum parameters. Nonetheless, the exponential amplification has an advantage because of its speed, and computational simplicity.

The result in this section proves that the exponential amplification improves the performance, η, of TR mirrors with uniform spatial loss. The one cubic meter aluminum cavity has a homogenous material make up, and can be assumed to have a uniform spatial distribution of loss.

5.4 Overcoming the Effect of Spatially Non-Uniform Loss: Numerical Test

The exponential amplification technique is derived assuming uniform loss distribution. The case of non-uniform loss distribution is better handled with techniques such as the inverse filter, and the iterative TR [28, 27], which do not assume uniformity of loss. However, it is expected that the exponential amplification can be applied in cavities with moderately inhomogeneous loss distributions. The applica-

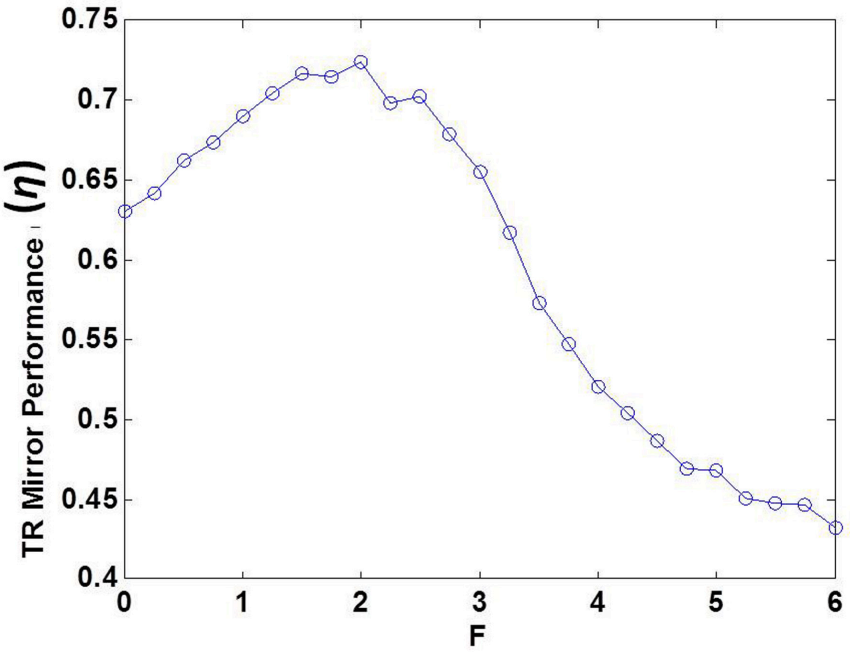

Figure 5.3: The performance (η) of the electromagnetic TR mirror as a function of F parameter used to exponentially amplify the sona signal. The optimum value of the fudge factor, F, is around $F = 2$ as expected for a precise determination of τ of the sona.

bility of the exponential amplification technique was studied as the inhomogeneity of the spatial distribution of loss was increased. The simulations in this section were designed to supplement the experimental results in Sec.5.3.

5.4.1 Simulation Setup

The numerical model is based on the star graph, which is introduced in Sec. 3.4.1. It is a quasi-1D chaotic system which consists of a driving transmission line that feeds a number of transmission lines, which are all connected to each other in parallel. It is a one port system. Thus, the original pulse is injected through the driving transmission line, and the sona is also collected from the same line. The original pulse has the same characteristics as the one used in the experiment described in Sec. 5.3.

There are 500 transmission lines in the star graph set up. Their length is given by $L_i = \sqrt{i}\ m$ for i ranging from 1 to 500. The driving line has a length of 0 m. The characteristic admittances of the 500 lines are $Y_{ci} = 1S$. The driving line has a characteristic admittance of $Y_{cd} = \sum_{i=1}^{i=500} Y_{ci} = 500S$; this set up eliminates prompt reflection of signals injected through the driving line. The terminal reflection coefficients, Γ_i, of the 500 lines are all set to 1. The dissipation is introduced through the frequency dependent propagation constant of the lines, $\gamma_i(\omega) = \imath\frac{\omega}{c} + \alpha_i$, where c is the speed of light and α_i is the loss constant of line i.

α_i specifies that the voltage waves decay on line i as $e^{-\alpha_i z}$, where z is distance measured along line i in meters. The spatial inhomogeneity of loss on the star graph

is modeled as follows. The α_i of each of the 500 lines is randomly chosen from the probability density function (pdf).

$$p_{n,\lambda}(\alpha) = \frac{\alpha^n}{\lambda^{n+1} n!} exp(-\alpha/\lambda) \tag{5.3}$$

The pdf has two parameters, n and λ, which define the mean ($\mu_\alpha = \lambda + \lambda n$) and standard deviation ($\sigma_\alpha = \sqrt{\lambda(\lambda + \lambda n)}$) of α values. This particular pdf is chosen for the following two reasons. First, the coefficient of variation ($R = \sigma_\alpha/\mu_\alpha$) can be easily varied while keeping μ_α constant. Keeping the average spatial loss constant simplifies the problem, and helps us focus on the effect of increasing spatial loss inhomogeneity. Besides, the main motivation for using the exponential amplification in the case of non-uniform loss is: if the $1/e$ decay constants (i.e. τ) of the different modes are not extremely different, we can use a single average τ value. Thus, it is not interesting to vary the average loss (effectively τ) here. In this set up μ_α is chosen as $\frac{1}{c\tau}$, where $\tau = 1.5\mu s$. The second reason to use this particular pdf is that its support is the set of positive numbers, which should be the case as α should always be positive on the transmission lines. Fig. 5.4 shows plots of the pdf for different values of R, where $\mu_\alpha \approx 0.002$.

The numerical values of the parameters of the star graph were chosen to achieve the following objective. The experimental result in Sec. 5.3 was based on an under-coupled cavity. An under-coupled cavity is characterized by the domination of energy loss due to dissipation over energy loss due to coupling [11]. If the cavity is not under-coupled, the advantage of the exponential amplification technique cannot be easily seen because there are no strong internal dissipation effects to be compensated

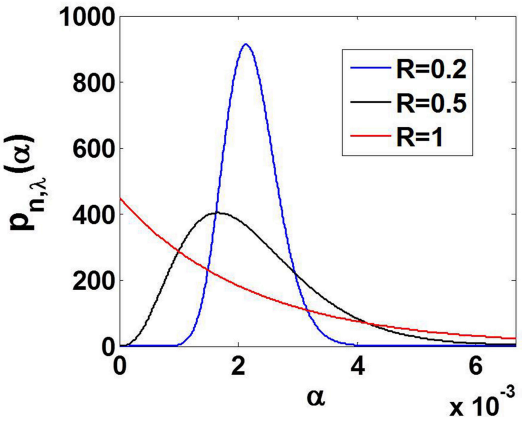

Figure 5.4: The probability density function (pdf) in Eq. 5.3 is plotted for different $R = \sigma_\alpha/\mu_\alpha$ values where $\mu_\alpha \approx 0.002$. R is a measure of loss inhomogeneity. The pdf is plotted for $R = 0.2$ (blue), $R = 0.5$ (black), and $R = 1$ (red).

in an over-coupled cavity. Thus, the star graph was set up to create an under-coupled cavity, where we can clearly see the advantage of the exponential amplification. To accomplish under-coupling, 500 lines were used in the star graph to increase the back-reflection coefficient of the waves that are trying to leave the star graph. This forces the waves to reverberate inside the star graph for longer, which decreases the coupling loss by two orders of magnitude compared to the dissipation loss.

5.4.2 Simulation Results

A TR mirror was implemented on the star graph by broadcasting the original pulse, collecting a sona, exponentially amplifying the sona with $A(t, F)$, time reversing the amplified sona, and broadcasting it back into the star graph. The reconstructed pulse was collected, and it was time reversed and multiplied by $A(t-x, -F)$.

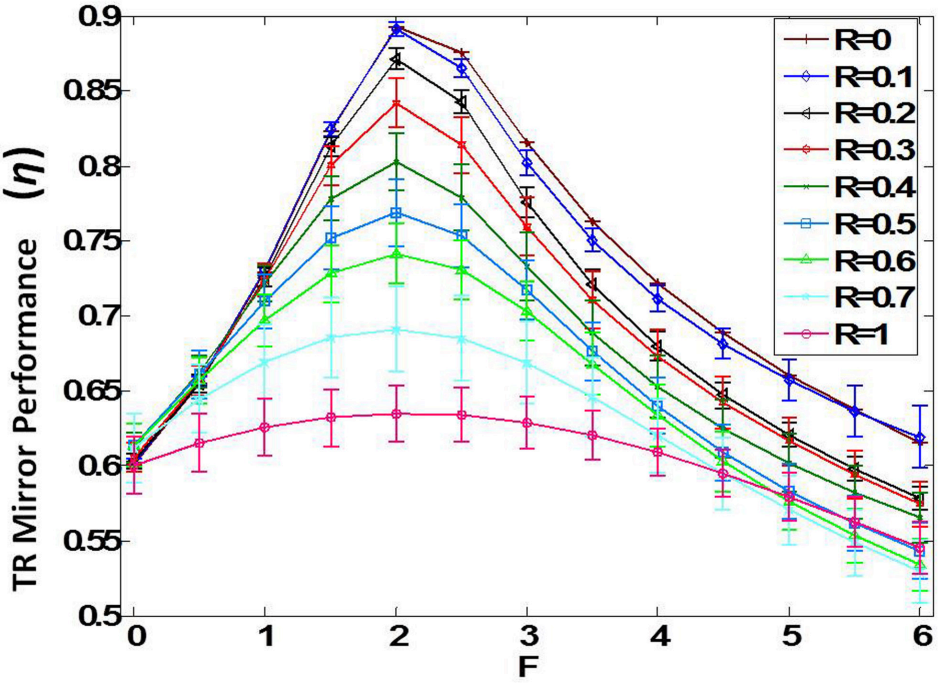

Figure 5.5: The performance (i.e. η) of the TR mirror in a star graph as a function of F parameter for various degrees of loss inhomogeneities characterized by R. Loss inhomogeneity increases with R. The optimum F value is always around $F = 2$ for the τ value that is well determined from the sona.

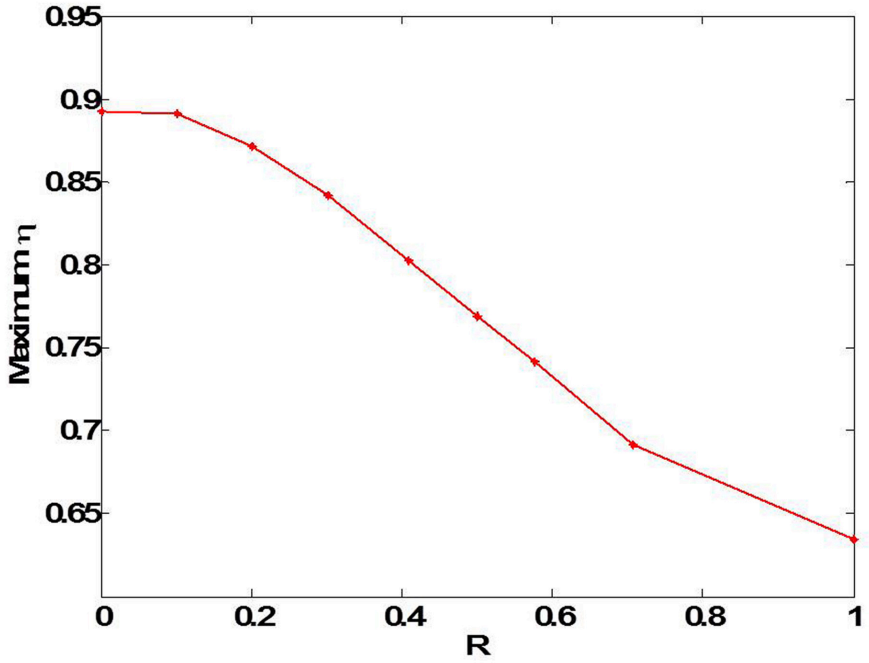

Figure 5.6: The maximum performance of the TR mirror in a star graph as a function of R. The maximum η is taken over all F values tried between 0 and 6 as shown in Fig. 5.5. R is the coefficient of variation of the loss, which increases with the loss inhomogeneity.

Here, x is the time when the $1ns$ Gaussian pulse was expected within the time reversed version of the reconstructed waveform. The signals were collected over a span of $10\mu s$ without noise.

The performance (η) of the TR mirror is plotted versus F as shown in Fig. 5.5. This entire process was repeated for star graphs with different degree of loss inhomogeneity characterized by R. $R = 0$ represents uniform spatial loss distribution. As R increases, the loss inhomogeneity increases. For each R value, 25 realizations of the star graph were generated; so, there are error bars included on the η vs F plots for each R value, as shown in Fig. 5.5.

For each R value shown in Fig. 5.5, the maximum η was taken over all F values attempted. The maximum η achieved is plotted as a function of the loss inhomogeneity (R) in Fig. 5.6. Fig. 5.6 demonstrates that the exponential amplification technique achieves a high performance, η, for small values of R, which are close to uniform loss distributions. The exponential amplification is still applicable in cavities with more inhomogeneous loss distributions. However, its effectiveness declines with increasing loss inhomogeneity as expected.

5.5 Conclusion

The exponential amplification improves the performance of time reversal mirrors best if the loss is uniformly distributed in space. However, even under conditions in which the loss is not uniformly distributed, the exponential amplification mitigates the adverse effect of non-uniform loss on the performance of time reversal mirrors. This technique may be advantageous to use in time reversal mirror based communication applications because even if the reconstructed pulse will have more sidelobes during the recording, the processed reconstructed pulse will closely replicate the shape of the original pulse.

Chapter 6

Conclusion and Future Directions

6.1 Final Conclusions

This dissertation has achieved two major milestones. These are: i) the development of novel wave-based sensors with minimal false negatives and comprehensive spatial coverage [18, 19, 20], and ii) the enhancement of the spatiotemporal wave focusing of time reversal mirrors [30]. The sensing techniques developed in Chapters 2 and 3 have the potential to be successfully utilized in real world applications. This potential is demonstrated by the rigorous experimental tests presented in this dissertation. The tunable iterative time reversal technique, which is presented in Chapter 4, has the potential to be integrated into existing applications of time reversal mirrors in various fields. The exponential amplification technique, which is discussed in Chapter 5, initiates a new perspective to improve time reversal mirrors which suffer from dissipation. Overall, this dissertation establishes the ground work to study a plethora of fascinating research problems. Some of the research problems that can be studied as an extension of this dissertation are outlined in Sec. 6.2

6.2 Future Work

6.2.1 Types of Perturbations that can be Detected

The sensors that are developed in Chapter 2 are extremely sensitive by nature. In principle, they can detect various kinds of small perturbations to the cavity. It is interesting to quantitatively establish the limits of sensitivity of these sensors for different classes of perturbations. For instance, in Sec. 3.3.3, the smallest measurable VCSPP was formulated. It is shown that a VCSPP that is induced by walls of the cavity moving over a sub-wavelength distance (Δx) can be detected, where $\frac{\Delta x}{\lambda} \approx 3 * 10^{-4}$. In a similar spirit, the possibility of detecting other classes of perturbations that have a sub-wavelength size can be investigated using the following two approaches.

6.2.1.1 Use of Evanescent Waves to Detect a Sub-Wavelength Perturbation

The work on time reversed focusing that beats the diffraction limit [39] inspires the possibility of designing a sensor that can detect sub-wavelength perturbations. The idea relies on the theoretical possibility of conversion between propagating and evanescent modes in a time reversal experiment [40]. The experimental set up to accomplish surveillance of the movement of a sub-wavelength "target object" is illustrated in Fig. 6.1(a). The ray chaotic enclosure contains the wave source element and the time reversal mirror. The evanescent-wave "generator" shown in the

illustration could for example be a bundle of thin copper wires, which have proven to allow conversion of evanescent waves to propagating waves and vice versa [39]. During the time-forward operation of the time reversal mirror, propagating waves get converted to evanescent waves and back again to propagating waves by the duo of the evanescent-wave "generator" and the target object (see Fig. 6.1(b)). The evanescent waves fall off exponentially in space, hence a small change in position of the target object will have a big influence on the evanescent-to-propagating conversion process. If the target object does not move before the time-reversed operation of the time reversal mirror (see Fig. 6.1(c)), a perfectly time reversed version of what happened in the first step should occur. Otherwise, we expect the change of position of the target object with respect to the evanescent wave generator to be detectable.

Possible problems with this scheme include the lack of sensitivity to such a small change. Therefore, the general idea may have to be first tested by placing both the evanescent wave "generator" and the target object near the source antenna. This will guarantee that almost all the ray trajectories, which pass through the vicinity of the source, will experience the effect of the changed evanescent-to-propagating conversion process.

This idea of detecting sub-wavelength perturbations using evanescent-propagating mode conversion can be investigated using different platforms. A High Frequency Simulation Software (HFSS) and/or CST Microwave Studio simulation can be set up to test this idea first. Ultimately, the idea can be tested in the electromagnetic resonator cavity using a time reversal mirror experimental set up schematically illustrated in Fig. 6.1.

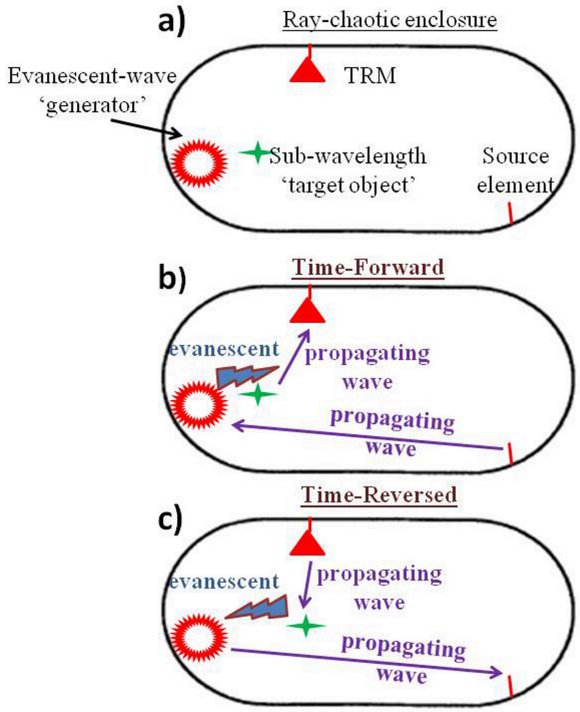

Figure 6.1: a) Illustration of a ray-chaotic enclosure that contains a time reversal mirror(TRM), a wave source, an evanescent-wave "generator", and a sub-wavelength target object that is under surveillance. b) The time-forward operation of the time reversal mirror: the propagating waves emanating from the source get converted into evanescent waves by the evanescent wave "generator", and back to propagating waves by the target object that is being monitored. c) In the time-reverse operation of the TRM, the propagating waves that start out at the TRM and reach the target object get converted to evanescent waves and back to propagating wave before reconstructing the source signal at the source location.

6.2.1.2 Direct Approach to Test the Detectability of Sub-Wavelength Perturbations

The one cubic meter electromagnetic cavity, which is introduced in Sec. 3.3.1, provides a controllable platform to test the effect of sub-wavelength perturbations (if such small perturbations are detectable at all). To be exact, the size of the cavity is much bigger than a typical wavelength of microwaves used, and at the same time it is not likely that there will be an uncontrollable sub-wavelength change in the boundaries of the cavity over the span of time the experiment is carried out. Therefore, one can induce controlled sub-wavelength perturbations to the cavity, and check if these perturbations can be detected by any of the sensing techniques developed in Chapter 2. Specific examples of such controlled sub-wavelength perturbations include: an aluminum pole (with sub-wavelength dimensions) that can be precisely motor-stepped into the cavity through a hole on the wall, a small magnetic object inside the cavity that can be moved by magnets from outside, etc. Regarding perturbers that can be moved around inside the cavity: both cases of moving a sub-wavelength perturber across a super-wavelength distance, and moving a sub-wavelength perturber over a sub-wavelength distance can be investigated. If these perturbations can be detected, the regime of fidelity decay [14] the perturbations induce can be examined (there is more discussion about the fidelity decay in Sec. 6.2.4).

6.2.2 Coupling Perturbations

While pursuing the design of sensors that extend the concepts of Quantum Fidelity and the Loschmidt Echo in Chapters 2 and 3, several research questions of general interest crop up. Perturbations, whose detection is of practical interest, usually happen inside the cavity. On the other hand, the ramifications of "coupling perturbations" to the antenna feeding energy into a chaotic cavity is of fundamental interest. Our research group had previously developed a model called the Random Coupling Model(RCM), which describes the statistical behavior of chaotic resonant cavities [4, 5, 6, 7]. Most of the perturbations that can be applied to chaotic cavities using the RCM cannot be directly realized experimentally; however, coupling perturbations can be performed both in the RCM and experimentally. Thus, the experimental investigation of coupling perturbations is interesting because the results can be compared directly with theory; for this purpose, a study of the RCM predictions of coupling perturbations can be performed. Such perturbations have not been studied before, to our knowledge.

Experimental Technique to Perform Coupling Perturbations

The effect of coupling perturbations on the classical analogs of the Loschmidt Echo and the Quantum Fidelity was preliminarily investigated in the electromagnetic cavity. Electromagnetic energy was coupled into this cavity using an antenna whose radiation impedance (and hence the coupling) was adjusted electronically. This was accomplished by using a varactor diode that was connected to the center

conductor and ground of a coaxial transmission line that slightly protrudes into the cavity through a small hole on the wall of the cavity (See Fig. 6.2). The center conductor of the coax, which couples the microwaves into the cavity, was biased using a DC voltage to ultimately bias the varactor diode. The bias voltage applied on the varactor diode changed its capacitance. The loop of wire, which protrudes into the cavity while carrying the diode, was designed to have a length of at least half of the wavelength of the microwaves; this guarantees that the current distribution on this radiating loop of wire changes significantly as the capacitance of the diode is changed. The change in the current distribution guarantees a change in the radiation impedance and hence the coupling into the cavity. One can quantify the change in coupling by measuring the radiation impedance of the antenna in two extreme cases: reverse bias, and forward bias. Based on previous work in our group on a dipole antenna that extends down to the bottom of a quasi-2D cavity, the radiation impedance is shown to be a function of the antenna current profile function $u(x, y)$ [8]. Based on this result for an antenna in a quasi-2D cavity, we hypothesize that a change in the current distribution of the antenna in the 3D cavity may result in a change in the radiation impedance.

Once an antenna with an adjustable coupling, (over a range of frequencies), is designed, the usual experiments to detect perturbations can be carried out. Particularly, manifestation of the coupling perturbations on the following calculations can be sought. The fidelity between sona signals collected before and after the perturbation can be studied as a function time; this study may perhaps reveal a new fidelity decay regime for coupling perturbations. A time reversal experiment

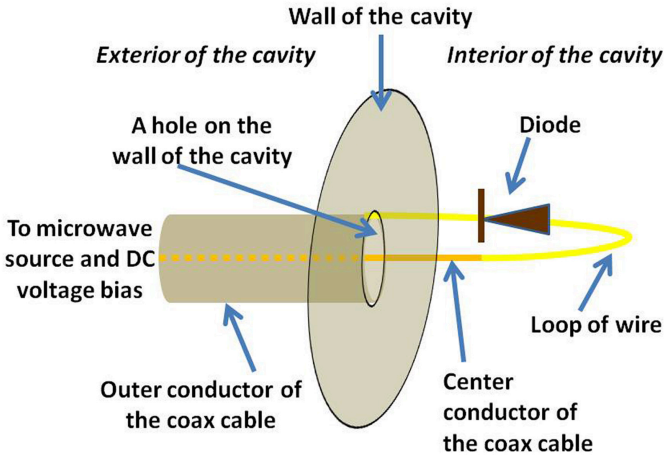

Figure 6.2: A schematic of an antenna, whose radiation impedance can be adjusted by applying a bias voltage on the constituent diode. The antenna is inserted into the one cubic meter electromagnetic cavity through a hole on the wall of the cavity.

can also be performed before and after a coupling perturbation, and the resulting reconstructed time reversed pulses can be compared. All these experimental results can be compared with results from the time domain version of the Random Coupling Model (RCM). The time domain version of the RCM was developed by our group to describe a generic wave chaotic cavity [6], and it is possible to do coupling perturbations in this computer model.

A preliminary experiment was performed using the antenna shown in Fig. 6.2. The $S_{11}(\omega)$ parameter of the antenna changed as the bias DC voltage on the antenna was increased. A one-port time reversal experiment was carried out using this antenna. The peak-to-peak amplitude of the reconstructed pulse decreased as the bias DC voltage was increased during step 2 of the time reversal mirror.

6.2.3 The Role of Chaos

The operation of the sensors fundamentally assumes that the cavity under surveillance is wave chaotic. Thus, it is worth investigating the operation of the sensors for cavities with different Lyapunov exponents [1]. This study is important because it helps define the applicability of the sensors to different kinds of cavities.

Experiment to Study the Role of Chaos on the Performance of the Sensors

The design of the sensors assumes that the cavity under surveillance is wave chaotic. The vitality of this assumption can be examined by modifying the walls of

the cavity (which is first introduced in Sec. 3.3.1) to effectively change the Lyapunov exponent of the underlying ray chaos. Introducing curved walls or scatterers in the cavity evidently increases the largest Lyapunov exponent. Whereas, removing the existing flat panel scatterers inside the cavity and perhaps making sure the interior of the cavity is as smooth as possible will bring the cavity closer to approximating the integrable case. The largest Lyapunov Exponent of a given configuration of the cavity can be calculated using a software model that relies on calculation of ray trajectories given the physical dimensions of the cavity's boundaries. This work will give insight into the following issues: the robustness of the time reversal mirror in a system that may approximate an integrable system, and the overall performance of the sensing techniques in cavities with different Lyapunov exponents.

6.2.4 A Study of Fidelity Decay

The sensors that extend the Quantum Fidelity to classical waves rely on a direct comparison of two sona signals which are collected before and after a perturbation. The comparison between these two sonas can be described using a single number such as their cross correlation or mutual information. Another approach that is commonly taken is to examine the fidelity between the sona signals as a function of time, commonly known as the "scattering fidelity" in the literature [14]. The scattering fidelity, which starts close to 1, is normally expected to decrease with time.

There are different regimes of fidelity decay that had been identified and dis-

cussed for different kinds of perturbations [14]. For instance, for sufficiently small perturbations, fidelity decays as a Gaussian function of time, which is called the "perturbative decay regime" [14]. On the other hand, there is a perturbation dependent exponential decay of the fidelity, which is derived from Random Matrix Theory; this is called the "Fermi golden rule decay regime" [14]. It is fascinating to look for new regimes of fidelity decay. So far, exponential decay of fidelity has not been observed experimentally. It also remains to be seen if local and global coupling to loss channels result in different regimes of fidelity decay.

Techniques to Calculate Fidelity Decay for Different Kinds of Perturbations

The comparison between two sona signals collected before and after a perturbation can be done as follows. First, the two sona signals are aligned in time. Then, corresponding portions of the sonas, with some chosen interval-length in time, are compared. The comparison is done by computing the cross correlations of the portions of the sonas which share the same start and stop time on the common time axis the two sonas share. Each such correlation value obtained tells us the scattering fidelity of those two sonas at some point in time, which is the time stamp of the portion of the sonas used to obtain that particular correlation value. In this manner, the fidelity between two sonas as a function of time can be plotted. Typically, the fidelity between two sona signals starts at one and decreases with time.

Different regimes of fidelity decay can be expected depending on the type of

perturbation applied. The following kinds of perturbations can be attempted with the goal of finding new regimes of fidelity decay. The first kind of perturbation that will be used is the introduction of absorbing channels. This can be accomplished by putting microwave absorbing patches on the walls of the electromagnetic cavity. The size of the absorbers can be chosen to be either on the order of the wavelength, or much larger than the wavelength; these two cases perhaps will allow us to look at different regimes of fidelity decay induced by the introduction of local and global absorbing channels. It will be interesting if any of these perturbations result in an exponential fidelity decay, which has not been experimentally observed before.

In addition to the experimental approach, the fidelity decay can also be studied using the analytical computer models such as the time domain Random Coupling Model and the star graph model (which was first introduced in Sec. 3.4.1).

6.2.5 Sensing Assisted by the Iterative Time Reversal and Exponential Amplification

In Chapter 4, it was stated that the iterative technique can be useful in applications in which time reversal mirrors have already been employed, but could benefit from an enhanced focusing. An example of such application of time reversal mirrors is sensing as introduced in Chapter 2.

As described in Sec. 2.4.3, the sona signals are exponentially amplified to extend the spatial range of sensors based on time reversal mirrors. However, we know from Chapter 5 that the exponential amplification of the sona results in significant

temporal sidelobes on the reconstructed pulse. It is true that the techniques in Chapter 5 can be applied to remove these unwanted sidelobes (induced by exponential amplification) from the reconstructed pulse, after it is digitized. However, the main advantage of the sensing techniques based on time reversal (i.e. Sec. 2.4.2) over the sensing techniques based on direct propagation comparison (i.e. Sec. 2.4.1) is the following. The reconstructed time reversed pulse does not even have to be fully digitized; we only need to measure its peak-to-peak-amplitude (PPA) using a simple circuit. This is a huge computational advantage of the sensing techniques based on time reversal mirrors. However, for this advantage to materialize, the reconstructed pulse should stand out from its temporal sidelobes; otherwise, it is not possible to easily measure its PPA. Therefore, if exponential amplification is applied to extend the range of the sensors, the sensing techniques based on time reversal may lose their computational advantage. In this situation, the iterative time reversal technique can be used to suppress the temporal sidelobes of the reconstructed pulse obtained from an exponentially amplified sona. This will allow the reconstructed pulse to stand out from its suppressed temporal sidelobes, as its PPA is measured in real time. Therefore, the sensing techniques based on time reversal mirrors can retain their computational advantage using the iterative technique, while they extend their range using the exponential amplification technique.

More concretely, the following sensing experiment can be performed using the iterative and exponential amplification techniques. Collect a sona from a cavity. Exponentially amplify the sona to increase the range of the sensor. Time reverse, and broadcast the exponentially amplified sona back into the cavity. Collect the

reconstructed pulse, which has temporal sidelobes induced by the exponential amplification. These temporal sidelobes inhibit the simple measurement of the PPA of the pulse. At this point, apply the iterative time reversal technique, which is described in Chapter 4, to perfect the exponentially amplified sona. It is vital that the cavity is not perturbed as the iterative process is carried out. The tunable iterative technique may be preferable as it takes less time to complete. The resulting optimal sona has two properties: i) it has more information about the parts of the cavity far away from the sensor because it is exponentially amplified, and ii) it does not result in temporal sidelobes of the reconstructed pulse because it is treated by the iterative technique. Finally, time reverse and broadcast this optimal sona periodically, and monitor the PPA of the reconstructed pulses to detect perturbations. A preliminary test of this procedure was carried out using the star graph model, which is introduced in Sec.3.4.1. The preliminary simulation results were promising, and should lead to successful experiments.

6.2.6 Super-Resolution Time Reversed Focusing

Time reversed wave focusing with a sub-wavelength resolution can be realized using electromagnetic waves. This work may enable the development of a super-resolution microwave microscope.

Imagine a two port, electromagnetic, time reversal experiment with antenna 1 and antenna 2 in a wave chaotic enclosure. The brief pulse broadcast by antenna 1 is picked up by antenna 2 as a sona. The time reversed sona is then re-injected

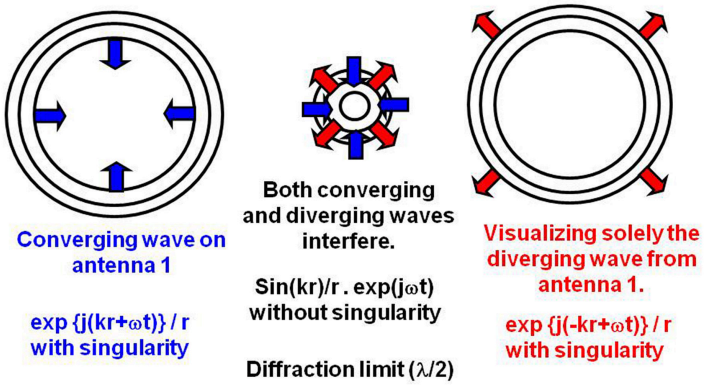

Figure 6.3: When the time reversed sona converges on antenna 1, it also is followed by a diverging wave due to impedance mismatch. The two waves interfere resulting in a sinc waveform which is the cause of the diffraction limit for wave focusing. Courtesy: Original figure from M. Fink (http://ohd2007.esisar.inpg.fr/ppt/INV2.pdf).

back into the cavity through antenna 2. This time reversed sona undoes its original path and collapses on antenna 1 (see Fig. 6.3). However, the impedance mismatch at antenna 1 means that a portion of the energy of the time reversed pulse that reconstructs at antenna 1 passes through and then diverges back into the cavity. This results in the imperfection of the time reversal mirror, because a time-reversed version of this diverging waveform was not there in the first part of the procedure. This imperfection can be corrected by adding a "sink" at antenna 1 [40]. The sink can be realized by simply injecting a π-shifted and time-reversed pulse at antenna 1 at the exact time that the reconstruction of the time reversed pulse happens. The amplitude of this π-shifted pulse will be adaptively chosen so as to completely cancel out the diverging waveform that results. This will guarantee that after the time reversed reconstruction of the pulse at antenna 1, there is no signal propagating in the cavity. This means that the time reversal mirror is indeed perfect.

So far we have described how the diverging wave comes about, and how it can be cancelled out in order to make the time reversal mirror perfect. One of the problems with the diverging wave is that it interferes with the converging wave (i.e. the time reversed sona collapsing on antenna 1), and the resulting spatial side-lobes degrade the spatial resolution of the time reversed reconstruction. Therefore, using the π-shifted pulse ("sink") to cancel out the diverging wave can improve the spatial resolution of the reconstruction.

The procedure mentioned above can be simulated using CST Microwave Studio and/or High Frequency Simulation Software (HFSS); such simulations will give insight into the experiment. If the experiment is successful (i.e. if the diverging

wave is canceled out), there will be no microwave energy after the pulse reconstruction at a separate pick up antenna that can be put anywhere else in the cavity. A successful demonstration of the principle of super-resolution time reversed focusing will open the door to the pursuit of exciting applications such as the development of super-resolution microwave microscopes using time reversal mirrors.

Appendix A

Setting up the Electromagnetic Time Reversal Mirror

The electromagnetic time reversal mirror which is utilized in Chapters 3, 4, and 5 of this dissertation consists of the following instruments: an Agilent Digital Storage Oscilloscope (DSO 91304A), a Tektronix Arbitrary Waveform Generator (AWG 7052), and an Agilent PSG Vector Signal Generator (PSG E8267D) (i.e. microwave source). The code used to automate the control of these instruments is provided in the Wiki page of our research group (www.anlage-wiki.physics.umd.edu); there is also a documentation and user's guide to the code. Here, only the most important conceptual aspects of the code are summarized.

A.1 Signal Acquisition through Aligned Averaging

The trigger time jitter in oscilloscopes is a notorious problem. The problem diminishes the advantage of the default averaging functionality of most oscilloscopes. Because, the sample signals that are being automatically averaged by the oscilloscope may not always be exactly in phase. As a result, the default averaging functionality of the oscilloscope cancels out the contributions of some of the sample signals that are out of phase with each other.

The solution to this problem is real-time aligned averaging by software. At every instant that a sample signal is acquired, it is aligned with a running sum

of the signals by maximizing its cross correlation with the running sum. After the alignment, the sample signal is added into the running sum of the signals. This process is continued until the specified number of sample signals is collected. Finally, the running sum can be divided by the number of samples to obtain the averaged signal. This scheme was implemented successfully to maximize the signal to noise ratio of the averaged signal.

A.2 Notch Filtering

The time reversal mirror uses an AWG which drives a microwave source. The AWG generates in-phase and quadrature signals. These signals are used to do I/Q modulation of a carrier frequency generated by the microwave source. This process introduces a coherent residual signal that is unwanted in the final RF output of the microwave source. This unwanted signal is a continuous wave at the carrier frequency specified. Unless this coherent residual signal is removed from the recorded signals, the signal to noise ratio is compromised. A notch filter was successfully implemented to solve this problem.

Appendix B

Modeling the Star Graph

The star graph model, which is introduced in Sec. 3.4.1, was implemented using a code that will be provided in the Wiki page of our research group (www.anlage-wiki.physics.umd.edu). Here, the most important aspects of code is summarized.

B.1 Frequency Domain Implementation

The star graph is modeled using the frequency domain for results in this dissertation. The frequency domain approach uses the analytical determination of the scattering parameter of the 1-port system as detailed in Sec. 3.4.1. The response to any time domain input signal can be readily calculated using the scattering parameters after Fourier transforming the input signal.

B.2 Time Domain Implementation

The time domain approach is an alternative approach to model the star graph. Even though this implementation was not particularly used for results in this dissertation, it has been shown that its results agree with the results from the frequency domain implementation of the star graph if the same specification of the star graph is provided to both implementations.

The algorithm for the time domain implementation of the star graph uses the

following parameters to define the system. Each of the N transmission lines of the star graph are labeled by $i = 1$ to $i = N$. The driving transmission line is labeled by $i = 0$, and it has zero length. The reflection coefficient from the terminations of each of the lines is Γ_i for $i = 1$ to $i = N$. In the time domain implementation of the star graph, loss is readily introduced by choosing values of $\Gamma_i < 1$. The one-way propagation time from the node of the star graph to the termination on transmission line i is denoted by t_i, where i ranges from 1 to N. The characteristic impedance of the i^{th} transmission line is given by Z_{ci} for i ranging from 0 to N. The voltage wave incident on the node from the i^{th} transmission line is V_{i+}. Whereas, the voltage wave that is leaving the node and propagating on the i^{th} transmission line is V_{i-}.

The total voltage at the node is denoted by $V_N(t)$, and it is

$$V_N(t) = V_{i+}(t) + V_{i-}(t), \tag{B.1}$$

where i ranges from 0 to N. The current on the i^{th} transmission line is denoted by $I_i(t)$, and it is given by

$$I_i(t) = \frac{1}{Z_{ci}}[V_{i+}(t) - V_{i-}(t)], \tag{B.2}$$

where i ranges from 0 to N. The total current at the node should be zero.

$$\sum_{i=0}^{i=N} I_i(t) = 0 \tag{B.3}$$

At the terminations of the the transmission lines denoted with i ranging from 1 to N, the outgoing and incoming voltage waves are related as follows.

$$V_{i+}(t) = \Gamma_i V_{i-}(t - 2t_i), i = 1, 2, ..., N \tag{B.4}$$

Consider the following sum $\sum_{i=0}^{i=N} \frac{1}{Z_{ci}}(V_{i+}(t) + V_{i-}(t))$. Using Eq. B.1, the sum is equal to $V_N(t) \sum_{i=0}^{i=N} \frac{1}{Z_{ci}}$. Next, Eq. B.2 can be used to substitute an expression for V_{i-}, which is $\frac{1}{Z_{ci}} V_{i-} = \frac{1}{Z_{ci}} V_{i+} - I_i$, into the summation considered. The resulting expression is $\sum_{i=0}^{i=N} (\frac{2}{Z_{ci}} V_{i+}(t) - I_i) = V_N(t) \sum_{i=0}^{i=N} \frac{1}{Z_{ci}}$. At this point, Eq. B.3 can be used to eliminate the second term on the left hand side to get

$$2 \sum_{i=0}^{i=N} \frac{V_{i+}(t)}{Z_{ci}} = V_N(t) \sum_{i=0}^{i=N} \frac{1}{Z_{ci}}. \tag{B.5}$$

This equation can be solved for $V_N(t)$ if $V_{i+}(t)$ is given for all i ranging from 0 to N.

For a given input signal on the driving line (i.e. $V_{0+}(t)$), the output signal can be determined as follows. At the beginning (i.e. $t = 0$), there are no incoming voltage waves from the lines labeled with i ranging from 1 to N (i.e. $V_{i+}(t = 0) = 0$ for $i = 1, 2, ..., N$). So, Eq. B.5 can be used to solve for $V_N(t = 0)$ using the ingoing voltage through the driving line (i.e. $V_{0+}(t = 0)$). Once the node voltage is known, the voltage waves that are immediately outgoing from the node can be determined using Eq. B.1 for all the lines. These voltages should be stored for each of the lines i ranging from 1 to N; because, they are used to determine the voltage incoming towards the node after time $2t_i$ using Eq. B.4 for $i = 1, 2, ..., N$. Once the incoming voltages (i.e. $V_{i+}(t)$) are determined, $V_N(t)$ can be solved for. This iteration can be continued to calculate the voltage waves that leave the node towards the driving line (i.e. $V_{0-}(t)$) for all times.

Bibliography

[1] E. Ott, *Chaos in dynamical systems*. Cambridge, U.K. ; New York: Cambridge University Press, 2nd ed., 2002.

[2] H.-J. Stockmann, *Quantum chaos : an introduction*. Cambridge: Cambridge University Press, 1999.

[3] R. K. Snieder and J. A. Scales, "Time-reversed imaging as a diagnostic of wave and particle chaos," *Physical Review E*, vol. 58, no. 5, pp. 5668–5675, 1998.

[4] X. Zheng, T. M. Antonsen, and E. Ott, "Statistics of impedance and scattering matrices of chaotic microwave cavities with multiple ports," *Electromagnetics*, vol. 26, no. 1, pp. 37–55, 2006.

[5] X. Zheng, T. M. Antonsen, and E. Ott, "Statistics of impedance and scattering matrices in chaotic microwave cavities: Single channel case," *Electromagnetics*, vol. 26, no. 1, pp. 3–35, 2006.

[6] J. A. Hart, T. M. Antonsen, and E. Ott, "Scattering a pulse from a chaotic cavity: Transitioning from algebraic to exponential decay," *Physical Review E*, vol. 79, no. 1, 2009.

[7] J. A. Hart, T. M. Antonsen, and E. Ott, "Effect of short ray trajectories on the scattering statistics of wave chaotic systems," *Physical Review E*, vol. 80, no. 4, 2009.

[8] X. Zheng, *Statistics of impedance and scattering matrices in microwave chaotic cavities: the random coupling model*. Dissertation, University of Maryland College Park, 2005.

[9] S. Hemmady, X. Zheng, T. M. Antonsen, E. Ott, and S. M. Anlage, "Universal statistics of the scattering coefficient of chaotic microwave cavities," *Physical Review E*, vol. 71, no. 5, 2005.

[10] S. Hemmady, X. Zheng, E. Ott, T. M. Antonsen, and S. M. Anlage, "Universal impedance fluctuations in wave chaotic systems," *Physical Review Letters*, vol. 94, no. 1, 2005.

[11] S. D. Hemmady, *A Wave-Chaotic Approach To Predicting And Measuring Electromagnetic Field Quantities In Complicated Enclosures*. Dissertation, University of Maryland College Park, 2006.

[12] a, "Loschmidt-echo decay from local boundary perturbations," *Physical Review E*, vol. 75, no. 1, 2007.

[13] A. Peres, "Stability of quantum motion in chaotic and regular systems," *Physical Review A*, vol. 30, no. 4, pp. 1610–1615, 1984.

[14] T. Gorin, T. Prosen, T. H. Seligman, and M. Znidaric, "Dynamics of loschmidt echoes and fidelity decay," *Physics Reports-Review Section of Physics Letters*, vol. 435, no. 2-5, pp. 33–156, 2006.

[15] T. Gorin, T. H. Seligman, and R. L. Weaver, "Scattering fidelity in elastodynamics," *Physical Review E*, vol. 73, no. 1, 2006.

[16] A. H. Quazi, "Method and system for processing acoustic signals," 1998.

[17] C. P. Slichter, *Principles of magnetic resonance, 3rd ed.*, vol. 1. New York: Springer Verlag, 1990.

[18] B. T. Taddese, J. Hart, T. M. Antonsen, E. Ott, and S. M. Anlage, "Sensor based on extending the concept of fidelity to classical waves," *Applied Physics Letters*, vol. 95, no. 11, 2009.

[19] B. T. Taddese, M. D. Johnson, J. A. Hart, T. M. Antonsen, E. Ott, and S. M. Anlage, "Chaotic time-reversed acoustics: Sensitivity of the loschmidt echo to perturbations," *Acta Physica Polonica A*, vol. 116, no. 5, pp. 729–732, 2009.

[20] B. T. Taddese, T. M. Antonsen, E. Ott, and S. M. Anlage, "Sensing small changes in a wave chaotic scattering system," *Journal of Applied Physics*, vol. 108, no. 11, 2010.

[21] M. Fink, "Time reversal in acoustics," *Contemporary Physics*, vol. 37, no. 2, pp. 95–109, 1996.

[22] M. Fink, D. Cassereau, A. Derode, C. Prada, P. Roux, M. Tanter, J. L. Thomas, and F. Wu, "Time-reversed acoustics," *Reports on Progress in Physics*, vol. 63, no. 12, pp. 1933–1995, 2000.

[23] G. Lerosey, J. de Rosny, A. Tourin, A. Derode, G. Montaldo, and M. Fink, "Time reversal of electromagnetic waves," *Physical Review Letters*, vol. 92, no. 19, 2004.

[24] G. Lerosey, J. de Rosny, A. Tourin, A. Derode, and M. Fink, "Time reversal of wideband microwaves," *Applied Physics Letters*, vol. 88, no. 15, 2006.

[25] S. M. Anlage, J. Rodgers, S. Hemmady, J. Hart, T. M. Antonsen, and E. Ott, "New results in chaotic time-reversed electromagnetics: High frequency one-recording-channel time-reversal mirror," *Acta Physica Polonica A*, vol. 112, no. 4, pp. 569–574, 2007.

[26] C. Draeger and M. Fink, "One-channel time reversal of elastic waves in a chaotic 2d-silicon cavity," *Physical Review Letters*, vol. 79, no. 3, pp. 407–410, 1997.

[27] G. Montaldo, M. Tanter, and M. Fink, "Real time inverse filter focusing through iterative time reversal," *Journal of the Acoustical Society of America*, vol. 115, no. 2, pp. 768–775, 2004.

[28] M. Tanter, J. L. Thomas, and M. Fink, "Time reversal and the inverse filter," *Journal of the Acoustical Society of America*, vol. 108, no. 1, pp. 223–234, 2000.

[29] H. M. Pastawski, E. P. Danieli, H. L. Calvo, and L. E. F. F. Torres, "Towards a time reversal mirror for quantum systems," *Epl*, vol. 77, no. 4, 2007.

[30] B. T. Taddese, T. M. Antonsen, E. Ott, and S. M. Anlage, "Iterative time reversal with tunable convergence," *Electronics Letters*, vol. 47, no. 21, pp. 1165–1167, 2011.

[31] T. J. Ulrich, P. A. Johnson, and R. A. Guyer, "Interaction dynamics of elastic waves with a complex nonlinear scatterer through the use of a time reversal mirror," *Physical Review Letters*, vol. 98, no. 10, 2007.

[32] T. J. Ulrich, A. M. Sutin, T. Claytor, P. Papin, P. Y. Le Bas, and J. A. TenCate, "The time reversed elastic nonlinearity diagnostic applied to evaluation of diffusion bonds," *Applied Physics Letters*, vol. 93, no. 15, 2008.

[33] T. J. Ulrich, K. Van Den Abeele, P. Y. Le Bas, M. Griffa, B. E. Anderson, and R. A. Guyer, "Three component time reversal: Focusing vector components using a scalar source," *Journal of Applied Physics*, vol. 106, no. 11, 2009.

[34] A. Buerkle and K. Sarabandi, "Non-destructive evaluation of elastic targets using acousto-electromagnetic wave interaction and time reversal focusing," *Ieee Transactions on Antennas and Propagation*, vol. 57, no. 11, pp. 3628–3637, 2009.

[35] A. Bakulin and R. Calvert, "The virtual source method: Theory and case study," *Geophysics*, vol. 71, no. 4, pp. Si139–Si150, 2006.

[36] C. S. Larmat, R. A. Guyer, and P. A. Johnson, "Tremor source location using time reversal: Selecting the appropriate imaging field," *Geophysical Research Letters*, vol. 36, 2009.

[37] D. H. Liu, S. Vasudevan, J. Krolik, G. Bal, and L. Carin, "Electromagnetic time-reversal source localization in changing media: Experiment and analysis," *Ieee Transactions on Antennas and Propagation*, vol. 55, no. 2, pp. 344–354, 2007.

[38] M. Davy, J. de Rosny, J. C. Joly, and M. Fink, "Focusing and amplification of electromagnetic waves by time reversal in an leaky reverberation chamber," *Comptes Rendus Physique*, vol. 11, no. 1, pp. 37–43, 2010.

[39] G. Lerosey, J. De Rosny, A. Tourin, and M. Fink, "Focusing beyond the diffraction limit with far-field time reversal," *Science*, vol. 315, no. 5815, pp. 1120–1122, 2007.

[40] R. Carminati, J. J. Saenz, J. J. Greffet, and M. Nieto-Vesperinas, "Reciprocity, unitarity, and time-reversal symmetry of the s matrix of fields containing evanescent components," *Physical Review A*, vol. 62, no. 1, 2000.

[41] J. de Rosny and M. Fink, "Overcoming the diffraction limit in wave physics using a time-reversal mirror and a novel acoustic sink," *Physical Review Letters*, vol. 89, no. 12, 2002.

[42] P. Blomgren, G. Papanicolaou, and H. K. Zhao, "Super-resolution in time-reversal acoustics," *Journal of the Acoustical Society of America*, vol. 111, no. 1, pp. 230–248, 2002.

[43] R. Carminati, R. Pierrat, J. de Rosny, and M. Fink, "Theory of the time reversal cavity for electromagnetic fields," *Optics Letters*, vol. 32, no. 21, pp. 3107–3109, 2007.

[44] G. P. Chen, W. B. Yu, Z. Q. Zhao, Z. P. Nie, and Q. H. Liu, "The prototype of microwave-induced thermo-acoustic tomography imaging by time reversal mirror," *Journal of Electromagnetic Waves and Applications*, vol. 22, no. 11-12, pp. 1565–1574, 2008.

[45] D. H. Liu, G. Kang, L. Li, Y. Chen, S. Vasudevan, W. Joines, Q. H. Liu, J. Krolik, and L. Carin, "Electromagnetic time-reversal imaging of a target in a cluttered environment," *Ieee Transactions on Antennas and Propagation*, vol. 53, no. 9, pp. 3058–3066, 2005.

[46] G. Montaldo, D. Palacio, M. Tanter, and M. Fink, "Building three-dimensional images using a time-reversal chaotic cavity," *Ieee Transactions on Ultrasonics Ferroelectrics and Frequency Control*, vol. 52, no. 9, pp. 1489–1497, 2005.

[47] J. V. Candy, D. H. Chambers, C. L. Robbins, B. L. Guidry, A. J. Poggio, F. Dowla, and C. A. Hertzog, "Wideband multichannel time-reversal processing for acoustic communications in highly reverberant environments," *Journal of the Acoustical Society of America*, vol. 120, no. 2, pp. 838–851, 2006.

[48] S. Q. Xiao, J. Chen, B. Z. Wang, and X. F. Liu, "A numerical study on time-reversal electromagnetic wave for indoor ultra-wideband signal transmission," *Progress in Electromagnetics Research-Pier*, vol. 77, pp. 329–342, 2007.

[49] G. Lerosey, J. de Rosny, A. Tourin, A. Derode, G. Montaldo, and M. Fink, "Time reversal of electromagnetic waves and telecommunication," *Radio Science*, vol. 40, no. 6, 2005.

[50] H. Q. Zhai, S. S. Sha, V. K. Shenoy, S. Y. Jung, M. Y. Lu, K. Min, S. Lee, and D. S. Ha, "An electronic circuit system for time-reversal of ultra-wideband short impulses based on frequency-domain approach," *Ieee Transactions on Microwave Theory and Techniques*, vol. 58, no. 1, pp. 74–86, 2010.

[51] R. Schafer, H. J. Stockmann, T. Gorin, and T. H. Seligman, "Experimental verification of fidelity decay: From perturbative to fermi golden rule regime," *Physical Review Letters*, vol. 95, no. 18, 2005.

[52] B. Kober, U. Kuhl, H. J. Stockmann, T. Gorin, D. V. Savin, and T. H. Seligman, "Microwave fidelity studies by varying antenna coupling," *Physical Review E*, vol. 82, no. 3, 2010.

[53] O. I. Lobkis and R. L. Weaver, "Scattering fidelity in elastodynamics. ii. further experimental results," *Physical Review E*, vol. 78, no. 6, 2008.

[54] R. Schafer, T. Gorin, T. H. Seligman, and H. J. Stockmann, "Fidelity amplitude of the scattering matrix in microwave cavities," *New Journal of Physics*, vol. 7, 2005.

[55] C. Draeger and M. Fink, "One-channel time-reversal in chaotic cavities: Theoretical limits," *Journal of the Acoustical Society of America*, vol. 105, no. 2, pp. 611–617, 1999.

[56] H. L. Anderson and A. I. of Physics., *Physics vade mecum : AIP 50th anniversary*. New York: American Institute of Physics, 1981.

[57] A. Papana and D. Kugiumtzis, "Evaluation of mutual information estimators for time series," *International Journal of Bifurcation and Chaos*, vol. 19, no. 12, pp. 4197–4215, 2009.

[58] S. D. Cohen, H. L. D. D. Cavalcante, and D. J. Gauthier, "Subwavelength position sensing using nonlinear feedback and wave chaos," *Physical Review Letters*, vol. 107, no. 25, 2011.

[59] F. Moglie, "Convergence of the reverberation chambers to the equilibrium analyzed with the finite-difference time-domain algorithm," *Ieee Transactions on Electromagnetic Compatibility*, vol. 46, no. 3, pp. 469–476, 2004.

[60] F. Moglie and V. M. Primiani, "Analysis of the independent positions of reverberation chamber stirrers as a function of their operating conditions," *Ieee Transactions on Electromagnetic Compatibility*, vol. 53, no. 2, pp. 288–295, 2011.

[61] A. Taflove and S. C. Hagness, *Computational electrodynamics : the finite-difference time-domain method*. Boston: Artech House, 2nd ed., 2000.

[62] P. Rohan, *Introduction to electromagnetic wave propagation*. Boston: Artech House, 1991.

[63] T. Kottos and U. Smilansky, "Quantum graphs: a simple model for chaotic scattering," *Journal of Physics a-Mathematical and General*, vol. 36, no. 12, pp. 3501–3524, 2003.

[64] T. Kottos and U. Smilansky, "Periodic orbit theory and spectral statistics for quantum graphs," *Annals of Physics*, vol. 274, no. 1, pp. 76–124, 1999.

[65] A. Cozza, "Increasing peak-field generation efficiency of reverberation chamber," *Electronics Letters*, vol. 46, no. 1, pp. 38–39, 2010.

[66] D. Cassereau and M. Fink, "Time-reversal of ultrasonic fields .3. theory of the closed time-reversal cavity," *Ieee Transactions on Ultrasonics Ferroelectrics and Frequency Control*, vol. 39, no. 5, pp. 579–592, 1992.